

UNIVERSITY OF HERTFORDSHIRE

SUBMITTED TO THE UNIVERSITY OF HERTFORDSHIRE IN PARTIAL
FULFILMENT OF THE REQUIREMENT FOR THE DEGREE OF

MSC BY RESEARCH

**Synthetic Observations of Line
Emission from Simulated H II Regions**

Author

Luke FLEMING

Supervisor

Dr. James DALE

October 2020

Abstract

In this work I post-process a series of simulations of Giant Molecular Clouds (GMC) from Dale (2017), Dale et al. (2014) by running them through MOCASSIN (MONte CARlo SimulationS of Ionized Nebulae) and studying the emission from the simulated clouds. I present spectral energy distributions (SEDs) from each simulation, including from multiple directions for some runs to highlight how this has no effect on the obtained SED. With these I present a new correlation between how IR/UV ratios evolve with time, and how they change with different initial conditions. I also study the turbulent nature and behaviours of the clouds, determining what could dominate the measured turbulence through observational techniques on these simulations. Because these simulations omit stars lower than $20 M_{\odot}$, I identify the approximate missing luminosity, including from lower mass accretion and show that in spite of the missing stars, the SED results and time-dependent SED relationships are not impacted by this and still remain accurate for our clouds due to the missing emission being negligible with respect the massive stars and reprocessing through the GMC. Dust plays an integral role in the measured emission from molecular clouds, however is a challenging property to accurately model. Given that a dust grain size model is used in this work, I also conduct an experiment using several grain size distributions which highlighted our adopted distribution leads to predictions that, with the exception of distributions found only in circumstellar discs, were in agreement with observation. Finally, I study emission line ratios across the clouds and produce Baldwin, Phillips and Telervin (BPT) maps with known classification lines, and empirically derive new classification lines specific to ionised regions and molecular clouds based upon my results.

Contents

1	Introduction	4
2	H II regions	7
2.1	Formation of H II regions	8
2.1.1	Strömgren sphere	9
2.1.2	H II region classification	13
2.2	Star formation	14
2.2.1	Termination of low-mass star formation	15
2.3	Virial Ratio	15
3	Previous Observational work	17
3.1	Integral field spectroscopy and MUSE	17
3.2	Morphology and ageing	18
4	Turbulence	20
4.1	Quantitatively analysing turbulence	20
4.1.1	Larson’s relations	20
4.2	Turbulent processes	21
4.3	Structure function	22
5	Methods	25
5.1	Radiation hydrodynamic simulations	25
5.2	Monte Carlo and calculation methods	27
5.3	Parameters and Initial Conditions	28
5.3.1	Dust model	29
5.4	Output files from MOCASSIN	30
5.5	Visualising output results	30
6	Emission lines	30
7	Results and Discussion	31
7.1	Images	32
7.1.1	Photoionisation only	32
7.1.2	Photoionisation and winds	35
7.1.3	Photoionisation, winds and dust	36
7.2	Spectral Energy Distribution	36
7.2.1	Photoionisation only	38
7.2.2	Photoionisation and winds only	38
7.2.3	Photoionisation, winds and dust	39
7.3	Effects of dust grain-size distribution	39
7.4	Evolution of SED with time	43
7.4.1	Protostellar Luminosity Function	49
7.5	Consequence of orientation on apparent morphology	52
7.6	Derived Structure function	57

7.6.1	Hot gas only	65
7.7	BPT diagrams	66
8	Conclusions	72
9	Appendices	82
9.1	Appendix A	82
9.2	Appendix B	85
9.3	Appendix C	89
9.4	Appendix D	91

1 Introduction

This project will study simulations of massive star formation and the dynamics behind distinct celestial features such as pillars and bubbles. These bubbles are defined as H II (singly-ionized hydrogen) regions, and are caused by the ionisation of gas around one or more stars due to their radiation. This work will focus around the post-processing of hydrodynamic simulations of cloud collapse and star formation in an attempt to deduce observational properties that could later be used to infer characteristics in real H II regions. The project intends to answer questions regarding the initial conditions of these regions and whether it is possible to recover information about the early stages of these stellar nurseries (energetics, size or any other property). The potential of finding ways to age H II regions would be of vital use to observers, and therefore studying anything that changes systematically with time could be utilised to give approximate ages for these environments. Currently, morphologies are used as a tool to gauge an idea of the evolutionary stage and corresponding age range for these regions, and this method will be tested and challenged within this project to determine whether this can be a reliable method. Tan et al. (2014) give an in-depth review of massive star formation, including discussions on the specific formation mechanisms at play, the role of magnetic fields and feedback processes, as well as numerical simulations to help understand magnetic fields and radiation pressure within the early stages of protostellar accretion. Krumholz et al. (2014) also gives a concise yet in-depth look into stellar winds, radiative and momentum driven feedback- something which will become evidently important in the simulations used in this work. Krumholz et al. (2014) also use some of the simulations seen in this work as examples to discuss the weak effects of stellar winds, and how photoionisation is dominant within molecular clouds. These reviews are a good reference for some of the concepts, mechanics and processes that will be discussed later in this thesis.

Giant Molecular Clouds (GMCs) are the most common homes for star formation and exhibit many turbulent features (Falgarone 1997). The turbulent features of the GMCs lead to density perturbations that result in smaller scale gas clumps capable of collapse and star formation, should they satisfy the Jeans Mass criterion - defining that a cloud of a given radius will collapse under gravity without re-expansion should the clump's mass exceed this mass (Bonnell et al. 2006). It is not yet clear why GMCs are turbulent, or why they are able to maintain their levels of turbulence, leading to the requirement of understanding ways that turbulence can be replenished within the cloud in order to understand observation. One potential method is the occurrence of H II regions within the GMCs. As massive stars form within these clumps and ionise the surrounding gas, the ionised region exerts an outward force towards the neutral gas which, in turn, may sustain the turbulence, as suggested by Gritschneider et al. (2009). The massive stars form irregular bubble-like ionisation fields that firstly reach an ionisation-recombination equilibrium, and after this expand under pressure influence (I give a full description of H II mechanisms in Section 2.1). The true behaviour of turbulence inside the H II region is largely unknown and is still debated (Medina et al. (2014), Gingold & Monaghan (1977)).

Observations of H II regions have been taken for many decades, and are visually some of the most attractive celestial objects captured. For observers, gathering valuable information about them is a challenging task, and it is only through instruments such as MUSE (Multi Unit Spectroscopic Explorer) that we have had a more in depth and detailed look at these en-

vironments. With new instruments such as MUSE allowing us to study H II regions at a new, unprecedentedly high level, with a bigger wavelength coverage and higher sensitivity, there lies a demand for sophisticated simulations to assist with interpreting observation. With this new level of observational capability more advanced methods have become available. I will attempt to use structure functions to quantify the velocity and turbulent information that has previously been done by numerous authors, such as Boneberg et al. (2015), McLeod et al. (2016), Chira et al. (2019), to further investigate how turbulence evolves through molecular clouds as well as test how turbulence decays without a driving force or mechanism. It is widely suggested that unless either internally or externally there is no mechanism that is maintaining the turbulence then it should decay quickly (Boneberg et al. (2015), Mac Low et al. (1998)). Using the mentioned structure functions should help to identify the nature of the turbulence with no definitive driving force other than the ionising stars.

Turbulent Giant Molecular Clouds have a wide range of masses, radial sizes, turbulent velocity dispersions, densities and many other properties. Their masses are typically in excess of $10^4 M_{\odot}$ and can be up to $10^7 M_{\odot}$ (Fukui & Kawamura 2010), radii of up to 200 pc (Murray 2011) and surface densities of less than $10^{-2} M_{\odot} \text{ pc}^{-2}$ and upwards of $10 M_{\odot} \text{ pc}^{-2}$ (Dale & Bonnell 2008). Initial conditions of GMCs can have future consequences on their ability to form stars, and therefore being able to derive the initial conditions of a given molecular cloud from observation would aid the ability of astronomers to identify certain properties that these clouds would have in the early stages of their lives. This especially applies to the study of H II regions as morphological changes occur from numerous internal and external processes. If certain changes can be linked to these initial parameters then they can act as indicators to how the early environments in these systems would have looked. I will attempt to use new methods to study and investigate the overall changes in the morphology of a GMC with regards to the level of destruction caused by stars over the course of its life, and as a further indicator to the ages and star formation activity that is independent of the orientation of the object with respect to the observer. This will involve a new look at how we can use the spectral energy distributions (SEDs) to quantify how molecular clouds evolve by monitoring the flux in infrared and ultraviolet frequency bands.

In both observation and simulation, results are complicated by a combinatory mixture of dust and gas that makes up GMCs as dust can lead to extinction and reddening, where shorter wavelengths of light are absorbed by the dust, leading to the effect of objects appearing redder. Dust is vital in the reprocessing of emission from the stars, and the effects of dust have been numerous observed and studied by authors such as Zhuravlev (2020) who studied the dynamic role of dust with molecular clouds, Lefèvre et al. (2014) who used observation to constrain a dust grain-size distribution and then use radiative transfer models to study how the dust grain-size distribution affected the scattering of IR light in dark clouds and Paradis et al. (2019) who used dust models and infrared data to study the dust parameters in different environments. A portion of this investigation will investigate the IR and UV emission from the simulated H II region, and therefore the dust distribution I use in this work may have an influence on the level of reprocessing or the frequency distribution of the IR emission. A study of six different dust grain-size distributions that include both distributions from other authors and that of what may be found within these regions, to determine what effect, if any, that the dust may have. Should there be any differences within the SEDs that arise within the different dust grain-size distributions, it will be of

deep interest to understand why this occurs in the processing of these simulations, what its implications are on the resulting findings we show and whether the grain-size distributions that show large deviation in either their shape or intensity of their SED are of any significance to my simulations environments. For example, dust distributions that are found in rare or very small environments would not be representative of an entire GMC region, and as a result should their SED look different, it may be appropriate to acknowledge but not be concerned by the deviating result.

Simulation work and modelling of H II regions has a very full and recent history, dating back to the early-mid 1960s where the first models were attempted (Vandervoort 1963), with very early theories from the mid 1950s (Oort 1954). For this reason, I will not attempt to address the corpus of literature in its entirety in this work, but instead I have selected some of the milestone papers. Oort (1954) developed reasonable statistical models for the formation of O-type stars within molecular clouds, and produced numerical models of parameters such as energy balancing between cloud collisions and formation of other clouds. As well as this, Oort (1954) further developed our understanding of how O-type stars behave on surroundings clouds, and at what distances ionising effects of these stars become negligible, and also the causes of the motion of shock-fronts. These findings then helped to identify how mass is lost (evaporated) from a cloud given distance, temperature, composition etc. Other authors such as Vandervoort (1963) carried out very simplified models to determine qualitative predictions of such regions. These simulations lacked the ability to model key characteristics such as the formation of a massive star due to gravitational collapse, turbulence within the gas and dust, modelling of chemical composition of the GMC the star(s) form in, and many other parameters that we now have the opportunity to utilise.

Hydrodynamic simulations began to occur within the research field of H II regions during the 1980s with authors such as Noriega-Crespo (1986) using numerical hydrodynamic simulations to study the dynamics of the residual gas, conditions for star formation and the effects on star formation efficiency, as well as the removal of gas in some scenarios. Their simulations were able to include a multitude of parameters and considerations - stellar system structure and gravitational field, the formation of new conditions where continued star formation could occur, time-dependent flux of the ionizing O and B stars, different metal abundances and the effects of supernovae (Noriega-Crespo 1986). Their results lead to a multitude of conclusions, but those that may be most notable was the finding that when in-falling gas of a high enough mass-rate with time was included then it was possible to completely inhibit and prevent all mass loss from the H II regions. Since this point, simulations have been continually used and utilised to study the complicated and intricate internal and external mechanics of GMCs - far beyond all that could be mentioned in this work.

The first Smooth Particle Hydrodynamic (SPH) simulations to study H II regions come from the work of Kessel-Deynet (1999), where they were used to both study the effects of feedback from young stars of their surroundings, and the fragmentation of turbulent molecular clouds. They were successfully able to demonstrate the time dependent ionisation of massive stars, heating effects found inside H II regions and hydrodynamics. It is this style of simulation that was then adopted into the simulations used for this work, as the aforementioned reasons govern that they are better suited for the intrinsically complicated mechanisms, such as turbulence and stellar feedback, that operate within turbulent molecular clouds. They also remove the potential for grid cell errors and model larger fluids effectively

whilst maintaining more accurate modelling of smaller regions or individual particles. It also treats the fluid not as multiple point masses, but as a collection of particles instead with a measurable radius, and better resolutions can be achieved simply by using more particles (Anathpinkida 2008). This is especially useful in methods we will use that will study specifically the turbulent motion of particles within the clouds as it allows for particles to collide, interact and influence each other. Following this, the first ever SPH simulations of star formation that included ionising feedback from massive stars was conducted by Dale et al. (2005), and created a new horizon of potential with understanding these vastly complex regions.

Today, we have the computational ability to be able to run high memory simulations of more complex star forming scenarios, and include multiple physical processes and parameters to continually converge towards a more complete theory and understanding of how massive star formation and H II regions form, evolve, affect their environments and disappear. This project intends to fully utilise the ability of computers to simulate massive star formation and H II regions in order to expand upon simulations previously carried out by Dale et al. (2014) and Dale (2017) to fully understand just what is the potential we have to learn from simulation about the regions we have observed for hundreds of years.

By the end of this work I intend to present numerous data sets from simulations run by Dale et al. (2014) and Dale (2017) to provide informative demonstrations of how observations can be affected by numerous factors that are both intrinsic to the cloud and a consequence of limited observational capabilities. Further to this, I will analyse the turbulence from our simulation results to illustrate the evolution through time, and to demonstrate how turbulence changes depending on how bound the cloud is, the initial size and other characteristics. The results from our new method to measure the level of destruction and how bound the cloud is may be potentially a step towards ageing star forming and ionisation regions with a more systematic approach. Maps of selected regions in the emission used in this work are given, along with spectral energy distributions and investigative work in the effects of dust distributions.

2 H II regions

H II regions are amongst the most fascinating and unique phenomena in the universe due to their intrinsic shapes and notably famous features (pillars such as the Pillars of Creation). Observations of H II regions can be traced back through hundreds of years, dating as far as 1774 by William Herschel, where he described sights of the Orion Nebula as “*an uninformed fiery mist, the chaotic material of future suns*”, with his prediction of star formation being confirmed approximately 100 years later by William and Mary Huggins (Jones et al. 1991). It was in the 1920s when more intricate observational details of H II regions were discovered, such that at very low gas densities it is found that O^{2+} emits the forbidden line of 500.7 nm (O’dell 2001), discussed further in Section 6. These tracers have helped the understanding and observations of H II regions to a great extent. With the ever-increasing capabilities within observational astronomy and astrophysics, it has now been possible to image several hundreds, and even thousands of H II regions within our own galaxy and further afield in other galaxies. Over the course of the history of studying H II regions, astronomers

have been able to go from the belief that these regions are a chaotic mess, with random and unpredictable behaviours, to a system of intricate and balanced processes that act in equilibrium with the multitude of physical and chemical parameters that occur.

The impact and effects of H II regions and massive star formation cannot be overstated. Over a range of spatial scales the formation of any star, but predominantly massive stars whose Zero Age Main Sequence, ZAMS, mass (given as the mass at which the star joins the Main Sequence and begins fusing hydrogen) is $> 8M_{\odot}$, their stellar feedback has effects on scales as small as accretion discs and protostellar cores up to whole molecular clouds and bigger still (Dale et al. 2014). Photoionisation and winds from massive stars affects an intermediate range of surroundings; continually increasing with time and with ionisation.

2.1 Formation of H II regions

H II regions most commonly form within dense molecular clouds, and both molecular clouds and the H II regions that are forming within them are intrinsic identifiers of star formation - specifically massive O and early B-type stars. These molecular clouds can have been formed by previous H II regions that have caused cold gas to become denser and more compact as the regions expand, and it is within the most dense regions, usually embedded far within the clouds, where stars form. It is to be noted that stars are classified in this way through the Morgan-Keenan spectral classification system, being given a letter from O, B, A, F, G, K, M. These are determined through the temperature of the star - with O being the hottest and M being the coldest. Subdivisions of these classifications further segregate the stars by temperature with a number following the letter from 0-9. Finally, Roman numerals are given to identify the star by luminosity- 0 for hypergiants through to VII for white dwarfs.

Massive stars (defined as being greater than $8 M_{\odot}$) have been shown from multiple observations, and resultant model atmospheric fitting to have surface temperature in the range of 30,000 K - 40,000 K, as shown by UV and optical spectroscopy from Bianchi & Garcia (2014) and Gordon et al. (2018). Above the masses of massive stars, such stars have a significantly higher luminosities and smaller peak wavelengths than stars of spectral type similar to the Sun, which is a G2V type star. Taking the upper limit of the stated temperature range, which is what is done when determining the temperature of the ionising stars in the simulations, and then the average radius to be around $15 R_{\odot}$ (Heap et al. 2006) O-type stars with these parameters have luminosities of the order $\sim 10^{32}$ W, whereas a solar-type star with $T_{eff} \sim 6000$ K would have luminosities of $\sim 10^{26}$ W. This tells us that massive stars with these temperatures would have significantly more ionizing effect and radiation-driven momentum due to the greater number of ionizing photons emitted from their surface. In addition to this, with a T_{eff} of 40,000 K, the peak wavelength for these types of stars sits within the UV band - around 72 nm (by Wien's Law).

By having a significantly shorter peak wavelength and higher total flux, massive O type stars can have a considerably greater effect on their surrounding environments- specifically the gas and dust cloud they are embedded within. Wavelengths within the UV are of comparable size to dust particles that sit amongst the gas (often less than $1 \mu m$), which leads to interaction with UV photons such as absorption and re-emission. This interaction with UV radiation also then prohibits the dust from coagulating to form larger dust particles around the massive star (Greenberg 1980). As well as this, the radiation can interact with the hy-

drogen and not only ionize it if the photon is of high enough energy, but also can transfer momentum to the atoms, giving them greater kinetic energy and potentially increasing the temperature of the surrounding region. The increase of gas momentum through UV absorption thus contributes to the growing pressure that the ionized region exerts on the cold outer gas at the ionization front.

As massive stars continually emit vast amounts of radiation from their surfaces out into the surrounding environment, surrounding gas particles that absorb the radiation become excited and/or ionised. These regions around the stars are dominated by molecular hydrogen, with small remnants of heavier elements such as carbon, oxygen, sulfur etc. These heavier elements are most likely products from older, extinct stars that had supernovaed long ago.

Spitzer & Arny (1978) first explained the full process of the expansion of an H II region, and is where part of our description will derive from. With the star in a model scenario emitting uniformly as a sphere, an ionisation front forms, where inside there is ionised hydrogen (H II), and beyond that is molecular hydrogen. When observed in multiple different lines, a definitive ring can be seen around the star where there is ionised hydrogen and H_2 . At the ionisation front, neutral and molecular hydrogen are ionised to form H II, and then due to the excitement and increase in kinetic energy, travels into the ionised region. As more hydrogen becomes ionised and travels into the region, the region boundaries expand further and further from the star. During this period, however, there is a continual process of recombination along with the ionization of the hydrogen gas. The consistent fluctuations of ionization and recombination assist towards leading to an overall thermal equilibrium within the region (maintaining an approximate 10^4 K). The hot gas of the ionised region puts increasingly more pressure onto the cold outer gas, and causes this cold gas to become denser. There is a second main process that occurs that keeps the system in equilibrium by allowing pressure inside the H II region to be released (this is known as Spitzer expansion is also discussed in the following section). The hot gas within the H II region seeks to escape through ‘gaps’, or weaker locations along the ionisation front, creating large outflows that travel through the cold outer gas and dust, as discussed in simulations by Dale et al. (2005), and demonstrated in early workings of these simulations by Dale & Bonnell (2008). The outflows occur where there is the least pressure acting upon the H II region, and this can lead to asymmetric and uneven ionization fronts. This therefore means that when observing an H II region, the massive star that is the ionizing source creating it may not necessarily be in the centre; it could potentially be anywhere in the region. The ionisation front is not uniform in density and structure for a culmination of different reasons - turbulence that leads to density perturbations, the slight differences in ionising power due to the small deviations in flux at different locations, and so on.

2.1.1 Strömgren sphere

H II regions are far from uniform and predictable, however trying to understand them from a simplified approach can help with understanding better the behaviours that occur. Strömgren (1939) developed a theory, later named the Strömgren sphere, that modelled a sphere of ionised hydrogen around a massive O or B-type star. Through a series of assumptions, it would be possible to determine the size of an initial H II region around a star with recombination equilibrium before thermal expansion or any other kind of expansion has oc-

curred, given the flux and recombination rate of hydrogen at the given temperature. The recombination rate is dependent predominantly on the number density of the gas particles in the region. The gas consists of just electrons and protons due to the fully ionised hydrogen. As such, we therefore know that because there is a 1:1 ratio of protons to electrons, the number density of protons will also be the same as the number density of electrons.

The theory assumes firstly that the region has evolved to be perfectly spherical, containing only fully ionised hydrogen and contains only a single central star. Within the sphere, the gas remains ionised due to the constant supply of photons that are continuously exciting the particles. Beyond the H II region, the photons have not yet reached these regions and thus protons and electrons remain combined. Therefore at the outermost edge of the H II region, where the hot and cold gas border each other, there is an equilibrium of ionisation and recombination. We can thus say that the radius of a Strömngren sphere is defined as the distance from the star to where there is a balance between ionisation and recombination.

The recombination rate of hydrogen, and all elements, is a collection of different rates dependent on the energy state the electron recombines into. The one exception lies with electrons that recombine and fall straight to the $n = 1$ state. Draine (2011) explains how an electron can recombine with a hydrogen nucleus (proton) to any energy level with the subsequent release of a photon with energy $E + I_{nl}$ where E is the kinetic energy of the electron and I_{nl} is the binding energy of the electron in that given energy level. As a result of this, for electrons going into the $n=1$ state, they instantly release a photon that is capable of releasing a Lyman continuum photon that can ionise another hydrogen atom. Because photo-dissociation around H II regions are relatively abundant in H I, these photons are immediately reabsorbed to ionise another neutral hydrogen atom. There is a distinction on whether the environment in which these events occur is optically thin or optically thick to the ionizing radiation, known as Case A and Case B recombination- demonstrated and introduced by Baker & Menzel (1938). Case A describes when the environment is optically thin to the ionizing radiation, such that every ionizing photon is able to escape the region, meaning that the capture rate coefficient considers recombinations to all energy levels, and Case B considers environments optically thick to the ionizing radiation and as such the recombinations to the $n=1$ level are ignored. For GMCs and H II regions, Case B recombination is considered and as such, we ignore the $n=1$ recombination and the recombination rate for hydrogen is given as the following summation, given in Equation 1.

$$N_R = \sum_{n=2}^{\infty} N_n \quad (1)$$

The recombination rate for hydrogen per unit volume per time can thus be given by Equation 2, recalling that $n_e = n_p$. Here, T_e denotes the temperature of the ionising region, and $\alpha_n(T_e)$ is the recombination coefficient for a given energy level. For the case of fully ionising hydrogen, the value is given as $\sim 2 \times 10^{-16} T_e^{-\frac{3}{4}} m^3 s^{-1}$.

$$N_n = n_e n_p \alpha_n(T_e) = n_e^2 \alpha_n(T_e) \quad (2)$$

From here, the recombination coefficient will now be denoted as $\alpha_H(T_e)$. Therefore, by multiplying by the volume of the Strömngren sphere, we obtain a value for the ionisation injection rate for the whole region. Considering that the single star is the only source of

ionising photons, it is the case that the injection rate of ionising photons, Q_H , of the star is the number of ionising photons per second multiplied by the volume they are injected into (being the same as the number of recombinations in the sphere). This leads to Equation 3.

$$Q_H = \frac{4\pi}{3} n_e^2 \alpha_H(T_e) R_s^3 \quad (3)$$

Finally, Equation 3 can be rearranged to find the radius of the Strömgen sphere in the ideal scenario of a perfectly spherical H II region, illustrated in Equation 4.

$$R_s = \left(\frac{3}{4\pi} \frac{Q_H}{n_e^2 \alpha_H} \right)^{\frac{1}{3}} \quad (4)$$

Despite a perfect Strömgen sphere being an extremely rare and unlikely celestial object to find, objects close to that shape have been observed, such as the Rosette nebula. An optical image of the Rosette nebula is given in Figure 1, where the near-spherical H II region can be seen at the centre of the denser gas.



Figure 1: The Rosette nebula in optical emission, displaying a near-perfect Strömgen sphere caused by a massive O-star. Image credit: Wang et al. (2010)

The Strömgen sphere identifies the point at which recombination and ionization are equal, however the radius can and will also increase to further radii via internal pressure

expanding the region up to a pressure equilibrium. These make up the two main factors that contribute to the expansion/sustained shell. As briefly mentioned earlier, a pressure equilibrium is obtained through the balance of the internal pressure of the ionized gas with the cold outer gas beyond the ionization front. The Strömgren sphere defines the radius for ionization/recombination equilibrium and is described as the initial stage of H II region expansion, but internal pressures of the hot gas (which can equate to up to 200 times more than the pressure of the cold gas (Bisbas et al. 2015)) further expand the radius of the ionization front, bringing the size of the bubble to larger than R_S . This expansion decreases the density within the sphere and as a consequence leads to a drop in recombination rate. This rather sudden reaction to the intense pressure within the cloud triggers a shock response in the cold gas, sending a shockwave through the cold gas ahead of the ionisation front; brought about through the fact that the shock front travels with a speed greater than the sound speed of the cold gas. This is inherently found through the sound speed of the ionized region being higher than that of the neutral gas. This series of processes defines the intermediate stage of H II region expansion.

The final stage of the expansion now refers to the pressure equilibrium mentioned. This is a very unlikely equilibrium to reach in real environments due to the multitude of other factors such as outflows from the ionization from the surface leaking hot gas and the irregular shape and make-up of the ionization front. This occurs in model scenarios, however, through the balance of ionization pressure to the pressure of the cold surrounding region. The temperature of the ionized gas at the ionization front is $10^4 K$ and the cold neutral gas has lower temperatures of approximately $100 K$ (Goldsworthy (1958), Axford (1961)). Considering again that the pressure inside the H II region is 200 times larger than the pressure acting inwards (Bisbas et al. 2015) we can determine the ratio of the number densities in both regions. P_i , n_i and T_i refer to the pressure, number density and temperature of the ionized region respectively.

$$P_i = n_i k T_i, P_n = n_n k T_n \quad (5)$$

$$\frac{n_i k T_i}{n_n k T_n} = 200 \quad (6)$$

And given that $T_e = 10^4 K$ and $T_n = 100 K$:

$$\frac{n_i}{n_n} = 2 \quad (7)$$

Given this, by equating the pressures at equilibrium between the inside and outside of the region, we obtain a final value for the ratio of the number densities before and beyond the ionization front, illustrated in Equation 8. Here, n_f is the final number density inside the bubble.

$$2n_f k T_f = n_n k T_n \Rightarrow n_f = \left(\frac{T_n}{2T_f}\right) \approx 0.005n_n \quad (8)$$

Substituting this into the equation for ionizing flux, as previously seen in Equation 3, equating it to the flux at the Strömgren radius and rearranging for radius gives a final radius in the region of approximately $34 R_S$.

2.1.2 H II region classification

It has long been suggested, as well as being a concrete prediction from the Spitzer expansion model, that smaller H II regions are younger and larger H II regions are older (Peters et al. 2010). This hypothesis is accurate within a given time frame, as H II regions do expand as the massive stars continually emit radiation. Observers have tended towards using a size-dictated category system for defining H II regions, which has been split into 4 distinct classes and is seen as an evolutionary sequence that H II regions morph through. The smallest observed H II regions are Hyper-compact H II regions (HC), followed by Ultra-compact H II regions (UC), then classical-type and finally giant-type H II regions. The sizes of these regions are given as $R(\text{classical}) \geq 1$ pc, $R(\text{compact}) \leq 1$ pc, $R(\text{UC}) \leq 0.1$ pc and $R(\text{HC}) \leq 0.05$ pc. The largest of H II regions (being classical-type) have radii (in rare cases) of upwards of 300 pc (Ye 1992), and hyper compact regions as small as 0.01 pc. Ultra-compact and Hyper-compact H II regions have been observationally studying numerous in works such as Leto et al. (2009), where 7 mm continuum emission was collected through Planck and as such a detailed study of their size, as well as dust distribution content and ionized gas emission was carried out. Churchwell et al. (2010) also conducted observations of 30 UC and HC H II regions in multiple molecular lines. Churchwell (2002) states clearly that UC and HC H II regions are not definitively the earliest stages of massive star formation. They display strongly radio and NIR emission, which is indicative of protostars and early star formation, and also contains the reprocessed radiation by the dust surrounding the newly forming massive stars. An H II region is classified as a UC H II region if, as well as the radial condition, have an electron density of $\geq 10^{10} m^{-3}$. Likewise, HC H II regions are defined by also having an electron density of $\geq 10^{12} m^{-3}$. These regions correspond, most likely, to single or a few stars at most forming within a dense clump of gas and dust. Like other H II regions discussed, UC and HC regions occur only through the presence of massive stars, and it is probable that they are the result of a massive star forming within a circumstellar disc and as the star becomes hotter and larger, its ionising capabilities increase and allow for it to produce larger and more out-stretched ionised bubbles; with assistance from other massive stars within the nearby vicinity that may have form at similar times.

During the early stages of massive star formation and at the time when UC and HC H II regions would be in existence, H II regions have been found to ‘collapse’. The bubbles themselves do not literally collapse under the pressure of the cold gas, but instead it can sometimes be the case that there are not enough ionising photons to maintain the ionisation of hydrogen atoms, leading to recombination at the ionisation front and as such a shrinking ionised bubble radius. This can occur from the accretion of material onto the star through the H II region, and if enough neutral material from outside enters into the ionised region then the majority of ionising photons can be consumed by this accreted material and consequently leads to a lack of maintenance in ionisation at the bubbles radius. This has not been observed or simulated to occur at later stages of the clouds evolution, however it can lead to the misleading conclusions of mistaking a collapsed (and I continue to use this word as it best describes what physically looks to be happening) UC H II region, and consequently misguide observers to believing they are younger than they actually are, and aligns with the belief that a smaller H II region correlates to a younger region. Fortunately for observers, the age differences between HC and UC regions is not significant, and therefore they will both have

young massive stars and the early stages of bubbles forming, but it may be important to have observable tracers beyond shape and size to identify these as it is possible for mechanisms within to lead to a mis-classification. Figure 2 gives a simplified illustration of how feedback from massive stars leads to ionisation fronts and cloud collapse.

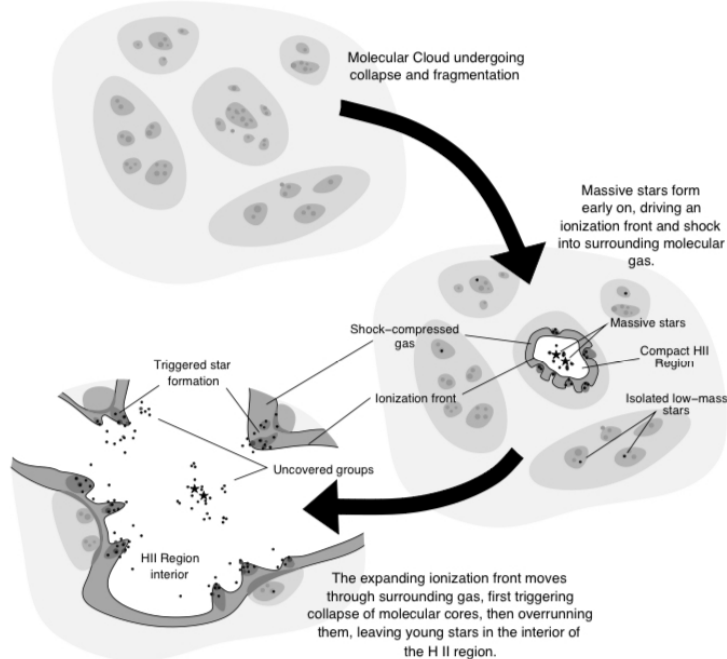


Figure 2: Evolution of an H II region formed by massive stars from Hester & Desch (2005). Here it is seen that the formation of lower mass stars is considerably affected by the expanding H II region around the massive stars; terminating some of the lower mass stars, but possibly triggering the formation of others by sweeping up dense gas.

2.2 Star formation

Some of the best conditions for star formation are molecular clouds, and for massive stars to form within embedded clusters, the mass of the molecular clouds is found to have the lower limit of $> 10^3 M_\odot$ (e.g. Dale & Bonnell (2008)). The turbulent and disruptive processes in the clouds lead to varying densities within regions, with higher densities having higher gravitational influence and thus collapsing on these regions. Molecular clouds can host star formation at multiple different stages in their life, and due to a number of different systems at work within them such as the sweeping up of cold gas by stellar winds or thermal pressure to form dense clumps. The Jeans mass defines the maximum mass, given the temperature and density, that a cloud can be stable and resist gravitational collapse (without re-expansion) is given in Equation 9, and is derived from the original Jeans Length from Jeans (1928). In this equation, k_B is the Boltzmann constant, μ is the mean molecular mass (assumed to be 1), m_H is the atomic mass of hydrogen, G is the gravitational force constant, T is the temperature and ρ is the cloud density. As the cloud fragments and turbulence leads to density irregularities, regions of the GMC exceed their local Jeans Mass and thus become

candidates for forming a star.

$$M_J = \left(\frac{81}{32\pi}\right)^{\frac{1}{2}} \left(\frac{k_B}{\mu m_H G}\right)^{\frac{3}{2}} T^{\frac{3}{2}} \rho^{-\frac{1}{2}} \quad (9)$$

H II regions are not ideal environments for star formation due to the higher temperatures, higher kinetic energies per particle and therefore higher virial ratio for the local region. However, it is the indirect result of H II regions on their surrounding environments that creates ideal nurseries for such events to occur - referred to as triggered star formation (Gritschneider et al. 2009). As formerly discussed in Section 2.1, the outward pressure from the stellar feedback of the massive stars, as well as the hot gas outflows from the leaking H II region, cause the outer colder gas to become more dense and potentially locally collapse. In addition to this, with the ability for these areas to remain isothermal and dense during the evolution of the ionization, they remain ideal star forming environments for long periods of time. This is, however, dependent on whether the cloud is initially bound or unbound as these cold areas will dissipate if the cloud was not bound to begin with. Furthermore, multiple simulations from Dale et al. (2014), Dale et al. (2012), Dale et al. (2013) and more have illustrated how regions of cold gas outside of the photoionising bubble and outflows can survive for long periods of time (depending on the number of ionising stars, size of the H II region and subsequent star formation). This creates the possibility of prolonged survival of dense and cold gas and dust regions forming new stars within them before a significant amount of feedback could terminate them. We see how this affects star formation later in Section 7.4, and whether the H II region supports star formation outside of its boundaries due to the aforementioned dynamics.

2.2.1 Termination of low-mass star formation

Massive stars and the formation of H II regions can also hinder star formation during the earlier stages of a molecular cloud's evolution. As Figure 2 demonstrates, during the very early stages of the formation of massive stars, low mass stars ($< 2 M_{\odot}$) also begin to accrete gas and dust around these more massive stars. Garay & Lizano (1999) discuss how massive stars begin affecting their environments much faster than lower mass stars due to their relatively short Kelvin-Helmholtz timescale; being just $\sim 10^4$ Myr. After this time, outflows and stellar feedback in the UV emerge from the massive core (Garay & Lizano 1999) and begin ionising and dispersing surrounding gas. The winds and photoionisation are also powerful enough to be able to completely destroy low mass nearby stars that are still in the early stages of their cores forming. The winds especially can destroy accretion flows onto the forming stars, and these processes can have effects on not only low mass stars, but also intermediate mass stars in the mass range of $2 < M < 8 M_{\odot}$.

2.3 Virial Ratio

The virial ratio, also referred to as the virial parameter, is an effective way to determine the stability of a system against gravitational collapse, and is mathematically useful for both simulation and observation work. The virial theorem defines that, for a idealised spherical model that is both governed by its own gravity and stable, the total kinetic energy contained

within the sphere is $-\frac{1}{2}$ of the gravitational energy. By stating that the gravitational potential energy for a perfect sphere is equal to Equation 10 (Bertoldi & McKee 1992), where M is the total mass of the cloud, R is the radius of the cloud and G is the gravitational force constant, it thus follows that the kinetic energy would consequently be equal to a $-\frac{1}{2}$ of this, illustrated in Equation 11.

$$E_{GPE} = -\frac{3}{5}G\frac{M_{tot}^2}{R} \quad (10)$$

$$\frac{1}{2}M_{tot}v_{rms}^2 = \frac{3}{10}\frac{GM_{tot}^2}{R} \quad (11)$$

In Equation 11, the root mean squared velocity refers to the total averaged velocity of all particles within the cloud (specific to the use in this work). It is more common convention within astronomical observations now to use the virial parameter α , which is expressed in terms of measurable parameters in Equation 12 and was first introduced by Bertoldi & McKee (1992). This version derives from the same principles as above but instead describes the three dimensional gravitational energy of the cloud to be that of a uniform sphere ($\frac{3GM^2}{5R}$) and that each of the three perpendicular directions contain the same kinetic energy such that it can be described as $\frac{3}{2}M\sigma^2$. A full description and discussion of the virial ratio can also be found in Bertoldi & McKee (1992). Given this and the virial theorem, we obtain the parameter result.

$$\alpha \equiv \frac{5\sigma^2 R}{GM} \quad (12)$$

Here, σ is the line of sight velocity dispersion. With the ability to predetermine all of these variables, it is possible to either accurately and precisely calculate the virial parameter for a given cloud, or, create a cloud with a given mass and radius and thus give it a specific velocity dispersion for a desired virial parameter.

The virial parameter is a key indication to whether a molecular cloud is gravitationally bound or not, as the level of self-gravity that exists with a system can lead to different behaviours, star formation efficiencies and the ways in which H II regions can evolve. Bertoldi & McKee (1992) state that for ‘*equilibrium interstellar structures, if strongly self-gravitating and supported by thermal pressure, have virial ratios of order two or somewhat higher; for instance, $\alpha_{cl} = 2.1$ in the critical Bonnor–Ebert sphere*’ (n.b.- A Bonnor-Ebert sphere is the largest mass an isothermal sphere composed of gaseous compounds can have whilst still being in a state of hydrostatic equilibrium (Ebert 1955)). This gives a reasonable threshold for the point at which a cloud is bound under its own self gravity, or has enough kinetic energy to overcome large-scale gravitational collapse or binding. The characteristic of isothermal gas within the bubble is also key, as it is found repeatedly that the net result of radiation injection from the massive stars, escape of radiation and the ionization/recombination of the hydrogen, is at thermal equilibrium with the gas. This can be, in part, maintained by the level of expansion from the bubble and its resulting impact on the internal gas.

This thesis includes simulations of star formation and feedback from giant molecular clouds, which are denoted Run I, J, T, M, Q and P. Each simulation type is discussed in more depth in Section 5.3, however each of the molecular cloud types has a different viral

ratio. For Run I and J, the virial ratios are the same, at a value of 0.7. This implies that the clouds have a low initial kinetic energy and are thus experiencing a more dominant gravitational influence. In these simulations, however, the virial ratio is given the simplified definition of the ratio of kinetic energy to gravitational potential energy. The advantages of this is to give a less abstract cross comparison on how bound and unbound clouds behave, since we do know to a considerably higher accuracy than an observer may be able to deduce, the energies within the system. Run T on the other hand, has a very different virial ratio, being a much higher value of 1.9. As a consequence, the cloud has much higher internal kinetic energy that is dominant over the gravitational energy attempting the hold the cloud together. Run M has the intermediate value of 1.5, which lies in the middle of all virial ratio values used in the studied simulations. Run Q has the highest virial ratio value out of all the simulations - being 2.3, implying that the cloud has a very high kinetic energy and is unbound for this reason.

These initial conditions give an insight as to how the cloud may evolve and behave, and basic predictions can be made. With higher virial ratio, we expect that clouds exist in a more unbound state, and are more free to expand. The resulting impact is a probably lower star formation and star formation efficiency, as well as larger structure over long periods of time. The opposite can be predicted for clouds with lower virial ratios. The physical properties of the clouds has to be taken into consideration though, due to the fact that a smaller cloud does not inherently mean that the cloud has a lower virial ratio.

3 Previous Observational work

The amount of observational work that has been conducted on molecular clouds is far beyond that which I am able to mention in this work, and thus only key work that is highly integral to the objectives in this work will be discussed. It is further helpful to hold cross-comparisons between simulation images and data and observational work. Specifically, the focus will be held around looking at velocity data, morphology and evolutionary age, and spectral energy distributions.

Being able to trace specific processes that occur within molecular clouds is a very difficult and often unsuccessful task in the field of observational physics. Chira et al. (2019) mentions how in molecular clouds there should be visible indicators/tracers of each potential process that could be driving the turbulence, but in spite of this, these tracers are either not observed at all or are too ambiguous to decipher. Even more so, these tracers may be visible within simulations and suggest a flaw with observational methods or instruments, but this only adds to the necessity of having high performance observational equipment that can confirm or dismiss predictions.

3.1 Integral field spectroscopy and MUSE

In more recent years, a wealth of data has come from the utilisation of MUSE- the Multi Unit Spectroscopic Explorer. MUSE is the next generation of observational instruments for the VLT and used by McLeod et al. (2015), for example, to obtain new information about structures within H II regions.

MUSE uses both integral field and adaptive optics to provide a wider field of view, while at the same time giving a higher spatial resolution. Integral field uses a grid of pixels, where in each pixel the photons received by it are passed through a spectrograph and consequently produce a spectrum. This therefore allows the instrument to know how many photons of each wavelength hit each pixel. MUSE uses 24 sub-fields that each use adaptive optics, with the adaptive optics being the component that allows for the high resolution, and the collective ability of the sub-fields giving the wide-angle field of view. The signal from the sub-fields is then fed into a spectrograph where the signal is split into wavelengths, allowing for a spectrum to be detected as opposed to a single beam. Further to this, with the Narrow Field mode being able to operate with a field of view of 7.5×7.5 arcsecs (Bacon et al. 2010), MUSE is more ideally suited for the study of properties of H II regions where smaller scale kinematics are to be studied across wider spatial scales. Especially given the fact that regions such as M16 (Eagle Nebula) has an apparent size of ~ 5 arcmins (Morales et al. 2013).

Understanding what observational instruments are capable of, and knowing the extent of what they can obtain, is vital in being able to develop methods that can be used by observers and are not far beyond where technology currently lies. As demonstrated by the wealth of work done on H II regions using MUSE, it has created a vast new potential for learning more about H II regions. As well as this, the simulations in this work contain H II regions on the order of ~ 15 parsecs, which is of comparable size to M16 where the Pillars of Creation are located (The entirety of M16 spans across approximately 20 pc, with the pillars having a size of 0.1-1 pc, determined from the Messier Catalogue). Given that MUSE has been extensively used to study these regions and that the features in this works simulations are of scales ~ 0.1 pc and upwards, MUSE would be an ideal instrument to conduct the later mentioned methods.

3.2 Morphology and ageing

Studying the shapes of H II regions is one of the easiest methods we have, as this is (currently) done largely by what we see with our own eyes from telescope imaging. Although this lacks methodical techniques, it can be highly indicative of how evolved the region is, and also an insight into the level of star formation present. Relaño et al. (2013) developed a basic morphological class structure of H II regions that was based around the shapes and structures of the bubbles. The four categories were *clear shell*, *shell*, *mixed* and *filled*, and are demonstrated by Figure 3 taken from Relaño et al. (2013). For many cases, these shapes will also relate to the age of the H II region and thus be a good estimator for the age of the stars within the cloud. By looking at Figure 8 in a later section we can see how the simulated clouds develop from a filled region, to a mix of forming bubbles and dense regions, to fuller shells and eventually cleared shells. These shapes thus coincide with the ages of the clouds, and may therefore be indicative of the evolutionary stage and age.

Further to this, ageing an H II region can be an abstract task, as the point at which an H II region ‘begins’ is not definite nor obvious. Currently, the main method for ageing H II regions comes from the study of the stars within them and fitting isochrones to Hertzsprung-Russell diagrams (HRD), and using the age of the stars as the indicator for how old the H II region itself is. A survey of colour against luminosity for all the stars in the cluster are found and plotted, and this gives an insight to how far along the stellar evolution is and as

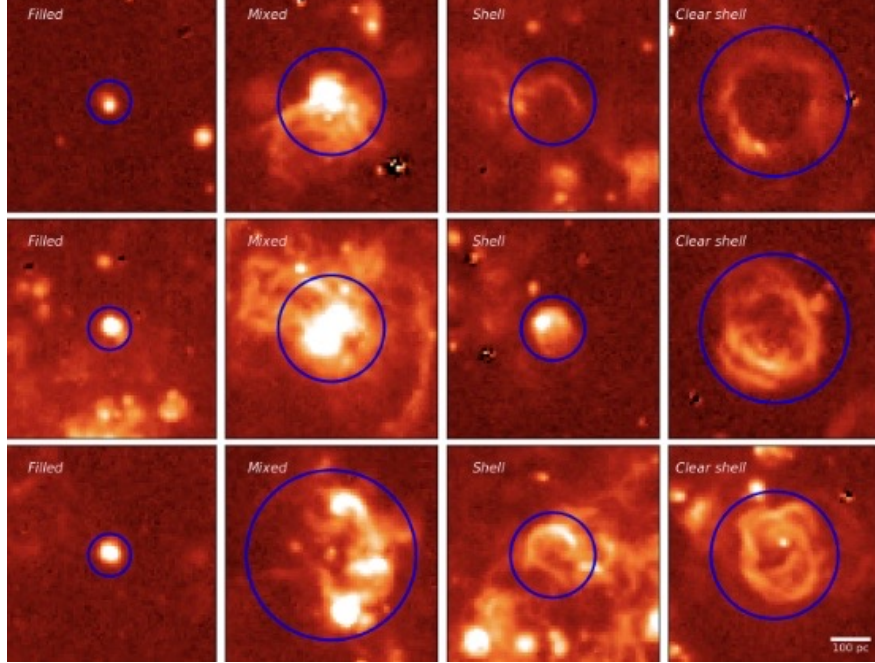


Figure 3: Examples of real H II regions and the class they belong to from Relaño et al. (2013). Each column represents a different classification and gives three examples of what may constitute each of such classes- labelled in the images.

such gives an estimate for the age. This is a reasonably good approach to ageing for H II regions where we can take a good census of the stars present, however for regions that are considerably further away, this may not be possible. This is because the regions are so far away that the individual stars that exist within them cannot be resolved, thus meaning that the number of stars, types and the luminosity of each individual star are unknown. Even more so, Siess et al. (2000) found that isochrone fitting for ages $< 10^6$ Myrs for massive stars gave large discrepancies, which is due to the isochrone fitting method not taking into consideration the effects from interacting binaries - which is significant given that a large portion of massive stars in H II regions exist in binaries. New methods pose very challenging obstacles to overcome, and there are currently no reliable methods for ageing the H II regions specifically. Stevance et al. (2020) have developed a new ageing method that incorporates massive star binaries and looks at spectral synthesis models to then compare to HRDs. This method produces stellar evolution models that include the binary systems that have led results astray in previous methods.

Dynamical ages of H II regions can also be determined, which come from the reasonable assumption that H II regions undergo constant expansion. If one can calculate the expansion velocity of the region and the radius of the bubble, then the dynamical age can be approximated by Equation 13 where R is the measured radius of the region and v_{exp} is the expansion velocity. Alternatively, considering that measuring the expansion speed of the bubble can be a difficult task, the ionised sound speed can be used instead, as the cloud expands a roughly the sound speed (which is typically $\sim 10 \text{ km s}^{-1}$).

$$\tau_{dyn} \sim \frac{R}{v_{exp}} \quad (13)$$

These regions can have multiple epochs of star formation over many millions of years, and can greatly change the shape and structure of the cloud dependent on the level of star formation. This could lead to the possibility that later formed stars could be mistaken for the stars that created the regions and therefore by ageing the region from the stars alone would give a false result. This mistake may not happen easily as it is highly unlikely that you would find newly formed massive stars within an H II region itself, but massive stars that have been burning on the main sequence or have moved onto the giant branch may have created their own H II region within their embedded cloud that has encompassed older bubbles. As such, the task of ageing is more of an interpretation, or how the observer chooses to define $t=0$.

4 Turbulence

Throughout the entire system of the H II region and surrounding cold gas, turbulence disrupts, distorts and transports gas and dust on both small and larger scales. Molecular clouds contain many different processes that contribute to the turbulence present within them, and as well as this, multiple external processes can have indirect effects on these molecular clouds and maintain turbulence. Further to this, the occurrence of turbulence can either assist star formation within a cloud or destroy star formation altogether, depending on the scales it works. A vast amount of research has been done in an attempt to define and quantitatively study turbulence. In the following section its causes and methods of measuring it will all be discussed, followed by a more in-depth discussion of the methods used in our simulations.

4.1 Quantitatively analysing turbulence

4.1.1 Larson's relations

Turbulence is a complicated process that is very hard to mathematically quantify and describe. The famous Larson's equations describe turbulence in molecular clouds, illustrated by Larson (1979) and then observational confirmed two years later by Larson (1981). Numerous further observations have been made that also confirmed the relationships, and these equations describe, or more likely act as distinct signatures of turbulence in molecular clouds (Vázquez-Semadeni et al. 1998). The first of Larson's relations, given in Equation 14 describes the virial state of the cloud on whether it is likely to collapse.

$$\langle \Delta v^2 \rangle \sim \frac{GM}{R} \quad (14)$$

The second of Larson's relations describes the velocity dispersion in molecular clouds as a power law, given in Equation 15. This gives a clear indication that the turbulent spectrum and the measured line width of a molecular cloud is connected to its size.

$$\langle \Delta v \rangle \sim R^p \quad (15)$$

The third of Larson’s relations shows just that the number density declines with increasing cloud size, shown in Equation 16

$$\langle n \rangle \sim R^{-q} \quad (16)$$

For Equations 15 and 16, p and q are empirically determined to be approximately 0.4 and 1.1 respectively. For the second relation, p can also be expressed as $p = -(n+1)/2$. The turbulent eddy energy spectrum is defined as $E(k) \propto k^n$, where k is the eddy wavenumber, and for Kolmogorov energy spectrum (which describes the turbulence in an in-compressible, non-magnetic cloud), where it is expected that the energy of the turbulence increases with distance, $n = -5/3$. This gives a p value of $1/3$, which is close to the empirically derived value.

4.2 Turbulent processes

There are multiple processes that contribute to turbulence, and these vary in the scale of the turbulence they cause. It is widely argued about which processes may be dominant in maintaining turbulence, however it is true that all processes can have some effect on the turbulent structure of molecular clouds.

It is important in this project to consider what processes lead to the dominant turbulent effects due to the fact that those which are considered to be highly contributing can be implemented, while others that may be considered negligible can be ignored. Additionally, it further assists in describing a more accurate and representative turbulent structure. In these simulations, turbulent processes are limited to some of those which would only exist inside the cloud, and also those that can be considered to be dominant. Not all internal processes are included, for example protostellar jets that eject from the forming stars.

Left unperturbed it would be expected that turbulence would, over time, dissipate and die out. As such, at large spatial scales we would expect the turbulent kinetic energy of the gas to be distributed and transferred to the point where it is negligible. However this is not the case with true turbulence in molecular clouds. Multiple different mechanisms can contribute to the maintenance and continuity of turbulence within a molecular cloud that are both internal and external. Driving forces such as the shockwaves from nearby supernovae and galactic shear can act as external mechanisms that maintain turbulence, with internal processes such as local gravity, magneto-hydrodynamics, molecular outflows and H II region expansion also contributing to turbulence. Many works have suggested that magneto-hydrodynamic mechanisms are insufficient for slowing turbulent decay. Oishi & Low (2006) used 3D, two fluid magneto-hydrodynamical codes to study the influential effects of ambipolar diffusion on its ability to cause clumping and small scale structure in turbulent clouds, and found conclusively that ambipolar diffusion was insufficient in changing the clump structure and have any influence scaling for gravitational collapse. Returning to the understanding that turbulence decays within the timescale of the crossing time of the cloud described in Equation 13, where R is the radius of the cloud and v_{RMS} is the root mean square velocity of the gas in the cloud. It has been suggested that magnetic fields could sustain turbulence for longer than the crossing time, however Mac Low et al. (1998) demonstrated that magnetic fields fail to maintain turbulence for significantly longer than the crossing times. Consequently,

this illustrated that they could not be a substantial mechanism for assisting turbulence and suppressing shocks. Brunt et al. (2009) found that, from observation samples, it was large scale external mechanisms that best describe the turbulent nature seen, and that small scale processes played a significant role only within the central cores of the clouds.

4.3 Structure function

The structure function is a method originally developed for the implementation of turbulence, and presented for use in turbulent clouds by Elmegreen & Scalo (2004) (where a full indepth description of what a structure function is and how it is derived can be found) and implicated into the understanding of turbulence in giant molecular clouds by Boneberg et al. (2015) as a way to quantify and investigate the evolution of turbulence from small scales to large scales. Mathematically, the structure function looks at how the energy of particles within a region change with increasing spatial scales with respect to numerous centre-points. Through the repeated iteration of this and subsequent averaging of the results, a relative velocity/spatial scale relationship can be drawn for the whole cloud. This comparison between a centre-point and the particles around it is carried out multiple times (on the order of thousands), and then averaged over the number of structure functions found.

As discussed in Section 4.2 earlier, due to multiple processes and mechanisms present, turbulence is maintained and driven within the clouds over considerably longer periods of time than may have previously been expected (crossing time etc). The turbulence for non-magnetic, incompressible fluids is described by the Kolmogorov power spectrum, so being able to recover a structure function that describes an energy spectrum with a similar power law would indicate that the turbulence in our clouds 1) does follow a Kolmogorov-type turbulent field and 2) would imply that the small scale turbulent mechanisms implemented in these situations are sufficient to provide the driving forces. One note to add is that although Kolmogorov’s theory was developed around incompressible fluids, it still offers to us a good description of turbulence found within compressible gasses

In practice, the velocity of the reference cell will be denoted as v_0 , and for every other particle, i , the structure function (given as $S(dv)$) is defined as $S(dv) = (v_i - v_0)^2$. The structure function is kept at second order to stay in line with the work carried out on the same simulations by Boneberg et al. (2015). Around the centre particle, radial bins are placed such that for every bin, a value of $S(dv)$ can be found that is the average of all particles in that bin. MOCASSIN, the radiative transfer code used to produce synthetic observables in this thesis, uses a cartesian grid, and since cartesian grids were being used I decided to start with bins that are square for computational efficiency. Figure 4 gives an illustration of how the bins initially looked in the work done in this project, and also highlights why it is easier with this method due to the grid structure of the simulations. The effect on the structure functions obtained should not be substantial, but low amounts of systematic error-like features may be present.

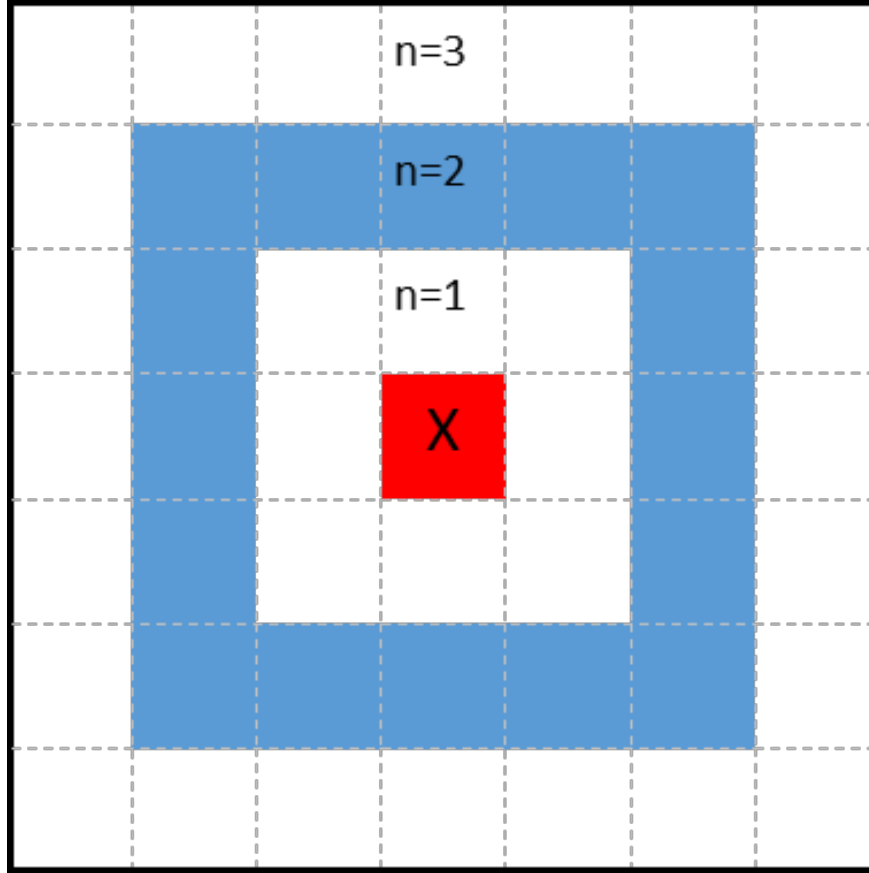


Figure 4: This figure gives a demonstration of how bins were defined when producing structure functions. With increasing values of n , a greater volume of the simulation is considered for each bin. The red cell in the centre signifies the cell that has been selected for deriving a structure function around, and the blue region identifies the $n=2$ bin.

After working with structure functions computed this way, I then adapted the code so that it could make circular bins around every point. Despite this method taking longer, it would lead to more accurate results, as this is how previous structure functions have been produced in other work such as Chira et al. (2019) and Boneberg et al. (2015). If, however, through cross comparison the results between the two shows strong similarities then it may be possible to use simpler square bins as an equally sufficient but time-saving method. In Figure 5 an image of Run I is given with a series of bins increasing in radii. This is how the new method's bins look and how they differ with increasing radius. Additionally, with this approach only 20 bins are used as opposed to the significantly larger 128 bins of the square method.

A further factor that will affect the outcome of the structure functions I obtain will be due to whether the bins are volume weighted or density weighted. Chira et al. (2019) undertook extensive work on structure functions of simulated molecular clouds and used density-weighted structure functions. The advantage of using a density weighted structure function is that if there are few particles within a bin (which can be due to a multitude of reasons), and they have abnormal velocities that are astray from the general trend, they will not dominate or strongly change the results. The disadvantage, however, is that data

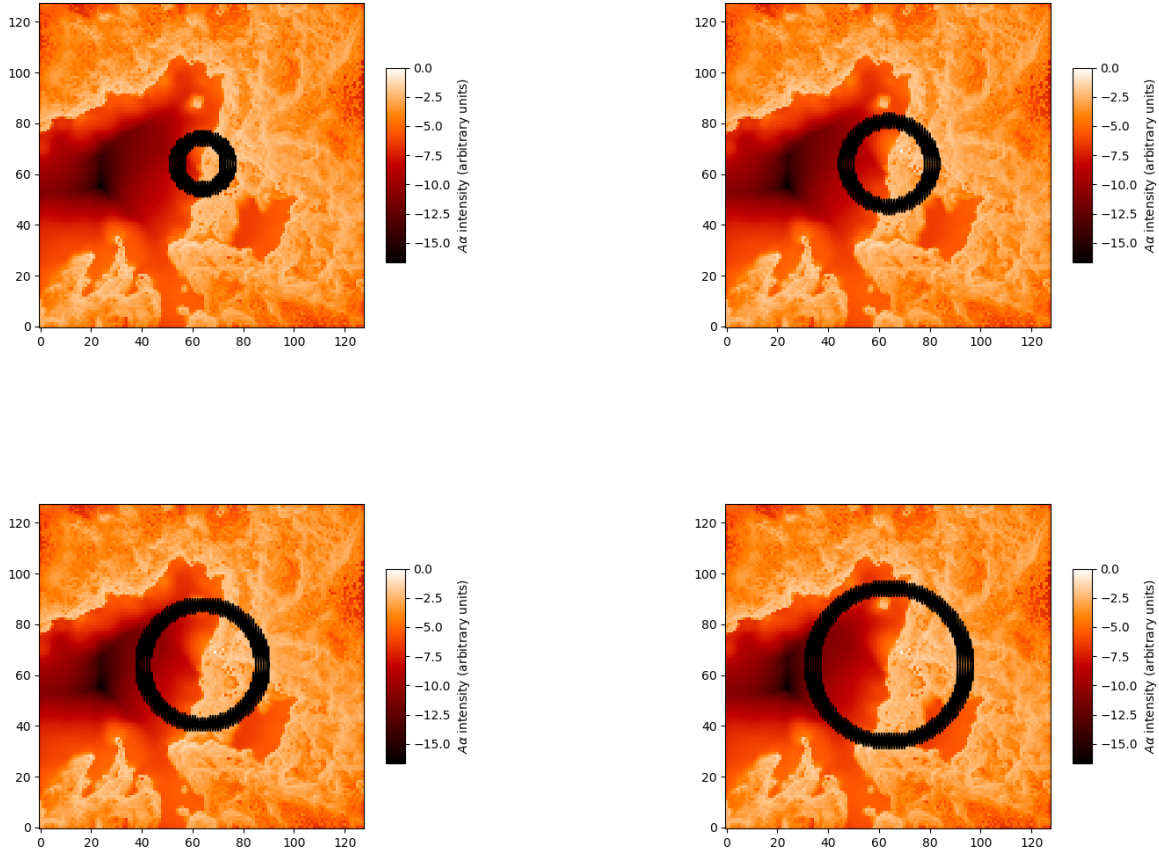


Figure 5: This demonstrates increasing radial bins centred on a central pixel- highlighting the size and workings of the circular bins. In practice, these bins will be positioned in 10^3 different positions and values for each radial distance averaged together. The bins continue out to a maximum radius of 15 pc, and pixels in a bin that lie outside of the bounds of the image are ignored.

collected will be bias towards denser regions and therefore to specific directions, or in regions where there is an H II region and ionisation fronts, it will be the ionisation from these fronts that will almost fully dominate the data. The SPH simulations are inherently density weighted, however when we superimpose a 3D grid upon it we apply a volume-weighted method to a density weighted simulation. The consequences or general effects of this are not fully understood and lie beyond the scope of this project.

Turbulence is not a uniform process, and as you explore along a molecular cloud there are different processes that dominate at different points, and it is not so that the turbulence in one area of a cloud or H II region is necessarily causally connected to that of another region of the cloud. Consequently, it is ideal that we are able to study the structure function of a single H II bubble, as the simulations used are very complex in shape, structure and turbulence. McLeod et al. (2015) produced structure functions of the Orion Nebula using MUSE through the use of four emission lines - $H\alpha$, [O III], [N II] and [S II]. Velocity data cannot be obtained on its own due to the obvious lack in being able to measure individual particle velocities. Therefore, the velocities have to be extracted from emission. The output of MUSE is fed through a pipeline that then studies the Doppler shifts within known lines to gauge a value for the line of sight velocity. It was found that for $H\alpha$ and [O III] the structure function, to a reasonable level of accuracy, a smooth positive increase was evident that may support a Kolmogorov-type power law. In contrast to this, for the [N II] and [S II] the trend follows a more horizontal relation that is indicative of high noise and/or chaotic velocity behaviour. It is unfortunate that this is a consequence of attempting to observe and derive a structure function if exposure time isn't sufficient or longer exposure times are not possible, however given that [S II] is a strong tracer of the ionisation at the ionisation front and elsewhere is weaker, it may be advantageous to only focus on $H\alpha$ and [O III], as well as comparing how what is found in these emissions with the raw velocity information. Furthermore, results given by McLeod et al. (2015) were measured across smaller spatial scales relative to the simulations given in this work. Whereas their structure functions covered up to close to 1 pc, ours extend out to 15 pc, and this relates back to previously discussed comments in Section 3.1 where it was noted how the scaling of methods from small to large scale could benefit observational data. By retrieving a similar or same power law in both a small scale and large scale environment would highlight the use of these methods on instruments that do not have a resolution as high or field of view as small as that of MUSE - being the instrument used in the aforementioned work for the structure functions.

5 Methods

5.1 Radiation hydrodynamic simulations

The simulations used in this project come from Dale et al. (2014) and Dale (2017), which were performed with a Smoothed Particle Hydrodynamics (SPH)/N-body code. The code for these SPH simulations is described in depth by Bate et al. (1995). The molecular clouds initially begin with a smooth Gaussian density profile, in such a way that the density at the centre is three times higher than that at the edge (all dynamical properties are given by Dale et al. (2014)). These simulations were created with the purpose to examine the effects

of stellar feedback on clouds with varying mass, radii and turbulent velocity dispersion. The idea behind this is to assist with the objective of determining characteristic properties of H II regions, including their initial conditions, with key observable tracers.

Smooth particle hydrodynamics is a computational method to model fluid flows in three dimensions. The first SPH code for astrophysical purposes was presented by Gingold & Monaghan (1977) and was used in the application of several polytropic stellar models. SPH codes tackle the problem of modelling mesh-free, continuous fields containing a finite number of particles that possess the properties of the field. Each particle not only exists as itself (analogous to a 3D Delta function), but also has a sphere of influence around it. In 2D, this can be imagined as instead of describing a point as a delta function, we instead describe it as a Gaussian function where particles can overlap and influence each other. This is known as the kernel function. Furthermore, with each particle having its own field of influence, the accumulation of all the fields gives the total fluid an overall field - thus a fluid composed of many small interacting particles, and implies that multiple particles nearby can act as a single function. The particle's properties are responsible for the dynamics of the fluid. Altering their kernel radius and the distribution of them can completely change the behaviour of the fluid. Increasing the intensity of the kernel function can increase the sphere of influence around the particle, which would be like increasing the gravity of an individual particle in an astrophysical simulation. Kernel functions are therefore important to refine when using in simulations such as these as they have to accurately represent gravitational potential wells and in the initial conditions, there is complete freedom choosing the velocities and distributions of the particles. Thinking of kernel functions in the context of gravitational potential wells, given the sphere of influence of each particle, those close together are going to be more bound to each other than those further apart.

A selection of criteria is laid out in order for the successful collapse of particles into a sink particle that will represent a star. It is widely known that a star cannot form simply by the present gas and dust having a high-enough density. There are a plethora of factors that govern whether a star can form or not. These simulations deal with those that are the most dominant and influential in the formation of stars, and in order for a sink particle to appear, strict criteria must be met. The first criteria to trigger whether a particle is a candidate for becoming a sink particle is the local density around it. From this, the code then determines the particles local Jeans mass and whether it exceeds this. As we have already discussed and explained, the Jeans mass defines the mass for a given radius, density and temperature at which above this the cloud will undergo gravitational collapse. The code then looks at the divergence in the velocity field ($\nabla \cdot v$), as this needs to be negative as this implies that the object is indeed contracting. Then the total energy of the local systems is checked. The four energy parameters that contribute to the binding or liberating of the particles is the gravitational energy drawing them together, and the thermal, kinetic and rotational energy which acts to overcome gravity. The sum total of the gravitational, thermal and kinetic energy must be negative in order for gravity to be the dominant force and thus causing the particles to collapse in on each other. The gravitational force must also be larger than the rotational energy as collapse can be halted or interrupted by large angular momentum tearing the collapsing cloud apart.

These simulations consider only internal mechanisms for driving turbulence within the clouds. They ignore any galactic effects or nearby supernovae, and also do not implement any

magnetic fields into the clouds which, as already discussed, should not lead to any noticeable differences in the energy spectrum. As such, the only driving forces for the turbulence come from the expansion of the H II region (linked in with the stellar feedback from the stars), as well as an initial Kolmogorov-type turbulence field set at the beginning of the simulation. The simulation also does not run for long enough to allow for the supernova of any of the stars.

5.2 Monte Carlo and calculation methods

The simulations discussed in Section 5.1 provided a particle and stellar distribution for emission and radiative transfer to be determined. To model the radiative transfer through the gas and dust, as well as the dust modelling, the Monte Carlo code MOCASSIN (MONte CARlo SimulationS of Ionized Nebulae) was used, as developed by Ercolano et al. (2003). The code uses a Monte Carlo iteration process to carry out the radiative transfer through the gas and dust of the simulation. Unfortunately, due to the inner workings of how MOCASSIN carries out the radiative transfer via this Monte Carlo iterative process (and also the monumental task it has to deal with), with high resolution and a greater number of frequency bins (discussed later in this section) it can be very computationally expensive. Even so, we are able to observe the simulated images in the same manner as what would be visible for an observer. MOCASSIN is also advantageous in its ability to simultaneously model both gas and dust within a simulation, and account for both in its calculations. This is heavily utilised in this project and is seen extensively later. For a full description of the code beyond what is discussed in this work, see Ercolano et al. (2003) and Ercolano et al. (2005). MOCASSIN was run on the High Performance Computers computing nodes at the University of Hertfordshire, using 8 processors with 16 GB of RAM per processor. We only had access to one node for every submission, as it was instructed that MOCASSIN could not run across multiple computer nodes, but instead only across processors within a single node. This mean that we were limited to, at most, 32 processors and 16 GB per node. The number of processors would not help with the memory issues presented due to the fact that the parallelization MOCASSIN performs would still mean that the entire grid is loaded into every processor, so having 8 processors or 16, would not make a difference to us. As a result, 8 processors at 16 GB per processor was chosen as a sufficient amount of memory per processor, and 8 processors being suitable to allow both more of our simulations to be processed, and also not take up too much memory as to inhibit other users.

First, we provided MOCASSIN with a grid that contains the locations of all the ionizing sources (massive stars greater than $20 M_{\odot}$) and the gas/dust particle layout from a given Dale et al. (2014)/ Dale (2017) simulation. With this, and knowing other specified parameters such as how many frequency bins are required (which decide how many possible different frequencies the energy packets can contain), MOCASSIN creates and releases energy packets from the stars, out into the surrounding region. The emission/luminosity from the star is modelled as isotropic (i.e. the star has uniform luminosity across its surface).

Energy packets are used in MOCASSIN instead of photons predominantly for computational efficiency. By combining a group of photons together and tracking that packet through the simulation, less memory and therefore time is required for the iterations as there are less items to track simultaneously. A specific feature of the energy packets is that they have a

	Run I	Run J	Run T	Run M	Run Q	Run P
Mass (M_{\odot})	10^4	10^4	10^4	10^4	10^4	10^4
Radius (pc)	10	5	2.5	2.5	5	2.5
(t_{ff} (Myrs))	2.56	0.9	0.4	0.4	1.2	0.4
α	0.7	0.7	1.9	1.5	2.3	2.3
v_{RMS} (kms^{-1})	1.4	1.8	6.9	6.1	2.6	3.6
n_{H} (cm^{-3})	136	1135	9096	9096	1137	9096

Table 1: Table of values for all simulations from Dale et al. (2014) and Dale (2017) and their corresponding parameters. These parameters were all predetermined prior to this work and are selected to give enough of a deviation from each other that distinct differences as direct results of these parameters could potential be seen.

fixed energy value; only the number of photons and the frequency distribution within the energy packets changes. Furthermore, the use of constant energy packets gives large assistance to the supporting of the conservation of energy as it can be immediately known that if an equal number of photon packets are instantly re-emitted after absorption, then energy conservation can be ensured due to the same energy in every packet. Thus, during the radiation transfer of photons, as an energy packet is absorbed, it will be instantly re-emitted and have the same energy.

5.3 Parameters and Initial Conditions

Multiple simulations with varying parameters and initial conditions were used with the incentive to find quantifiable differences in any observations found. The clouds chosen were those that had varying virial ratios (brought about through different radii - consequently leading to different densities, and RMS velocities) and freefall times. The naming system has been carried over from the work already referenced that these were taken from. In Table 1 I present all of the simulations used in this work and the corresponding parameters. Runs I, J, T and M are all initially bound clouds, and Runs Q and P are unbound, and this can also be seen through their virial ratios. I used Run I for much of the experimental aspects of the project, including the testing of dust and winds.

Few predictions can be made about how the evolution with time of each cloud will differ, as once multiple parameters are changed, the combined effect can be obscure. Given that Runs I and J are the same mass cloud but J has half the radius, it would be expected that collapse within the cloud happens sooner, and that star formation is more prominent due to this effect. Quicker collapse in a more dense environment and where the particle velocity is not significantly boosted has the predictable effect of establishing higher levels of stellar formation, given that the particles will be more bound as the escape velocity scales with $1/r^{0.5}$.

The variable parameters available in the Monte Carlo radiation transport calculations were limited only to the dust-gas mass ratio, dust distribution, grain size distribution, and then computational changes within MOCASSIN such as frequency bins. The grids containing the particles were predetermined, thus meaning that how the difference in mass between gas

and dust particles with regard to their ability to move and disperse, as well as the momentum transfer through both radiative and kinetic mechanisms could not be fully investigated. Essentially, the gas and the dust have to be treated as being coupled for this work. A final note to add is that Run P was only included for further investigation into spectral evolution of clouds and is absent in all other methods.

5.3.1 Dust model

As already mentioned, a dust grain-size distribution was included in the simulation, however this was implemented through MOCASSIN. A great deal of work has been done in attempting to estimate a dust-to-gas mass ratio for H II regions, however due to the unique nature of every H II region, as well as the technical difficulty of trying to make a measurement of a parameter such as this, an exact value cannot be easily stated. Work carried out by Anderson et al. (2012) and Brinchmann et al. (2013) illustrates just some of the large quantity of work that has gone into determining these parameters. Anderson et al. (2012) measured the temperature distribution of dust within H II regions and their specific features. Cold dust temperatures within the photodissociation regions were found to be 26 K, while temperature in local filaments were lower, at 19 K, and in dark clouds were even lower at 15 K. Brinchmann et al. (2013) used optical spectroscopy to determine the dust to gas mass ratio for H II regions. As a result, for this work we use the value they found of $M_{dust}/M_{gas} = 0.01$ as this also appears to be in reasonable agreement with most literature. As well as this, a dust size and type distribution is required, as this affects the probability of reprocessing in each cell and how the energy packets are reprocessed.

For the work carried out in all runs, a species distribution that was based upon amorphous carbon was chosen for the dust. Amorphous carbon has no crystalline structure to it and no order to the arrangement of the atoms. The term amorphous carbon covers a large spectrum of different types of carbon but usually refers solid state carbon such as soot, which, in a molecular cloud, dust may largely consist of or contain. Later, in Section 7.3, the effects of dust and the different possible distributions are investigated to see if the difference in species type can have a profound impact on the SED or is negligible.

Previously we discussed SPH codes, their workings and what their structure consists of. SPH codes are not based upon grids, as they are instead constructed by a series of particles, and since MOCASSIN requires grids as inputs it is necessary to map the simulations onto a grid. This was carried out through the use of a code given to me by Dr James Dale, and mapped all the particles onto a Cartesian grid and converted the cumulative values of particles (velocity, emission etc) within each grid into a single value for each such parameter. The resolution of the grid is the users choice, however it was found through early testing that the computers being used to carry out the computation was only capable of handling up to 128^3 cells. With these size grids the run times fluctuated, depending on the specific simulation being run, between 70-120 hours, with a few reaching the 150 hour limit put in place on the submission itself to the computers. This gave the earlier hindrance of not being able to work to the full potential accuracy of this method, as was originally intended. With regards to the outcome and results of this project, the shortfalls or more affected results will be around visualising the regions, as lower spatial scale objects could either not be resolved, or if so, not be large enough to be able to carry out work on them. Further to this,

some methods, such as determining the structure function of the region, will investigate the effects of noise, and although we do not know what would be an appropriate or minimum resolution, this work will help determine if at such scales they give acceptable results. This will be discussed further in Section 4.3. In spite of this, the cartesian grid should still provide a high-enough resolution grid for us to successfully gather all data and conclusions we hope to obtain. There are more accurate methods that have been developed and used in this same way such as Voronoi meshes (Hubber et al. 2016).

5.4 Output files from MOCASSIN

MOCASSIN returns multiple output files for the user. These include a plot file that contains intensities for every cell in every wavelength that is specified by the user. These were used to create the images seen later in Section 7. SED information for the whole region is also given, and this is dependent on the number of frequency bins set by the user. The maximum number of bins that was found for these simulations, that would also allow a cell number of 128^3 , was 300 bins. It was found that above this number of bins and grid cells, the memory required exceeded the memory available, and so this combination of bin number and cells gave a detailed-enough SED and also a resolution for the simulation images that was able to distinguish features such as pillars. Source locations, temperatures and masses, which are inputs for MOCASSIN, are recorded and are very useful in studying how H II regions form around individual stars.

5.5 Visualising output results

The intensity outputs from MOCASSIN were fed through a Python script that accounted for dust opacity; by taking the value of the intensity of a cell and multiplying by the exponential of the product of the opacity and frequency of that cell ($e^{\kappa\nu}$) in that wavelength. To make the visualisation possible, as previously discussed, a grid was created before being passed through MOCASSIN.

To construct BPT maps, a second Python script was provided by Dr Dale that read in gas densities and emission to produce maps in multiple line ratios. Structure functions, SEDs, peak ratio plots and ionizing source positions were all produced and implemented through Python scripts I, myself, wrote.

6 Emission lines

For the imaging of the simulations, four different lines were chosen- $H\alpha$ (656.3 nm), [O III] (500.7 nm), [N II] (654.8 nm) and [S II] (671.7 nm). The $H\alpha$ line comes from the electron transition from $n=3$ to $n=2$ in the Balmer series. [O III], [N II] and [S II] are all forbidden lines, as they violate the selection rules in quantum physics. As a minor overview, the selection rules govern the restrictions and conditions for electron transitions to occur in atoms and molecules. The rules state that for an electron transition to be 'allowed', the spin of the electron cannot change during the transition, both the total orbital angular momentum number (L) and the total angular momentum number (J) must change by exactly

± 1 , and the parity of the initial and final wavefunction must change. [O III], [N II] and [S II] all violate one of these rules through $\Delta L = 0$. Electrons become excited into meta-stable states in high energy levels, however due to the fact that the regions these atoms are existing are low density regions (H II regions and planetary nebula), atoms or ions are far less likely to experience collisions or other mechanisms that lead to energy transfer and remain unperturbed. Electrons in these meta-stable states are far more likely to also emit forbidden lines, and as a consequence of the excited electrons and prolonged periods of time for the electrons existing in these states, forbidden lines are emitted. Additionally, as a result of the low density and previously mentioned properties, the emission can contribute to a significant proportion of photons emitted, and occupy a large amount of the visible spectrum observed, with the ionised region being mostly transparent to visible light.

$H\alpha$ is a very good tracer of hydrogen ionization within these regions as it is one of the brightest hydrogen lines, making it easier for observers to trace. In H II regions, radiation from the massive stars is absorbed by neutral hydrogen, and the electron is given enough energy to become liberated from its host proton. It is then during the recombination of the electron with another proton that as it falls back to the ground state, a common transition conducted in this is the $n=3$ to $n=2$ transition - $H\alpha$. The potential of the transition coming from only an excited atom that has not recombined is very low due to the close similarities in the excitation energy from $n=1$ to $n=3$ and the ionization energy. Using the Rydberg formula given in Equation 17 where R_H is the Rydberg constant, an energy of ~ 12.1 eV is obtained, and for the full ionisation of the electron ($n_f = \infty$) the energy is found as ~ 13.6 eV. With these energies being close together, leading to a very small difference in the frequency of the photon required to liberate the electron or simply excite it to the $n=3$ state, it is far more likely that the atom is ionised and thus the $H\alpha$ comes from the recombination of the atom as opposed to a transition without ionization.

$$\Delta E = R_H \left(\frac{1}{n_f^2} - \frac{1}{n_i^2} \right) eV \quad (17)$$

The forbidden lines being observed are used as tracers for specific properties of the regions as well as for determining further aspects of the clouds. [O III] is a very good tracer of the hottest gas in the region, which is likely where the highest levels of ionisation may occur, and [S II] can be used to infer the electron density of the environment.

7 Results and Discussion

Through the early stages of working with MOCASSIN, a lot was found with regards to the level of accuracy we could achieve given the memory and timescale we had available. We started with a late simulation time step in Run I, and made low resolution grids (64^3). This gave an indication to the length of time required for the resolution of grid we would use, which for this size grid was around 2 hours for 20 iterations from MOCASSIN. Further to this, early SEDs obtained showed that at lower wavelengths (around the IR frequency band) the number of bins available were very low - being only around 5 for the entire IR band and the remaining 145 of the 150 for the visible and UV frequencies. It was therefore necessary to find a grid resolution that would be of high enough quality that structure functions,

reasonable quality images and higher resolution radiative transfer could all be produced. After testing, the number of frequency bins that could be used was 300 and a 128^3 grid. This was the limit that still allowed for all the results we hoped to obtain.

MOCASSIN also produces an output file for the direction-averaged SED, and this contains a range of wavelengths with corresponding luminosities. The number of wavelengths given is dependent on what is requested by the user and is biased towards higher wavelengths (the returned wavelengths are predominantly in the visible/UV). Given that our SEDs produced are in log space, and the linear spacing of the frequency bins, it lead to the larger frequencies that we wished to look at being less well sampled. During the work done in this report, multiple different viewing angles are chosen for taking the SED, and this was done through the use of MOCASSIN’s ‘*inclination*’ feature. The wavelengths were calculated from the frequencies and converted from Rydbergs to Hz and then μm . A position file for the ionising sources is also given, and all of these files are utilised in the following section.

In the simulations from Dale et al. (2014) some included winds while others only allowed for photoionisations from massive stars. The purpose of using varying levels of realism allows for the individual investigation of specific mechanisms that exist within these systems, and in what way they alter the environment. It is only for Run I where we investigated the absence and presence of winds side by side, and for each we study the emission maps and the corresponding SEDs.

The addition of winds is then included into the photoionisation simulation via the modification of the SPH code. Winds alone are not investigated in this project as it is widely agreed that winds have substantially less effect than photoionisation, and this has been shown by Dale et al. (2014) for these specific simulations. The winds are implemented through imagining that the massive ionising sources emit momentum particles randomly in all directions. Which gas particles are struck by the momentum particles is determined and then as they come into contact with gas particles, they transfer small amounts of momentum to them, and thus lead to wind-like effects.

7.1 Images

The images given in the following sections are from MOCASSIN, and are emission maps in $H\alpha$ normalised to the maximum peak in the map. In addition to this, the intensity scale of the images is logarithmic. Consequently, despite images potentially appearing to look as bright in different emission lines, this is in fact not the case, and it would actually be the case that emission from, potentially, [S II] would indeed be fainter than the emission from $H\alpha$. Furthermore, since the simulations are three dimensional, the images are constructed through projecting them down one line of sight to give a two-dimensional image, representative of what an observer would see - the emission in the image is the overall emission down every pixel line-of-sight.

7.1.1 Photoionisation only

The evolution of the H II region with time is in line with that which has been implied by observation, where it is possible to image multiple clouds, determine their approximate ages and thus see how certain features evolve with time. In the early images, we see outflows

expanding into the cold gas, driven by the photoionizing radiation from the massive stars. The heated gas escapes through the weak points in the cloud and leads to bubbles further from the centre of the ionising source, where the gas is ionised and less dense. Since massive stars are continually forming, in different locations multiple bubbles can be driven at the same time from these locations. It can also be noted how the bubbles evolve through the four different morphological types that were discussed previously. This indicates that, in this circumstance, the shape of the bubbles is indicative of the age of the region, and can be traced in Figure 6.

Within the later stages of the evolution there are prominent features that can be seen. One of these features is clear and well-defined pillar structures. These are present in the left lobe, and following the progression of this specific region of gas and this main pillar present is the remains of an accretion flow, although pillars can form in many ways. Pillars from accretion form through the destruction of the flow close to the star from stellar winds. The winds are strong enough to disrupt the flows and disperse matter close enough to fall onto the star. Pillars can also form through high density cold gas present within the cloud, and as photoionisation leads to hot gas and consequently an H II region, the hot gas looks to leak out through weak points in the ionisation front. Higher density regions survive longer (this was already discussed in Section 2.1) and they can often result in these pillar shapes, where these isolated dense objects become overrun by the ionisation fronts.

Delving into where the ionising stars form, the extent of the effect of photoionisation on the surrounding regions can be seen, as this can indicate to what level the feedback from the stars was able to form new star-forming regions; changing the density of the gas enough to trigger star formation. The ionising sources are close to the centre of the cloud, but the bubble is clearly expanding out to large radii, indicating the high ionising capabilities of the sources. There are in fact seven sources, however due to the closeness of some of the sources in this plane, it is not possible to fully see them. I give an image of the sources overlaid onto the final time-step image in Figure 7.

Some of the most interesting features are also what we do not see, being that there is no evidence of massive star formation outside of the original stellar nursery. However this does not mean that no triggered star formation occurs, and the simulations do exhibit this, but the emission maps only show no sign of massive stars within this triggered formation. The simulations also signify regions where star formation is terminated by the photoionisation. This is difficult to see in the emission maps, but termination often occurs close to the massive stars as it is here where photoionisation and winds are strong enough to destroy forming stars.

Something that can also be seen with the sources overlaid that is not immediately clear as to the reason behind the behaviour is the fact that the sources do not sit in the centre of the bubbles, but at the very edges of the two bubbles instead. In an ideal model, an ionizing bubble would expand approximately evenly around a forming star, such that the star sits seemingly in the middle. But for a star to be at the very edge would seem rather counter-intuitive. The explanation behind this comes from mechanics previously discussed in Section 2.1 when it was stated that hot ionised gas escapes through the path of least resistance, where less dense points on the ionisation front impose less pressure on the hot gas and thus give way to hot outflows. In this case, for the massive stars there was most probably less resistance on the hot gas to the left and right, meaning that these two H II bubbles formed to the sides of them as opposed to symmetrically around them. The wealth

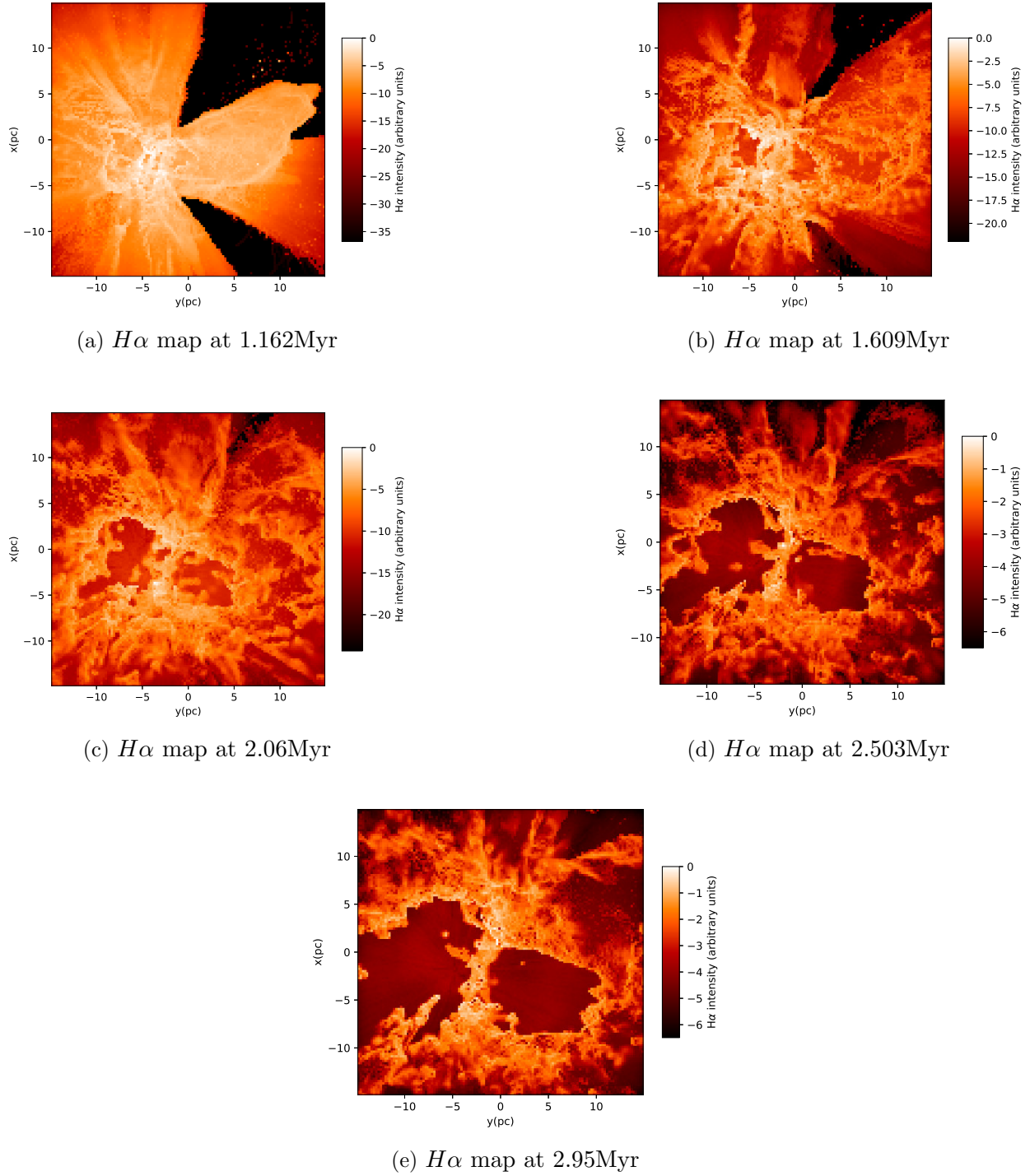


Figure 6: Evolution of $H\alpha$ within the simulated GMC of Run I with photoionisation only. The dark regions correspond to very low/no $H\alpha$ emission, and bright areas signify a high level of emission. At later times well-defined bubbles can be seen forming in the centre and outwards to the left and right, caused by the photoionising radiation from the massive stars. Distinct pillar structures can be seen at the bottom left of the final two panels, caused by the destruction of the surrounding environment, with these likely surviving due to being high density regions.

of research carried out on H II regions by numerous authors, and the images and simulations gathered around them have shown that under accurate galactic conditions the majority of massive stars that form H II regions do not sit precisely in the centre of such bubbles, and can thus be deceiving when attempting to identify the ionising source responsible, and remains a challenging task.

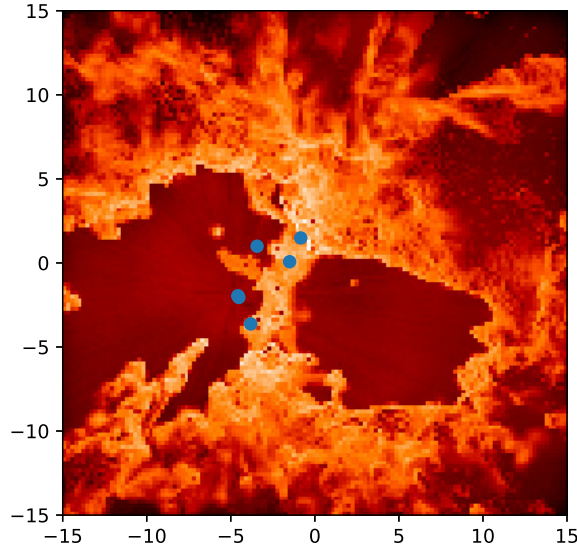


Figure 7: Positions of ionising sources in the photoionisation only simulation at 2.95 Myr. The scaling is the same as previous images shown of this simulation. It is evident that the later-forming stars have all formed within the central, more dense region of the cloud and that the H II region expansion has not lead to triggered star formation further out beyond the ionization front.

7.1.2 Photoionisation and winds

We now look at Run I with both photoionisation and winds turned on, and compare it with the discussed model above. In the early stages of the H II region, there are no distinct differences between it and the simulations with photoionization only. However it can be noted that distinct bubble-like structures form earlier than with the absence of winds, although this may be a characteristic that is specific to this simulation. A further consequence of this earlier bubble formation is the dominance of these early bubbles. The bubbles grow more rapidly and dominate over bubbles that form later, illustrating that the combined effect of photoionisation and winds is more effective in clearing gas away from the massive stars.

A second observation that can be made from Figure 8 is the lack of pillar-like structures in comparison to when winds were absent. Where previously there were prominent pillars in the bottom left, these are now stumped in shape and fragmented. The effects of winds on these pillars could be correlated with how these pillars formed. Winds can disrupt and destroy accretion flows onto stars, which may have been the case for these pillars. Studying the source positions once winds have been included allows for a more detailed look at how winds hinder or assist star formation compared to when only photoionisation is present.

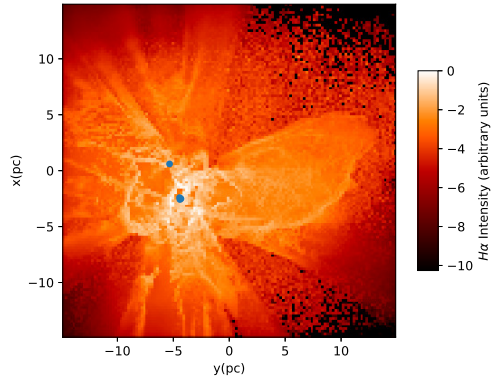
Looking at Figure 8e, a notable difference in the distribution of the massive stars is seen, and the stars are more towards (but not in) the centre of the H II regions. Supporting the potential possibility that the pillars were destroyed by winds, and/or were accretion flows is the presence of a massive star within the vicinity of the pillars. The star sits at the tip of a large pillar and has a second pillar curving around it. Studying the region at an earlier time in Figure 8d we can see that the pillar the star is found at the tip of did not exist, and is a probably consequence of hot gas around the star escaping through weaker points in the ionisation front. It is therefore likely the case that the massive star formed there out of chance at the base of a pillar and destroyed it. The second pillar structure, that sits to the right of the star, is also experiencing the driving effects of the newly formed star and is therefore likely being destroyed by its winds. With this star also forming in a different region to the initial stars, far from the centre where the first three were situated, it is reasonable to suggest that winds assist in collecting gas without transferring large amounts of kinetic and/or thermal energy into dense clumps suitable for star formation.

7.1.3 Photoionisation, winds and dust

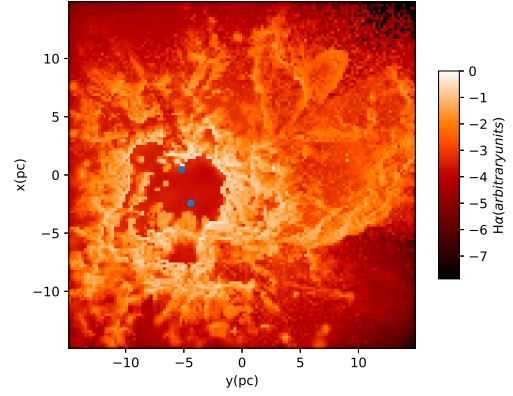
The SPH simulations used in this work do not include dust and I am only able to study the emission properties of the dust through MOCASSIN. The only notable differences will have been in the emission peaks, which can be seen in Section 7.2. The dust model that we used was able to sufficiently demonstrate the effects seen through observation of dust, however it was not possible to model any varying dust models with time or how the mass ratio of dust:gas may have varied as the cloud evolved.

7.2 Spectral Energy Distribution

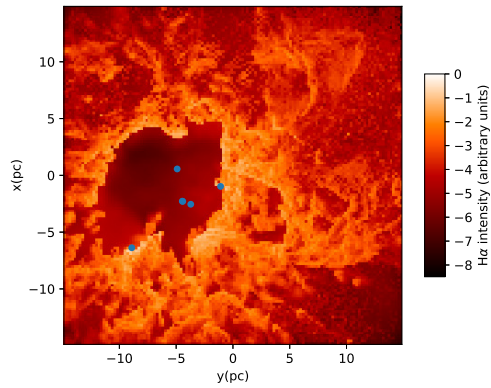
The spectral energy distribution (SED) of any celestial region can reveal an abundance of information to an observer, with indicators to star formation, temperature, age, and many other properties. With molecular clouds and H II regions, there is a potential wealth of knowledge to be gained from them, given that they highlight so many mechanisms that occur within the clouds (discussed in more depth later in the section). Regarding the SEDs of molecular clouds and more importantly H II regions, there has been some work done in identifying how features in the SED can reflect potentially the shape or age of the region. Relaño et al. (2013) took an extensive survey of H II regions within M33, and through a devised morphological classification system that took into consideration the evolutionary status of the bubbles present, gave normalised and averaged SEDs that were representative of each H II region morphology they found. They classified H II regions into four different classes - filled, mixed, shell and clear shell. However, this classification relied on only the physical appearance of an H II region, and thus determine its class which then assigned its SED shape to a specific class. It may be that different classifications of H II region can be represented by more definitive features, therefore by examining the evolution of the SED in a simulation with time, and then investigating how these features change with cloud properties it may be possible to give more accurate classification of these regions.



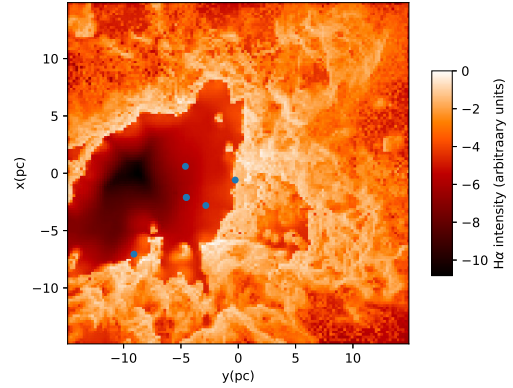
(a) $H\alpha$ map at 1.162 Myr



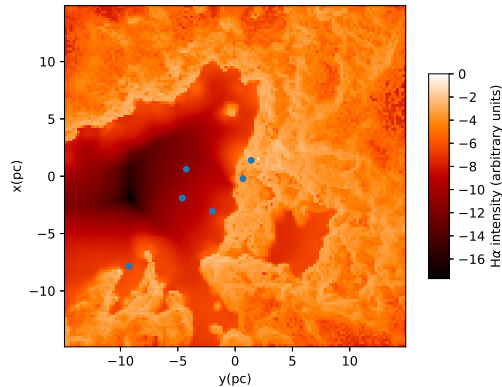
(b) $H\alpha$ map at 1.609 Myr



(c) $H\alpha$ map at 2.06 Myr



(d) $H\alpha$ map at 2.503 Myr



(e) $H\alpha$ map at 2.95 Myr

Figure 8: Evolution of $H\alpha$ within GMC with the effects of photoionisation and winds for Run I. Dark regions also correspond to low/no $H\alpha$ emission and bright regions indicate high $H\alpha$ emission. The blue dots give the locations of the massive stars, and the occurrence of them being spread out across the region indicates later intervals of triggered star formation. A very large bubble, greater than that seen in Figure 6 likely due to the increased combined effects of photoionisation and stellar winds exists and dominates the region. Pillars still exist in the bottom left but are not as well defined due to the added destructive effects of winds- which can terminate accretion flows that are one cause of the occurrence of pillars.

7.2.1 Photoionisation only

With photoionisation effects only, and with no dust in the simulation, we would not expect to see any emission tracers of dust in the SED. The main effect of dust in H II regions is the absorption of high frequency photons (UV) from the stars and the re-emission of these photons at lower frequencies (IR). Without dust, the stellar spectra of the stars leaves the cloud largely unchanged. The stellar spectra are close to being black bodies and the only absorption present within them are from photons that have high enough energy to be able to ionising hydrogen within the cloud. These tracers would be in the form of peaks in the IR area of the SED. The emission seen is therefore that of the emission from the ionising sources and should follow a blackbody-shaped curve.

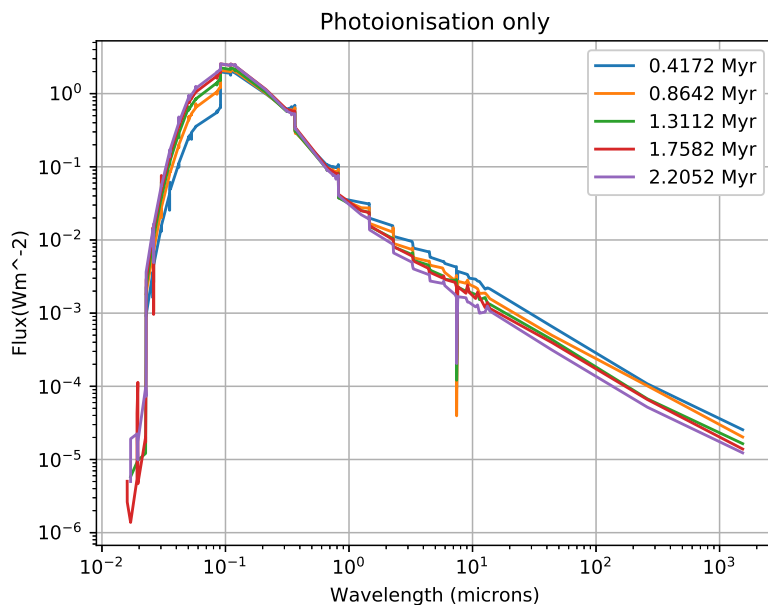


Figure 9: Spectral energy distribution for the photoionisation only GMC from Run I averaged over the whole image along the same axis as the illustrated images (which has been defined for our own use as the z-axis). The decay of the plot at the IR tail is indicative of the SED being largely dominated by the stellar emission of the massive stars and that this radiation undergoes little/no reprocessing.

7.2.2 Photoionisation and winds only

The main effect of stellar winds is to drive gas away from the massive ionising stars, leading to the H II region's spectrum becoming less effected and altered until a new massive star forms that is embedded. As winds drive turbulent flows, and also collect up gas into denser and colder regions, star formation can continue at increased rates as these regions of high densities and low temperature pose ideal environments for new stars to form since it can lower their local Jeans Mass.

The behaviour of the SED is in line with a difference in star formation between the two regions. It appears plausible that in the simulations involving winds, the star formation

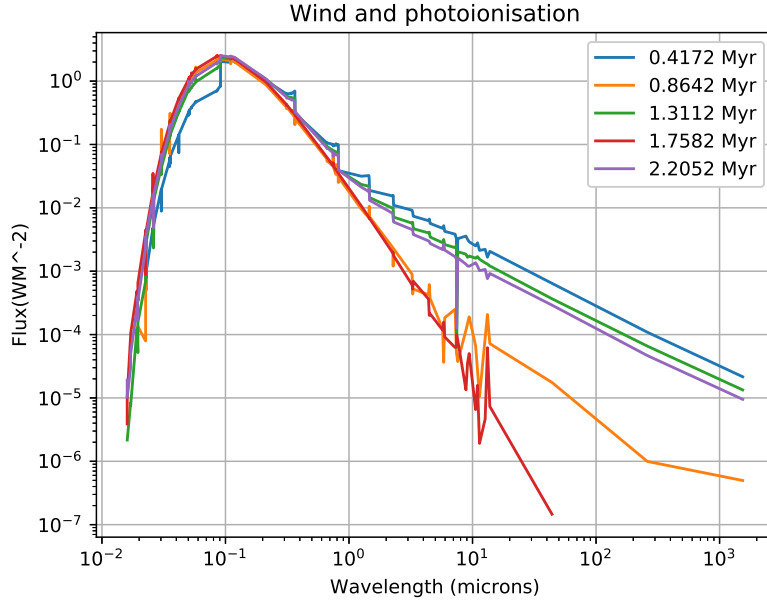


Figure 10: Spectral energy distribution from Run I for photoionisation and winds. The plot differs from photoionisation only with some time steps having considerably lower IR than the photoionisation only, and although this could be a consequence of the winds, it is believed to be a computational error with the simulation dumps- likely being the result of cells that have failed to converge and thus the temperatures of the gas being wrong.

is delayed, despite still forming the same amount of massive stars after the last time step. By studying Figure 11, it can be seen how for no winds present, there is a reasonably linear increase in the number of stars that form with time. In contrast to that, with winds introduced the number of massive stars increases in large jumps between certain time-steps. Due to the fact that we cannot process all dumps from a simulation because of a lack of time, it is not possible to determine at which point the stars formed to greater detail than identifying in between which dumps they formed. The large jump in ionising sources may be indicative of a secondary region of star formation. Consequently, this may lead to the reason for the later jump in the SED at older ages.

7.2.3 Photoionisation, winds and dust

Adding dust into MOCASSIN has a large effect on the SED we obtain. This is due to the reprocessing of higher energy photons and subsequent re-emission of IR photons, as discussed in earlier sections. The peak of the IR is maintained likely due to the continued occurrence of newly forming massive stars that are embedded within the gas and dust.

7.3 Effects of dust grain-size distribution

When introducing dust into the simulations, a suitable grain-size distribution had to be chosen that would represent what would be present within a molecular cloud in reality. This

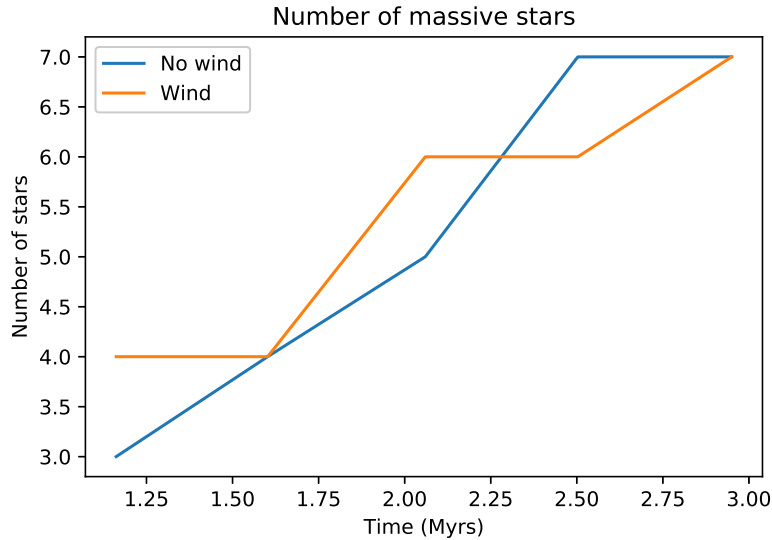


Figure 11: Evolution of the number of sources with time, with both wind present in the simulations and absent. It can be seen how with winds included, star formation continues at a slightly better rate, with star formation terminating around 2.5 Myrs, but continuing after this time for winds. Winds also seem to cause the star formation to be more incremental and staggered as opposed to photoionisation only, likely caused by the winds to better create ideal regions for triggered star formation.

is a very hard task due to the fundamental problem of not truly knowing what the dust properties are of a given molecular cloud to great extent, something that is still the centre of a great deal of debate. Although we have an informed understanding of what gas and dust particles consist of, and also a general idea of what is contained in a molecular cloud, we cannot look directly at a cloud and through any type of observation determine the size distribution exactly. It can, however, be indirectly inferred and constrained through methods such as studying the slope of the far infrared within the GMC’s SED. This therefore leaves the task of having to make a decision of the dust grain sizes that would best represent that of a molecular cloud.

As previously mentioned in Section 5, a dust-to-gas mass ratio of 0.01 was chosen, as this is a largely accepted value within molecular clouds. Further to this, the species type selected for the work carried out was based upon the physical parameters of amorphous carbon - a group of carbon compounds that contain no crystalline structure. In addition to the aforementioned species distribution, five other distributions were chosen to investigate. The first was a glassy pyroxene distribution (glpyrMg50), composed of largely magnesium, iron and silicon oxide particles. These types of compounds (found in pyroxene) are most likely to be formed in very high temperature and pressure environments, likely a by-product of a dying star and/or supernovae. The second distribution is a silicate-type distribution (glSil). Due to silicon being a larger atom, but with the same grouping in the periodic table of elements as carbon allowing it to form multiple bonds, the dust particle sizes are found to mainly exist in the range ($\sim 0.1 - 1\mu m$), but with some grains exceeding larger diameters of $20\mu m$ (Speck et al. 2009). In the following table I give the minimum, maximum and

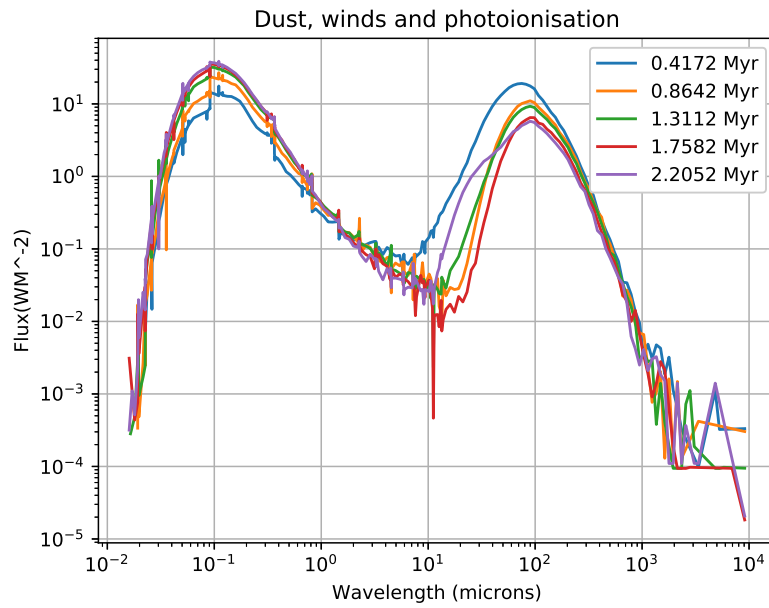


Figure 12: The spectral energy distribution for photoionisation, winds and dust inclusion from Run I as an evolution with time. There are clear differences compared to Figures 9 and 10 which is the result of the dust properties present. The dust is able to absorb higher energy photons and then re-emit them in the IR, leading to the observed IR peak. Two of the IR peaks are shifted slightly more towards shorter wavelengths which is likely the result of the presence of hotter gas near newly formed stars.

Name	$a_{min}(\mu m)$	$a_{max}(\mu m)$	Index
amC-hann	0.04	905	2.2
glSil	0.4	500	3.6
glpyrMg50	0.2	500	3.6
Sil-dlaor	0.01	10^4	3.3
OssOdef	0.4	10^4	3.6
OssOrich	0.4	10^4	3.6

Table 2: This table gives the minimum and maximum values of the dust grain radii as well as the power law index for every distribution used in this work.

power-law index for all of the dust distributions.

The following two distributions are linked to the silicate distribution and study oxygen deficiency and richness within the dust. An oxygen deficient silicate species (OssOdef) that is representative to that which may be present within a circumstellar disc, along with an oxygen rich distribution (OssOrich) of the same type are trialed as this may be a plausible composition of the dust during the star formation in the molecular cloud. The final distribution is another silicate distribution from Laor & Draine (1993) (sil-dlaor).

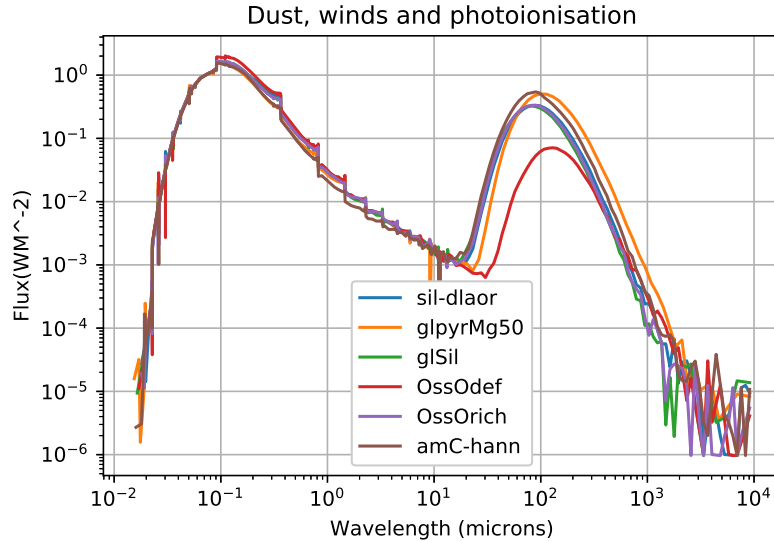


Figure 13: Spectral energy distributions for different dust distributions with the 0.8642 Myr dump. It is evident that most of the distributions are in close agreement with the distribution we have chosen, and only OssOrich, which is a dust distribution found mainly within the protostellar discs of forming stars, has any significant deviation which does not impact the applicability or validity of our results since this would only account for a very small percentage of the total dust in the GMC.

Figure 13 illustrates that for almost all of the dust distributions there is very small difference in the resultant SED. Looking towards lower wavelengths, the stellar emission from the stars can be seen and predictably, there was negligible difference between the distributions.

The reason for this is because the emission in this part of the SED is representative of unprocessed radiation from the massive stars. As such, the wavelength range does not discriminate between the models, and it may be the case that for the oxygen-deficient distribution that there is a greater presence of grains in the size range of $0.3 - 0.5 \mu\text{m}$ where this is found to lead to a local maximum extinction and absorption, found by Clayton et al. (2003).

Larger effects are found in the higher wavelengths, representative of the IR radiation and the reprocessing of stellar radiation through the dust. The most notable differences lie with the lack of IR emission from the oxygen deficient distribution. This distribution is a distribution that could be found within a circumstellar disc, where it may be found that a large proportion of reprocessing takes place. However, oxygen rich silicate distributions can be found around forming stars and they exhibit a far greater IR emission. This highlights a potential inconsistency in the measuring of spectral energy distributions with the lack of knowledge around the dust distribution present. The experiment shows that the difference in grain-size distribution has little effect on the measured emission from the cloud, unless an oxygen depleted distribution is used that would be suitable more towards a circumstellar disc as opposed to the bulk of a molecular cloud. The second note to draw from the results is that the distribution that was chosen for the work done is moderately representative, given that it matches the effects other distributions have on the emission. The resultant impact on the conclusions drawn is that the results are, for the most part, in accordance with many possible dust distributions.

7.4 Evolution of SED with time

As the massive stars continually expand the H II regions around them and clear the gas and dust from close proximity, there is more opportunity for photons from the stars to escape the environment without being reprocessed or scattered by the dust (and partially by the gas). How embedded a star is in the molecular cloud leads to noticeable signs within the SED. Referring back to Figure 12 it can be observed how at the early stages of the cloud, where stars are still deeply embedded in the cloud, there is a noticeably higher infrared peak than optical/UV peak. This indicates not that the stars are not formed and/or are emitting, but instead that a higher proportion of the emission from the stars is being reprocessed by the dust and re-emitted as IR. However it may be predicted that as the stars clear their surroundings then the IR peak would drop. This would be true if no further star formation was allowed, but all five simulations discussed here do and consequently as cold gas and dust become denser and collapse, more stars form. These new stars are also deeply embedded within smaller clumps and thus their radiation is reprocessed by the dust. The resultant effect is a maintained IR peak until no further star formation can occur. In the simulations we do, however, see these effects as a result of massive star formation only and not as a combined effect of massive and lower mass stars since we have not modelled the lower mass stars here.

Given this, and the fact that we are able to measure the peaks in each spectral band, it may be possible to use this as a method to age, or at least systematically classify H II regions and molecular clouds by their measurable features as opposed to making conclusions by eye. Figure 14 shows how the ratio of the peaks evolves with time for each of the runs. In order to maintain continuity across all simulations, a set of boundaries were implemented

to define the range of frequencies that can be used for each of the peaks. For the infrared section of the SED the frequency range $4 \times 10^{11} < \nu < 2 \times 10^{13} \text{ Hz}$ and for the UV portion the boundaries $10^{14} < \nu < 10^{16} \text{ Hz}$ were adopted. The purpose of these boundaries is also to accommodate for an issue found with MOCASSIN where for the lowest frequencies the flux values were found to be missing, leading to these regions of the SED remaining undefined. Additionally, as will come more apparent in Section 7.4.1, the SEDs used for these calculations are taken down a single line of sight, and are not the net total of the emission in all directions or directionally averaged. MOCASSIN also outputs directionally averaged SEDs, however these are not useful in studying orientation effects.

This method takes the integral of the emitted flux over the previously mentioned frequency ranges, given in Equations 18 and Equation 19

$$A_{IR} = \int_{4 \times 10^{11}}^{2 \times 10^{13}} F(\nu) d\nu \quad (18)$$

$$A_{UV} = \int_{10^{14}}^{10^{16}} F(\nu) d\nu \quad (19)$$

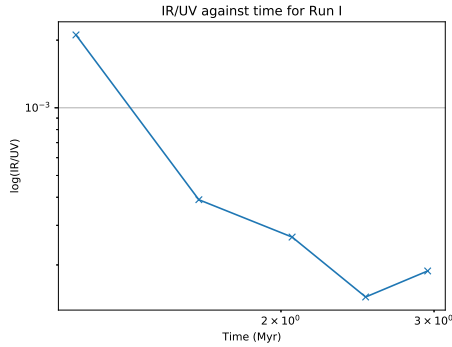
Since it is not possible to solve these integrals analytically for our SEDs, we result to using numerical methods and a summation approximation, demonstrated in Equation 20.

$$\sum_{i=0}^{i=n} F(\nu_i)(\nu_{i+1} - \nu_i) \quad (20)$$

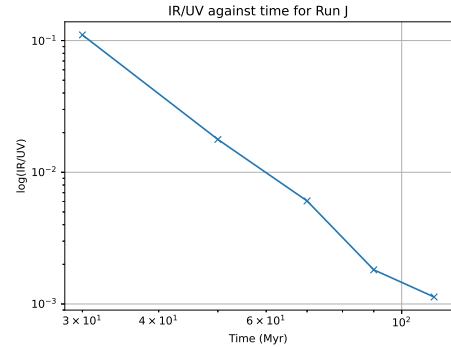
This then gives us the area for each region, and following a simple division of the two is taken which allows us to arrive at the desired ratio.

Across Runs I, J, T and M there is a very similar behaviour in the form of a power-law decay of the infrared against ultraviolet. The nature of the decay is in line with the occurrence of embedded stars continually clearing their surroundings, reducing the level of dust that is processing the stellar radiation, and highlights the potential case that in spite of new embedded stars forming, they do not have enough of an effect to increase the ratio by a significant amount, if any at all. It is possible that the ability for unprocessed radiation to escape the region increases at a greater rate to that of the amount of radiation being reprocessed by dust from newly formed stars. To understand better the behaviour of these plots, it is useful to study the star formation and number of stars present over the same time period. It is again important to highlight that these simulations do not model sources of intermediate or low mass; only the high mass stars have the ability to affect the environment around them.

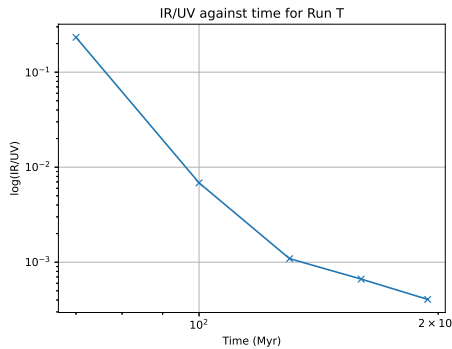
Figure 15 depicts an interesting story regarding the star formation and number of ionizing sources present in the simulations. Runs J, T and M all exhibit very similar increases in massive stars; sharp initial increases as the gas fails to quickly clear due to being bound (seen by their lower virial ratios), as well as having higher initial densities that maintain more suitable star forming environments for longer. In contrast, Runs I and Q possess substantially lower increases in massive stars, showing very slow and linear increases with time.



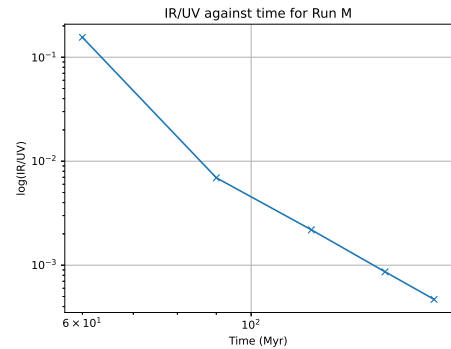
(a) Evolution of IR/UV peak for Run I



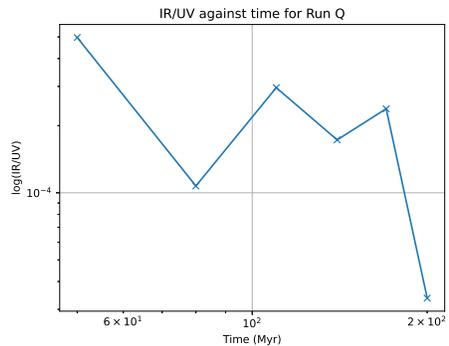
(b) Evolution of IR/UV peak for Run J



(c) Evolution of IR/UV peak for Run T



(d) Evolution of IR/UV peak for Run M



(e) Evolution of IR/UV peak for Run Q

Figure 14: IR/UV peak for each simulation as a function of time. It is seen how there is a consistent pattern of decay within Runs I, J, T and M, and that Run Q has a more chaotic behaviour which could be linked to it being an unbound GMC. Given these plots, it posed an important question of whether the nature of these plots was due to a decrease in IR emission, and increase in UV, or a combination of both.

When assessing and attempting to understand why this pattern exists for the peak ratios, there are only a few mechanisms that may contribute, however the most likely is with regard to the current physical state of the cloud. As the initial massive stars continually ionise hydrogen, and the photoionisation and stellar winds clear the gas and dust, this overall lowers the amount of both gas and dust that the radiation has to pass through. With regards to the earliest forming massive stars, they simply experience a smaller layer of gas and dust around them and reduces the probability of reprocessing. For the newer, embedded stars that are still undergoing accretion and have not yet cleared their surroundings, the same circumstances are at work. The regions beyond the immediate accretion area have been cleared, and as such we see again that the reprocessing probability goes down. Even more so, it may be the case that the effect that this cloud destruction has on the decrease of IR emission is beyond that of the increased rate of dust reprocessing that comes with the embedded newly-forming stars.

The implications of the processes that stand behind the found relation is that this can act as a tracer for the level of destruction that has been caused over the entire life-time of the H II region, which would be defined as the point at which the first massive stars formed. The lower the IR/UV, the more substantial the gas-clearing and the greater the volume of H II.

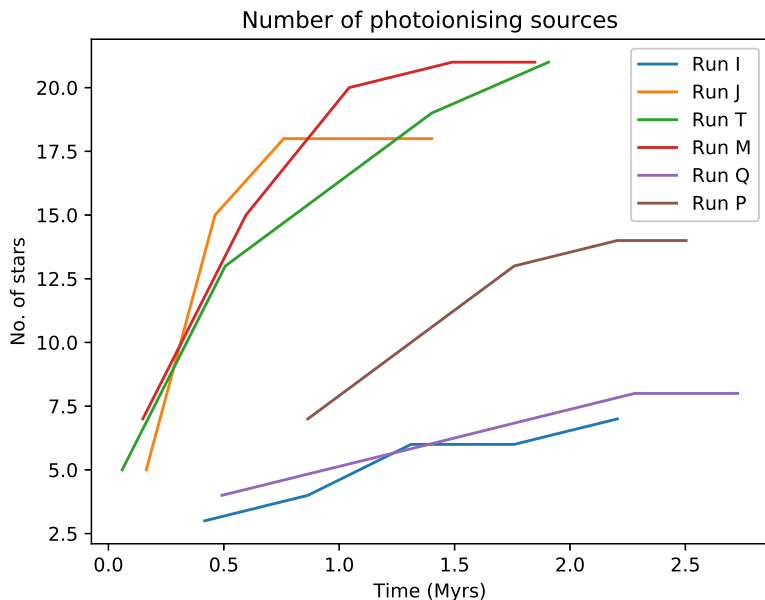


Figure 15: Evolution of the number of photoionising sources with time for each simulation run. The runs all start at different times due to not taking measurements from the very start of each simulation, but from the point where massive star formation is fully underway.

A comparison of the change in area ratios with time presents a systematic change in the nature of the decay. Figure 16 illustrates both the difference in IR emission in comparison to UV for all runs as well as a new run, Run P, from the time where ionisation first turns on, as this gives a more meaningful insight to how significant the differences between the cloud

properties are. Run P had the same virial ratio and mass as Run Q, but had half the radius which makes for a cloud that has a much higher escape velocity. This would help bridge the difference more between bound clouds and unbound clouds as its properties make the resultant levels of star formation and destruction more unpredictable and gives us further information specifically to unbound GMCs, considering up until now the only unbound cloud has been Run Q. Due to the lack of data points for the simulations, it is harder to draw an accurate relation, however it is apparent that, again with the exception of Run Q that seems to behave differently to the other runs, there is the consistent occurrence of a power-law. Runs J, T and M demonstrate very closely matching power-laws, exhibiting powers laws of $\propto t^{-2.169}$, $\propto t^{-2.266}$ and $\propto t^{-1.867}$. As the conditions of the cloud allow for more destructive behaviours to occur, such as a higher virial ratio and (given the circumstances) a differing radii, we start to see a stray away from this relation, with a power law of $\propto t^{-1.543}$ for Run I and an undefined relation for Run Q. Initially, this seems counter-intuitive as it would be predictable that clouds with more embedded stars and remain embedded due to the high gravitational energy relative to the kinetic energy would find the amount of IR emission is much higher for longer periods of time, and not drop off as quickly. However, judging from the nature of the plot at early times it is visible that there is still a steep drop off, but due to the cloud exhibiting a lower gas density in spite of having the same virial ratio the cloud's stars free themselves from being embedded quicker and also hinders the level of further massive star formation. A further observation of all runs is their eventual decay, being that by extrapolating data at longer timescales it appears likely that they tend towards the same/similar value. It is probable that this value would be the value of stars with no dust reprocessing around them.

Referring back to Figure 15, there is a distinct similarity between how the peak ratios evolve and the evolution of the number of stars. Runs I and Q experience a much slower rate of star formation, as previously mentioned, and this correlates into how their peak ratio evolves - specifically that lower star formation tends towards a flatter curve for the ratio. This would appear, upon further reflection, to give explanation in multiple ways to why the different pattern of behaviour is seen. First and foremost, with fewer massive stars capable of ionizing the gas present at any given time, and with the failure of the cloud to support sufficient star formation, there are not the quantity of embedded stars that contribute to the great amounts of IR radiation we see in Runs J, T and M. Second to this, and equally important to the contribution of the relation is the rapid ability for the cloud to be dispersed and ionization to take effect. The stellar winds and ionization can lead to significant levels of bubbles and clearing at very early ages that is not dissimilar to what can be seen at the late stages of clouds with smaller radii, lower virial ratios or other parameters that make them more gravitationally bound.

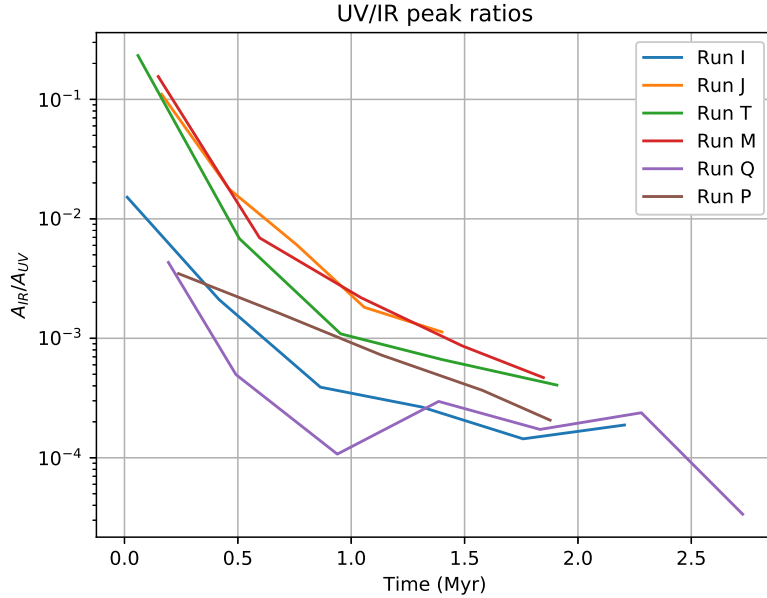


Figure 16: Direct comparison of how the value of the area ratio changes with time across all runs. Ignoring Run Q we see how all other simulation runs follow a gradual power-law decay with time. What is also apparent is that the steepness and vertical position on the plot are seemingly tied to how bound the clouds are (virial ratio).

To understand in greater depth which mechanisms are playing dominant roles in the nature of the behaviour in Figure 16, separate plots of the UV and IR emission, normalized to their individual peaks, were constructed. The area of the individual peaks in each time step is found and the value plotted. The results are shown in Figure 17.

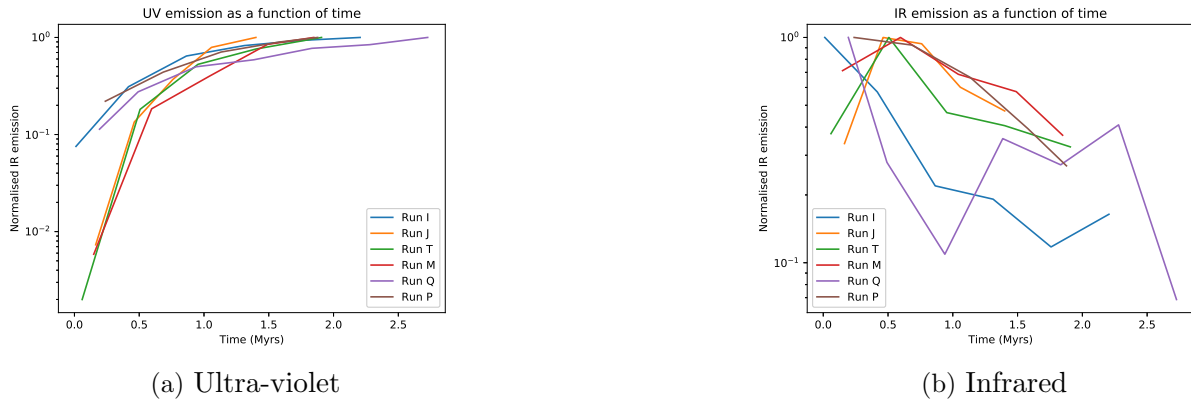


Figure 17: The UV and IR emission curve areas as a function of time. The plots have been normalised to their peaks. These two plots show that the behaviour of the IR emission of the GMCs is the dominant factor in the observed behaviour of the IR/UV plot. The continual decay after only a short period of time agrees with the fact that the clouds become more dispersed and ‘cleared out’ as the stars continually ionise and destroy the cold surround gas, which allows for more unprocessed radiation to escape.

The evolution of the plots in Figure 17 indicates that the IR plays the more influential role in the results given in Figure 16. The UV plateaus towards a maximum value that is representative of the stellar emission in the lack of presence of nearby dust and the continuous clearing of embedded stars until they have all fully cleared their surroundings. The IR behaviour comes almost completely from the presence of embedded stars in the cloud. Referencing back to Figure 11 where the evolution of massive star formation can be seen, clouds that experience high levels of massive star formation early on emit increasingly higher levels of IR before decreasingly with time, whereas clouds with low levels of massive star formation have initially decreasing functions. Given that after a specific time for Runs J, M, T and P massive star formation appears to cease or is greatly slowed due to how much gas has been cleared, it makes sense that the IR can ‘freely’ decrease as the remain stars free themselves from the surrounding gas and dust. Run Q exhibits particularly chaotic evolution with time despite its similar star formation profile to Run I. This suggests that in addition to the embedded stars having large influence on the result, the measure of how bound the cloud is also plays a role that is significant enough to dictate the measure.

7.4.1 Protostellar Luminosity Function

As already mentioned, the SED contains no information regarding the lower mass stars that are also forming in these regions due to the lack of ionising capability found in these stars. However these stars would contribute to the spectral energy distribution, and maybe more so in the visible/IR spectrum than in the UV. Offner & McKee (2011) give the accretion luminosity of a protostar, given in Equation 21, as the combined luminosity of all protostars in the region could lead to a change in the total detected IR/visible flux in the cloud. Further to this, at different times the luminosity within a band of wavelengths may differ depending on what the dominant source is (e.g. whether low mass stars or dust reprocessing are dominant in the visible/IR). It would be expected that at very early times the dominant source of lower frequency radiation would come from the forming massive stars and the heavy reprocessing of radiation through the dust due to the still deeply embedded stars. At later times, when the stars have cleared their surroundings, there would still be lower mass young stellar objects (YSOs) that are still emitting predominantly in the IR.

$$L_{acc} = f_{acc} \left(\frac{m}{0.25M_{\odot}} \right) \left(\frac{\dot{m}}{2.5 \times 10^{-6} M_{\odot} yr^{-1}} \right) \left(\frac{2.5R_{\odot}}{r} \right) L_{\odot} \quad (21)$$

In Equation 21, m is the mass of the star, f_{acc} is the fraction of the gravitational energy of the infalling material that is radiated away, and r is the radius of the star. We can then use this equation to account for all the luminosity that we are not modelling in the absence of the lower mass stars. It is important to stress that using this equation only gives us a rough estimate for what the contribution of accretion luminosity would be if we had the ability to model it more accurately. Within this equation we have also had to give our own estimates for getting all the of the masses for the stars, the accretion rates, as well as assuming there is a power-law between there mass and radii.

There are, however, certain obstacles in this method of including these accretion luminosities. Firstly, the luminosity determined would be the sum total of the flux over 4π

steradians, however the SED obtained would be from only one direction. The second short-fall, although not detrimental to being able to apply these luminosities to the SED, is the lack of wavelength information for the emission. There is no information regarding the peak of the emission frequency or any kind of distribution for the frequencies, and as such we make the assumption that the luminosity exists only in the frequencies satisfying the frequency boundaries of the IR/visible area of the SED. This over-assumption (since it is certainly not the case that the entire luminosity of the low-mass stars exists strictly in only our set of boundaries), we can see if they would make up a high-enough percent of the luminosity such that it could have a significant effect on the results we found studying only the massive stars. Investigating in the most extreme of cases will help determine whether it is necessary to take closer and more careful consideration into the influence of low-mass stars

Figure 18 plots the cumulative luminosity of all the massive stars, and then the estimated total IR luminosity due to accretion onto all low mass stars using Equation 21, and the masses and accretions estimated by the SPH simulations. The value for the fraction of gravitational energy that the stars radiate away is given an approximate value due to the difficulty in trying to measure this value, and also for the fact that it will be different for every star, but in this work we have to assume many of the properties about these stars. We see that the luminosity from the low-mass accretion is significantly less than the massive star luminosity, and the ratio of the two rarely comes close to 1%. This therefore means that the emission detected in the SED in such regions would be overwhelmingly dominated by the massive stars, and for the rest of this work means considering only the massive stars in our work is accurate and does not hinder the quality of the results found.

A final note of the practicality of our findings in observation is that due to the large distribution of wavelengths measured for the SED, extinction effects can be more prominent in the higher wavelengths than in that of the lower wavelengths, which could lead to inconsistencies across H II region comparison, and with the nature of this method, could significantly prohibit its applicability unless extinction between the H II region and the Earth is appropriately accounted for in the line of sight of the H II region.

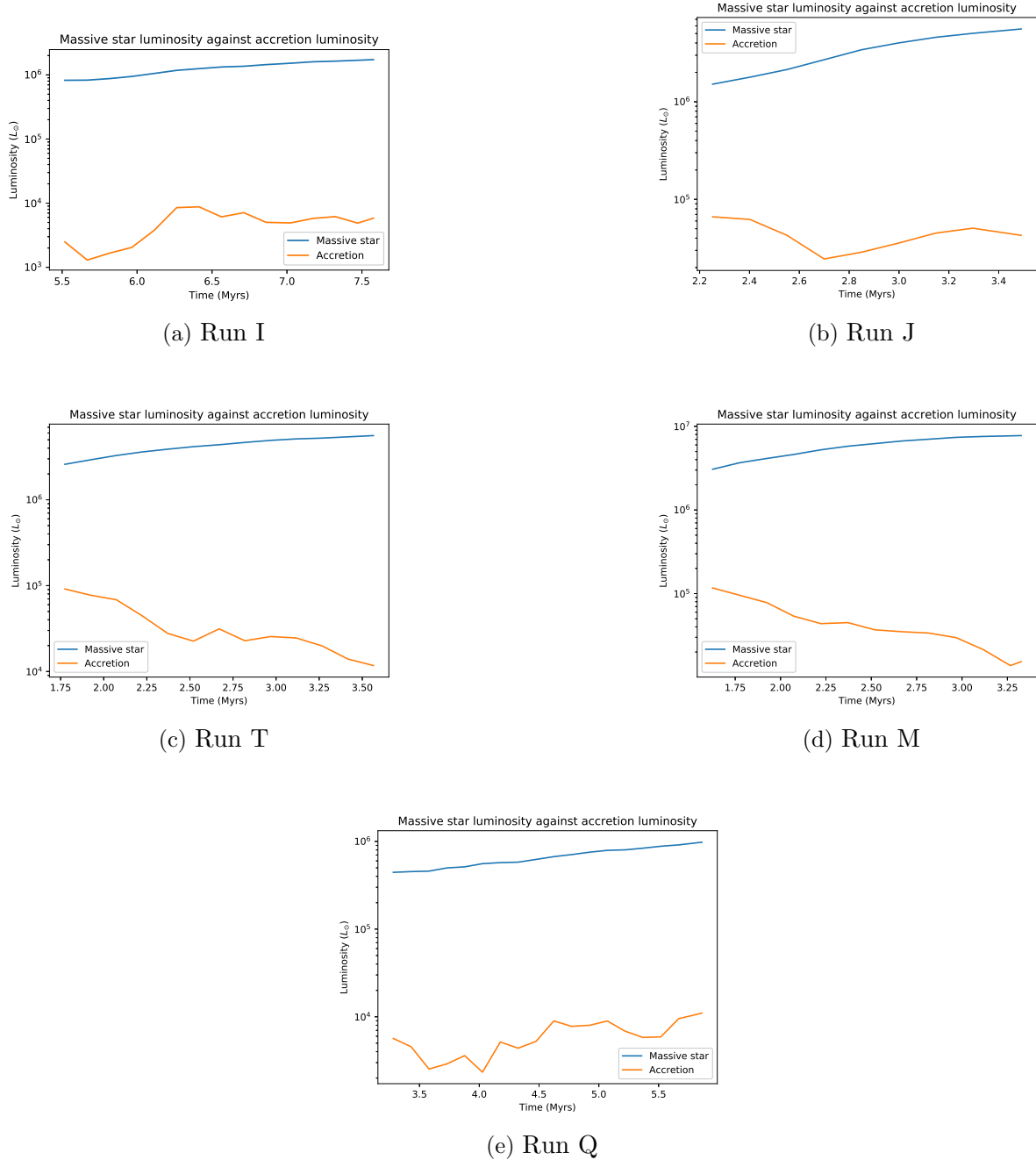


Figure 18: A comparison of the accretion luminosities for the low-mass stars against the cumulative luminosity of the massive stars against time. It is evident that the amount of lower mass accretion luminosity is substantially lower than the massive star luminosity, meaning that for all intents and purposes the exclusion of this emission means only losing a negligible amount of emission light in SED calculations.

Using these figures and making the rather crude assumption that all of the emission from the massive stars exists in the UV and that all of the accretion luminosity is in the IR we obtain a single plot that gives the ratios of the two for each run with time, given in Figure 19.

We see similar behaviour between this new plot and the previous plot which did not consider any emission regarding lower mass stars. These similarities come through the occurrence of a significant drop with time of the ratio in Runs J, T and M, with a more chaotic evolution with time for I and Q. This may therefore suggest that firstly these emission mechanisms exhibit similar evolutionary patterns with regards to their emitted radiation with time, and also that should this data be combined with our first plot, this new data could support the decaying shape seen in Figure 16. The most important property, however, is that the fraction of accretion luminosity to massive star luminosity is so small that it can be considered not influential in our work.

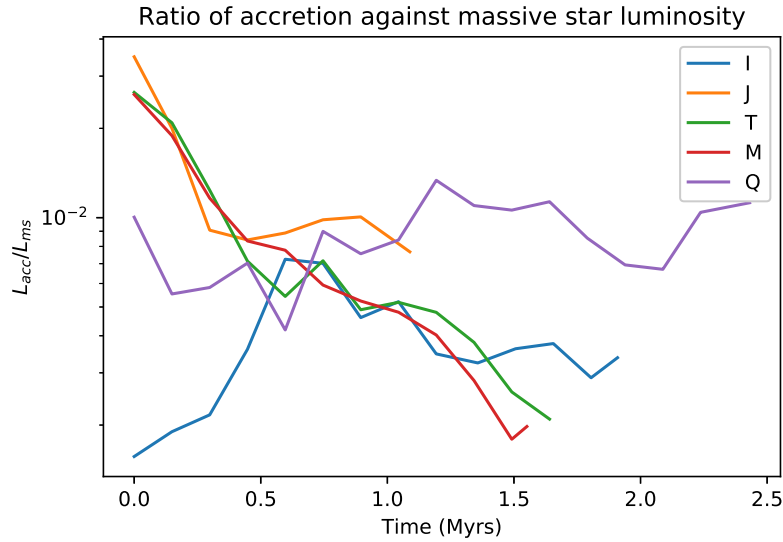


Figure 19: Emission ratio of the massive star luminosity against accretion ratio as a function of time for each run. There are similarities found between this plot and that found in Figure 16, which although the level of emission is negligible compared to the massive star emission, if included then the two mechanism’s emissions could be expected to match in shape and trend.

7.5 Consequence of orientation on apparent morphology

It is no secret that different orientations of celestial objects can lead them to look very different and almost unrecognisable compared with the same thing side-by-side. Take a spiral galaxy for example. Viewed along its galactic plane we see a long smear of gas, dust and stars with no distinguishable visible features other than a streak of star formation. However, taking a look along the normal to the galactic plane and you see an abundance of characteristics from spiral arms to the bright galactic centre, AGN and even down to H II regions and massive star clusters. The same is evident in H II regions, as they do not evolve equally in all directions due to their anisotropic expansion from accretion flows and inhomogeneities in the cloud.

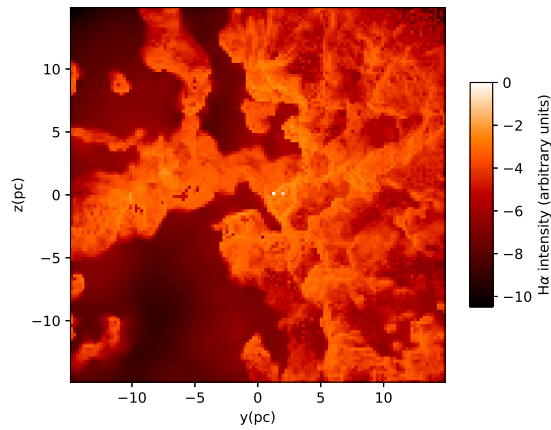
Referring back to the discussion on morphologies in Section 3.2, there are multiple classifications that rely on the physical appearance of the H II region. Yet, with H II regions appearing different depending on from what angle we observe them, it raises the question of

how we can thus define them based upon this visible process. To study the level of impact on the observed shape due to the orientation, a simple experiment was carried out that took one simulation, and took three images of it looking down the x , y and z axis. If classifying H II regions in this way is to be reliable, then it must be the case that they can be classified through this regardless of observational limitations.

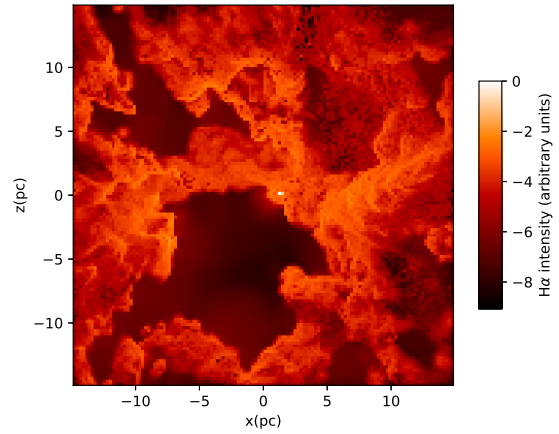
Figures 20 and 21 demonstrate how H II regions can look different due to the plane presented to the observer. The definition of the ionised region is obscured along other axes—appearing smaller and containing more gas than seen in the y -axis looking at Figure 20. Further to this, the shell is smaller, and with these two factors it would probably lead to the classification of a shell, whereas along the y -axis it may be classified as a cleared shell. This consequently leads to a misleading approach to trying to find properties beyond what can be visibly seen after determining where it should sit in the classification system. As such, it is possible and likely that in works where these style of classification systems have been adopted, there has been a large crossover due to the misconception of believing orientation may be a redundant factor to consider. Further to this, there is another dilemma hidden in the fact that if an H II region looks different dependent on its orientation, and that you can classify to be multiple things simultaneously because of this, can you classify it at all? And if we decide that regardless, you can still classify it, which is correct? It is for this reason that we cannot rely solely on the morphology and shape that we see to calculate (approximate) ages and stages in evolution.

Figure 21 strongly represents the extent of the difference that can be seen when looking at H II regions from different angles. This is a case where the differences between the two shapes are so significant that along the z axis you would see two very well defined H II bubbles forming a lobe, and conclude that there is significant massive star formation, but along the x axis there is a very different situation. The cloud appears far more fragmented in many areas and is difficult to determine exactly what activity is occurring. It would be evident that there is star formation taking place but the abstract nature of the environment means that identifying what stars are causing the destruction is very challenging.

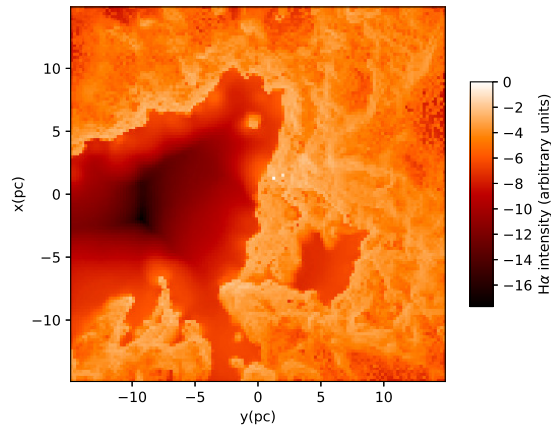
On account of this, having tracers that can identify the class of an H II region regardless of orientation would be very helpful. Hence, it may be beneficial to study how the SEDs are affected by the morphology, since this is a factor that we know regardless of orientation, and the SED is a reliable source of information that observers can retrieve. Furthermore, with evolving activity of star formation, the kinematics and dynamics of the particles within the gas cloud are constantly changing, which results in a (potentially) changing turbulent velocity field. Results from Section 4.3 could also identify ages, and therefore assist with classifying H II regions.



(a) Observation along the x-axis

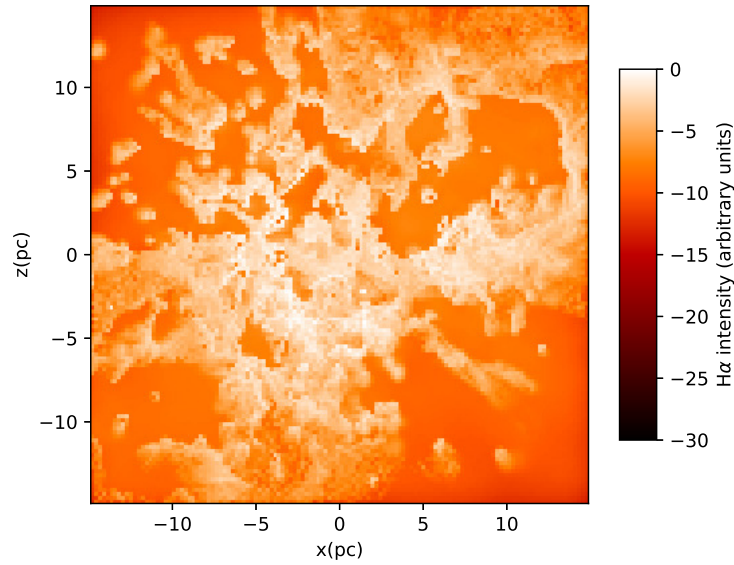


(b) Observation along the y-axis

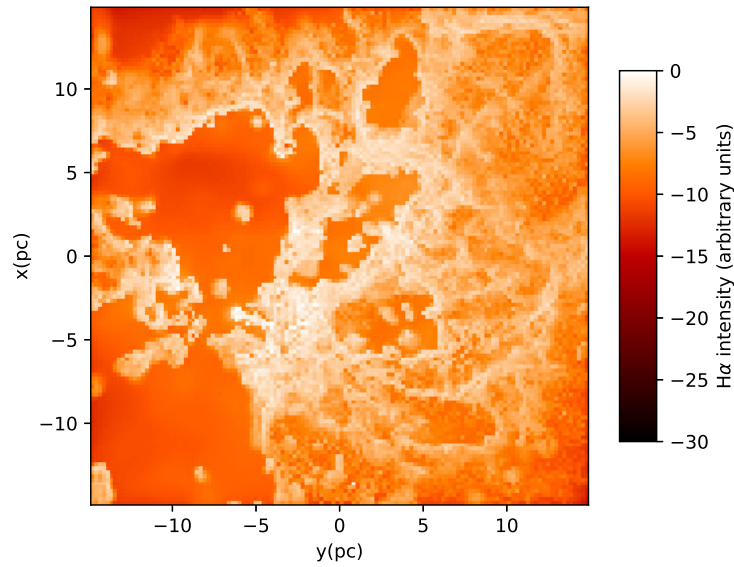


(c) Observation along the z-axis

Figure 20: Observations of the H II region along three different axis from Run I at 2.2052 Myrs. These three viewing angles highlight how the perception of an H II region, and how you may classify it, change. Along the z axis a clear bubble can be made out, however along the x and y axis this is not so apparent and they may instead be classed as mixed or filled shells, as opposed to 20c.

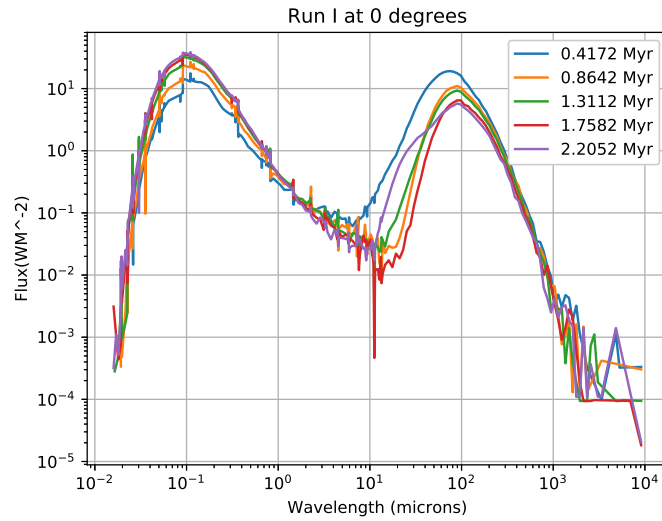


(a) Y-axis

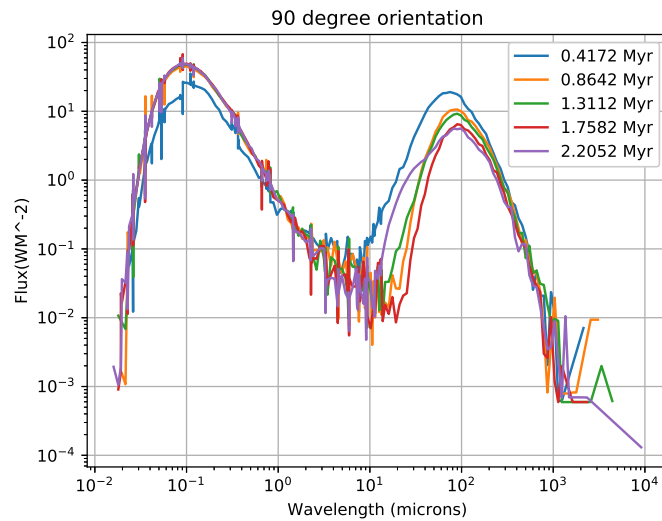


(b) Z-axis

Figure 21: Run T at 1.9072 Myrs from two different observation angles. We very clearly see how the bubbles found along the z-axis are almost completely unidentifiable along the y-axis, illustrating how classifications can again be very different depending on what part of them is made visible to the observer.



(a) SED over time along the z-axis



(b) SED over time at 90 to z axis

Figure 22: SED comparison from two different observation angles for Run I. The two plots are the same in shape and features, and almost identical with regards to the peaks of both the UV and IR parts of the SED. There is noticeably more activity at approximately $10^1 \mu\text{m}$ but the origins of why we see this at a different orientation is not fully understood.

Studying Figure 22 we can see how observing an H II region from a different angle has only slight effects on the SED. Further SED comparisons from the other runs can be found in Appendix B, and reinforce the little change in SED from orientation. Considering that H II regions can present themselves as different classes of H II region purely based upon what angle we can observe them, this gives us a property and potential tracer that is independent of the orientation at which we observe the object. Knowing this, it therefore confirms that classifying H II regions by their physical shape and thus describing the SED from that is potentially unreliable, and instead methods should be made to apply this in reverse- taking

the SED and thus determining the level of star formation, how well cleared out the clouds are and potential age of the H II region.

7.6 Derived Structure function

A description and discussion of structure functions was given in Section 4.3, and the results from our methods for the structure function are now given in this section. For observers, it poses a very challenging task to be able to accurately determine the density of gas and dust within a given region to the spatial scales that would be required in order to derive an accurate structure function that is density weighted and a small-enough resolution to be able to successfully show the behaviour of the turbulence.

Electron density maps have been successfully obtained, depicting the ionisation spread across these types of regions, including work by McLeod et al. (2015) and McLeod et al. (2019) where electron density maps of the Pillars of Creation and N44 and N180 were produced. These were made through the use of the [S II] doublet, taking the difference in their intensities for each cell. The electron density maps typically give an accurate description of the ionisation at the ionisation front, however beyond that are unrepresentative due to the ionising radiation not yet reaching these parts of the cloud. Regardless, given that the electron density map would depict the behaviour of electrons, and that there is one electron for every one hydrogen atom, this would therefore mean that the electron density inside the H II region should also be representative of the density of H^+ . These may give assistance in attempting to better density-weight our structure functions.

In this work we modelled three different type of structure function - a structure function that is based purely on the velocity data of the simulation, a structure function that incorporates three different emission lines (each tested separately) from each pixel and finally a structure function that uses the velocity data and the electron density data together.

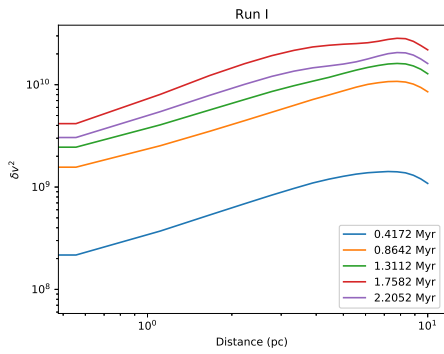
Starting with the velocity data only, Figure 24 illustrates for every run the time evolution of the structure function. The first set of structure functions come from the modified, adapted approach to structure functions where we used circular bins. For every time step in every simulation we see the similar trend of a close to power law shape. All of the simulation structure functions quickly tend towards a similar shape- with the shape and value being maintained for the duration of the simulation. This could be the result of one of many reasons or a combination of all. H II regions maintain a near-equal energy gain/loss mechanism where they gain energy from the ionising stars that absorbs into the surrounding gas and dust, and then loses energy through photon emission and doing work on cold gas. The gas particles will not continuously increase in kinetic energy due to the maintained energy loss as already discussed, however it is not immediately clear as to why there are not noticeable differences at small scales and larger scales. With radiation not yet reaching further spatial scales at especially earlier times, it may be more predictable that the difference in energy becomes increasingly greater with time. Instead we find that for Runs T and M the increasing deviations of difference do not extend beyond the second simulation dump, and with Run J it is not beyond the third. Further to the difficulty in understanding these functions, it is apparent that there is no correlation between the behaviour of the structure function and the Virial ratio of the clouds, which may have explained this occurrence.

Run I depicts a pattern that is more predictable to the situation happening, with the

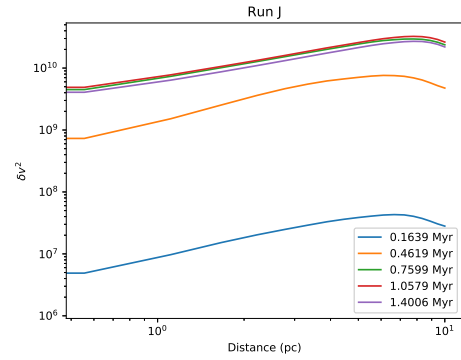
magnitude of the differences increasing with time, and Run Q shows a not-to-distinct difference from the same pattern. The intensity of the structure function with time increases, and the difference between smaller scales and larger scales becomes more significant. Studying the final structure functions of each simulation to determine whether a $R^{2/3}$ power law is maintained, where R is the distance from any given point, fits to each function were made and for I, J, T, M and Q the fits had powers of 1.04, 1.05, 1.07, 0.96 and 1.03 respectively. I do not present uncertainties with these measurements as there are no uncertainties within our emission measurements or our velocity measurements. This is due to the fact that I can extract the exact value of the velocity, emission of any given line, or spatial distance from any point for any particle or cell from the simulation, and because of this, I know that this is the true value of a given variable without any inferred error. As a consequence, with no error bars on our data, I cannot give maximum and minimum fit lines to constrain uncertainties. These power laws were fitted only for the data up to approximately 11 parsecs, as after this the structure function curves downwards for reasons that are not fully clear, but may be due to these distance being less well defined as a result of the method used. The powers are higher than the power law predicted of $R^{2/3}$, but considering that a power law is prominent and well defined in the plots suggests that the turbulence may still behave in a similar way. The higher power law means largely that at further distances the difference in the velocities are greater than expected, but not that they are necessarily higher. This is studied in more depth by analysing the progression of the velocity field through the cloud.

Referring back to previous discussion, considering that to achieve these structure functions came at the cost of a more time-expensive method, investigating the square bin structure functions may shed light into whether they are viable options in making these measurements. Although for the rest of the results I will present are through the circular bin method, this is still important to highlight for the benefits of time efficiency, as well as supporting our further results by showing that through two different methods we can achieve similar structure functions. These structure functions are given in Figure 24. The similar trend in how the structure functions evolve with time in each of the simulations between square and circular bins reinforces that certain large jumps, such as the ones seen in Runs T, M and J are in fact characteristic of the clouds themselves and not an error in our method. Given that for all of these jumps, they happen between the first and second time steps, which would suggest that the cloud exhibits significantly less turbulent activity in comparison to later times.

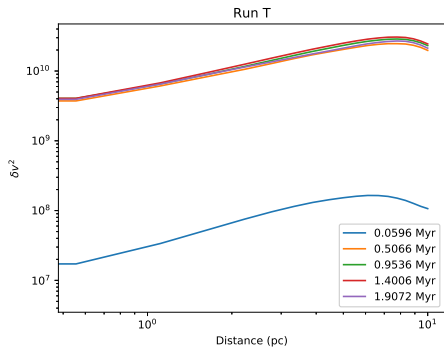
To study further the nature of the structure function and investigate how the average velocity with distance from the centre of mass (CoM) evolves, circular bins are plotted at further distances from the centre of mass of the cloud (taken to be from the centre of the grid as the approximate CoM). This may assist in understanding why we see such an increasing power law with time. These measure just the average velocity within each bin, and the results are shown in Figure 25. They show that as the bubble expands and the photoionisation carries to further distances, the velocity of the particles within the cloud increase up to the a distance where beyond this the gas is likely to still be largely unperturbed. For the earliest plot, the average velocity with distance is relatively uniform, likely being due to the unperturbed initial velocity profile given within the simulations. Following on to the next plot, the gas inside the forming bubble is increasing in velocity even though it is still very much contained in a small volume inside the cloud evident through the overall



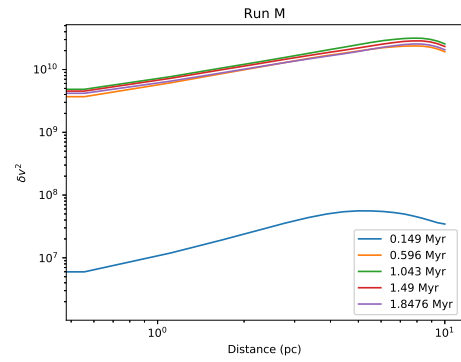
(a) Run I



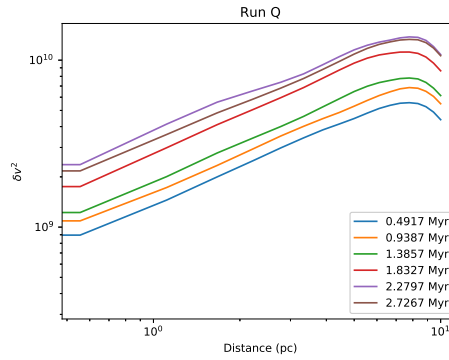
(b) Run J



(c) Run T

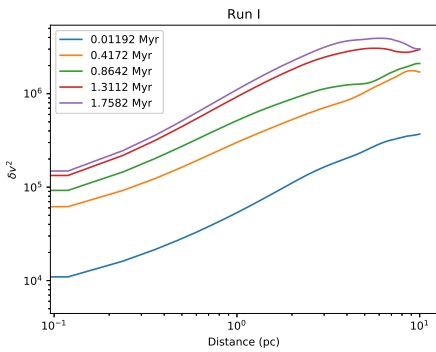


(d) Run M

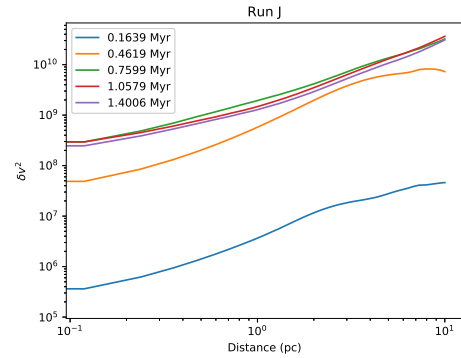


(e) Run Q

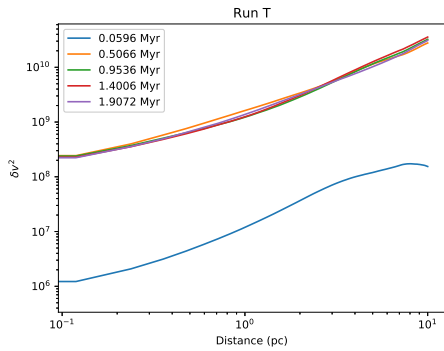
Figure 23: Structure functions for velocity data for each run as an evolution with time. The units of the y-axis are $(ms^{-1})^2$ and the drop-off seen at the largest distances in all time-steps is due to the lack of data points within these bins. Differences in results for each simulation are the combination of different properties of the clouds, such as vary radii, densities and virial ratios.



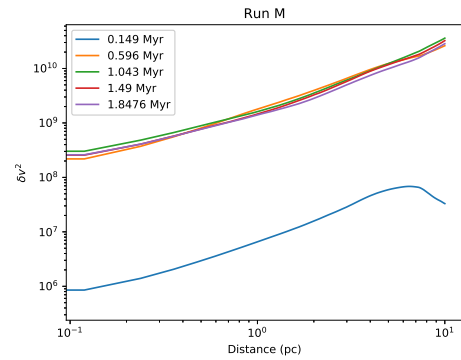
(a) Run I



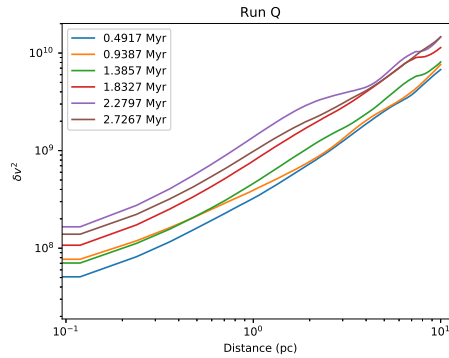
(b) Run J



(c) Run T



(d) Run M



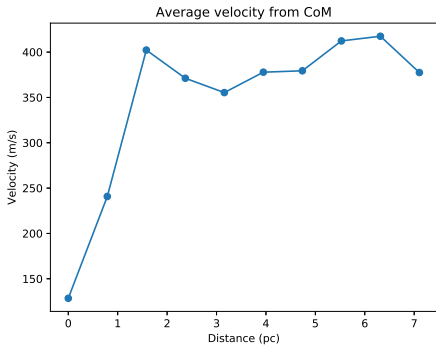
(e) Run Q

Figure 24: Structure functions for velocity data for each run as an evolution with time using the square bin method. The drop-off at some large scales is due to the lack of points within these bins, but amount of times this drop-off occurs is reduced in this method. The units on the y-axis are $(m s^{-1})^2$.

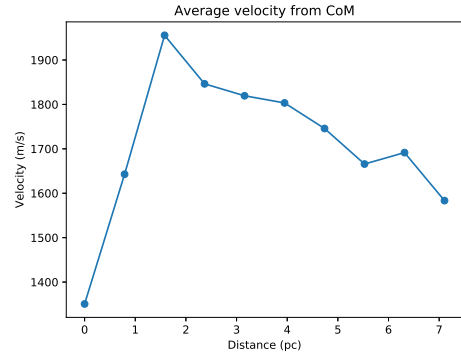
profile of the second plot. At the third plot and onward, we see significant development throughout the entire cloud, which correlates with what our emission maps show. Overall, we see that with time the general trend is that the velocity function follows the ionisation within the cloud, or maybe more specifically, the hot gas outflows from the ionised region. Deviations of this are present in plots at times for 1.3112 Myrs and 2.2052 Myrs where at the beginning we see an initial decrease in the velocities before the continuous increase in velocity magnitude. Although the absolute cause cannot be pinpointed, it may be the result of newly forming massive stars within the vicinity of 1-3 pc of the centre of mass that disrupt the gas particles. These anomalies would then resolve themselves with continued absence of mass star formation, and then when another local star close to the CoM forms, we again see a disruption. This is backed and evidenced from earlier results in Figure 15 where for Run I we see a boost in massive star formation between 0.8642 Myrs and 1.3112 Myrs, followed by a period of no star formation between 1.3112 Myrs and 1.7582 Myrs, and finally the presence of 1 new massive star between 1.7582 Myr and 2.2052 Myr. The timing of these formation events ties in with what we have seen in the velocity profiles. Consequently, this leads to the possible conclusion that the structure function does indeed follow the hot gas, and as a result the structure functions we found are likely tracing the hot gas within and escaping the bubbles more so than the cold gas.

These results suggest that the overall impression of the gas movement is that it is moving outwards - away and out of the bubbles. When we look at individual points and take velocity bins around them, we see an effect that is not dissimilar from the Hubble expansion model where all galaxies see other objects moving away from themselves regardless of their location - with faster galaxies be at further distances from the centre and slower objects located closer. Given that it is the same in our cloud scenarios, each cell registers (nearly) every other cells velocity as moving away from it. But what is effecting our structure functions is the combination of both the outward expansion velocity of the gas and the turbulence. The outward expansion is leading to the further distance particles travelling faster as well as the addition of the turbulence which has the effect of creating a steeper structure function than predicted. Whereas the $\frac{2}{3}$ is for an incompressible turbulent gas, we have a turbulent gas that also has the intrinsic property of the velocity field having an outward flow. Overall, this may explain why our structure functions exhibit this steeper gradient.

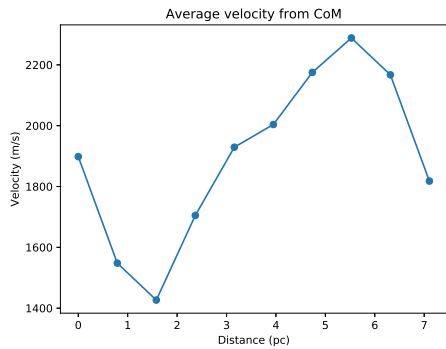
From this point, $H\alpha$, [O III] and [N II] emission were included into the velocity data through multiplication of the intensity of a given cell in a specific emission line with the velocity value in that cell. This would allow for whether certain emission lines traced better throughout the entirety of the cloud. We omit [S II] from this work for the three following reasons. Firstly, in work carried out by other authors, [S II] did not act as a good identifier for structure functions, secondly MOCASSIN struggled to converge many of the cells in this emission line and thirdly, [S II] emission is only prominent in very few regions of the entire H II region and cloud. As already mentioned, McLeod et al. (2016) found that [S II] and [OI] returned noisy structure functions, with the $H\alpha$ and [O III] yielding power laws on small spatial scales. In this work we do not study the [OI] line but instead use [N II], which allows for further insight into finding an ideal emission tracer for the structure functions. We start first with $H\alpha$ since this likely to trace the hot gas and ionisation of hydrogen, as our velocity results suggested that the structure function traces hot gas.



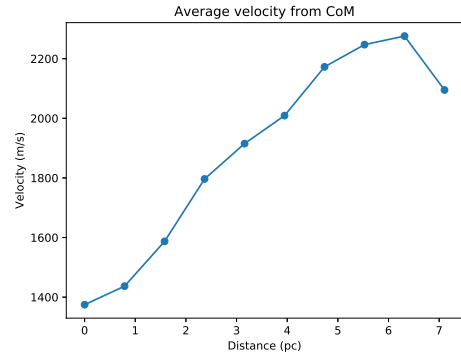
(a) 0.4172 Myrs



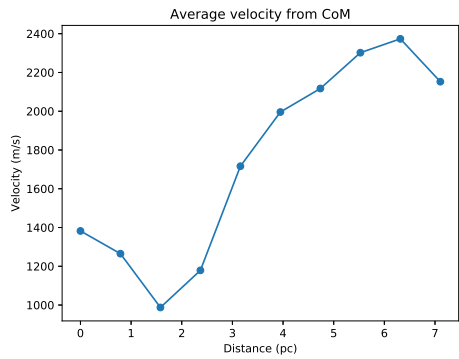
(b) 0.8642 Myrs



(c) 1.3112 Myrs

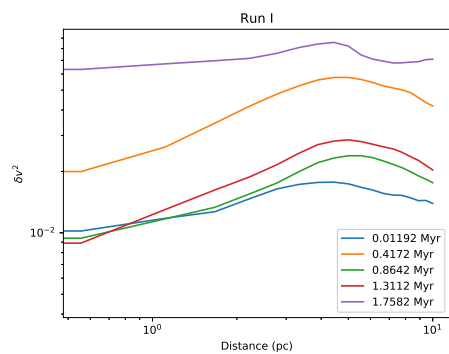


(d) 1.7582 Myrs

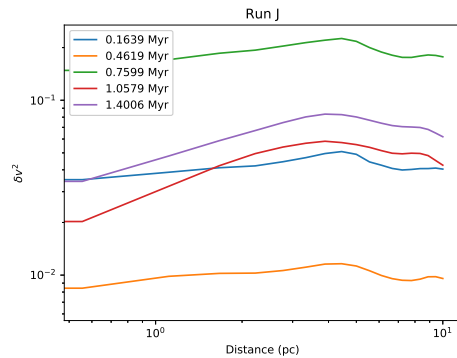


(e) 2.2052 Myrs

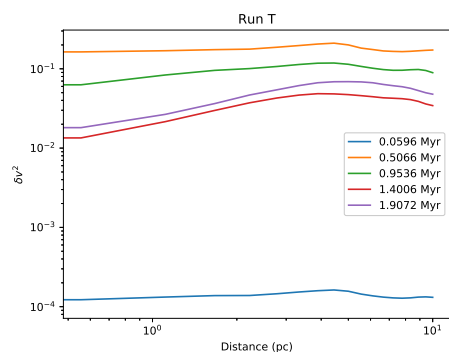
Figure 25: Average velocity of all the gas with increasing distance from the centre of mass of the molecular cloud. It is possible to infer from the smaller spatial scale behaviour when new massive stars formed as the general increasing velocity trend becomes distorted. The overall increasing trend fits in line with the concept the the gas (or more specifically the hot gas) is moving with a net outward flow.



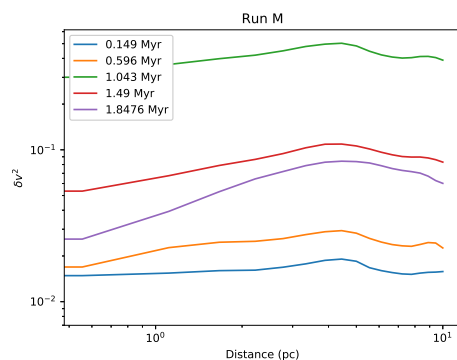
(a) Run I



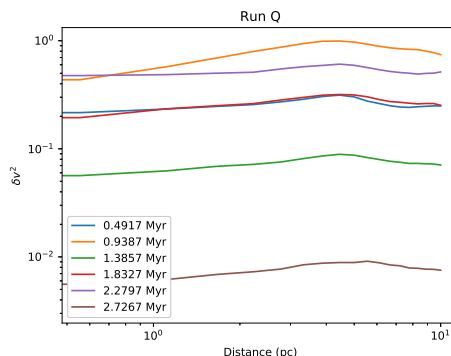
(b) Run J



(c) Run T



(d) Run M



(e) Run Q

Figure 26: Structure functions in $H\alpha$ emission. The units on the y-axis are $(ms^{-1}Wm^{-2})^2m^{-3}$ which simplifies to $m^{-4}s^{-1}W$ (however the units are not as descriptive in this format) but I still denote the variable as δv^2 as the units do not represent a single given quantity, and this data is representing emission and density-normalised velocity data. There is no clear trend within the data that could suggest a Kolmogorov-type power law present, or a power law that would fit in like with the ~ 1 power that we have seen in our previous structure functions.

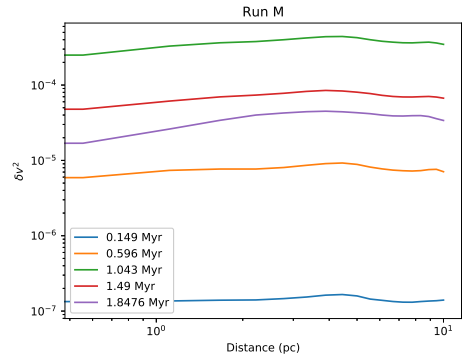
The structure functions with $H\alpha$ do not present prominent power laws or any distinct repeatable features. The only features we see are the noticeable increase in the function with

time - likely due to the overall increase in $H\alpha$ emission as more gas is ionised or that as the stars accrete more and more gas with time, the average velocity of particles increases giving a greater range of velocities with the result of lifting the whole function up the y axis. The loss of data after this point, resulting in the subsequent drop off in the function may be due to the lack of $H\alpha$ emission at these distances, since the photoionisation has not yet reach that far. Moreover, given the fact that this occurs at all times in simulations such as Runs M and J, it may also be due to the whole method of creating the structure function, as if $H\alpha$ is very present closer to the centre, then that means that fewer randomly selected points to sum bins around may feel the influence of the $H\alpha$ at larger distances. This is all, however, speculation and would require further investigation to find the true cause of this. Making power law fits to the structure functions with $H\alpha$ emission did not yield any further insight, with powers varying between 0.2 and 1. As such, even though across different time steps we can find evolutionary patterns for a given simulation, these features do not carry across to different initial conditions.

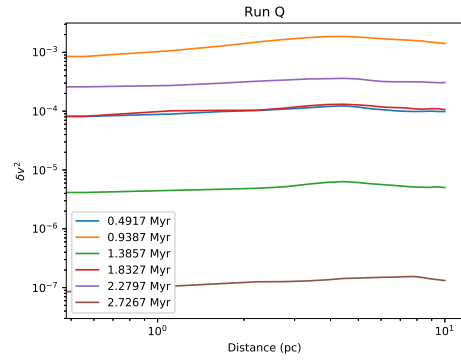
Appendix C contains the structure functions including [O III] and [N II], and we find that these emission lines do not bring any new indicators as to being able to trace the turbulence or extract the true structure function through the emission. The functions are very much flat in both emission lines for Run Q, indicating that the velocity field is random at all distance scales. Runs J, T and M also exhibit very similar behaviours in being largely flat across all time steps. This again implies a high level of randomness and noise. It is only with Run I where we see any kind of positive correlation in the data, but even this is not of the order seen in the velocity only functions, and eventually becomes a flat function regardless. As a result of these findings, I find that these emission lines, at least on their own, are not able to extract the structure function from these simulations.

The final method used for structure functions was applying electron densities to each cell to infer a simple level of density-weighting. This was only applied to the structure function involving $H\alpha$ emission based upon the mechanism behind this type of emission. Given that $H\alpha$ is a tracer for hydrogen ionization, electron density weighting would identify regions where there are higher levels of ionization and lower (given that free electrons are the result of such ionization), and therefore weight them accordingly. This method is not applied to any other emission lines as the electron density does not trace the emission of other lines in the same way that it can accurately trace $H\alpha$.

The electron density weighting was calculated through the study of the [S II] doublet - taking the difference between the two fluxes for every cell. This value, which would represent the electron density of that cell, is then multiplied by the velocity and $H\alpha$ emission in that cell and the same structure function method is carried out. The results for Runs M and Q are given in Figure 27 since these gave the closest to any real correlation, and show how despite the ability to deal with some of the more chaotic behaviours at the higher spatial scales in the original $H\alpha$ plots, they still did not lead to a power law of any sort, and the horizontal lines indicate that this is just noise.



(a) Run M



(b) Run Q

Figure 27: Electron density weighted structure functions in $H\alpha$ emission for Runs M and Q. The electron density was used to weight the $H\alpha$ emission by multiplying each cell $H\alpha$ value by its electron density value. We see no significant or distinguishable trend or pattern within the plots, and does not correlate to the velocity structure functions, which is what I hoped to extract.

7.6.1 Hot gas only

To further investigate the nature of the turbulence in the cloud, and specifically attempt to study the structure functions yielded from the simulations, a look at the hot gas will help study if the photoionization of the gas is the main contributing factor to the influenced turbulent field. I only study particles at temperatures above 5000 K to give a large-enough clearance from the cold gas.

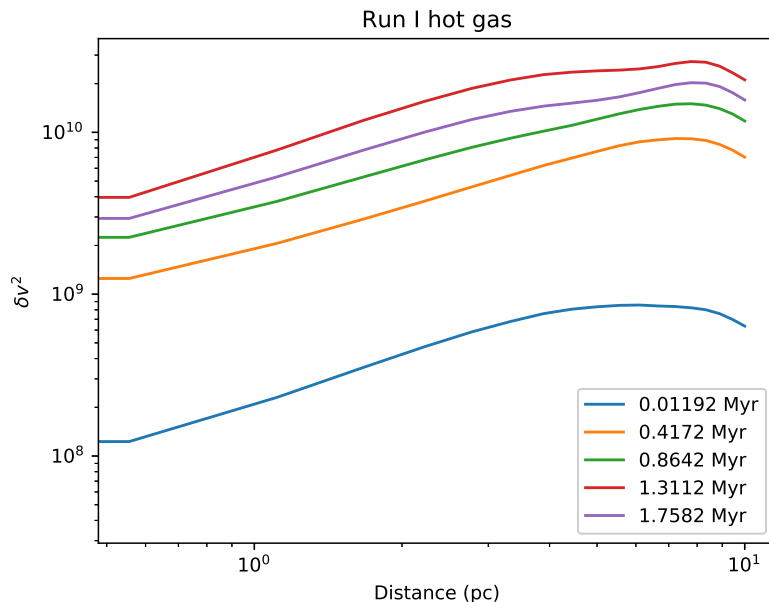


Figure 28: Structure functions for only the hot gas in Run I simulation dumps. The shape of the plot is very similar to that found with hot and cold gas considered. The similarity suggests that the shape of structure functions is dictated predominantly by the hot gas properties inside the gas cloud; with the cold gas playing very little part in altering the slope found.

Comparing the results of studying only the hot gas with the structure function with all the gas, we see almost no difference in the results. The only slight deviation between the two arises at the earliest time step where the drop off at the edge is less sharp in only the hot gas, which may be a result of the more gradual drop-off of hot gas at further distances from the centre as opposed to the gas of any temperature. The conclusion of this result, along with results from Figure 25, is that the structure functions obtained in this work are dominated by the tracing of hot gas within the cloud, and this therefore implies that the functions trace more the outward flowing gas from the bubbles.

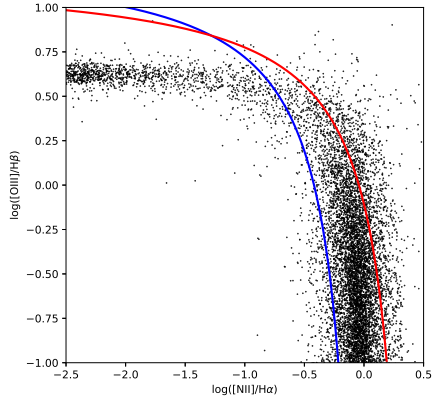
7.7 BPT diagrams

Baldwin et al. (1981) investigated how different excitation mechanisms can be classified through the ratio of forbidden metal lines. They state that ionization through H II regions, planetary nebulae, power-law continuum and shock-wave heating can all be separated by the production of BPT maps (Baldwin, Phillips and Telervin maps). The requirement for a method such as BPT maps came from the study of unresolved galaxies and AGN, where it could not be determined whether the dominant emission mechanism was photoionizing radiation from H II regions or shocks. Kewley et al. (2001) fitted a cut-off on the BPT map that indicated where emission due to star burst would stop and due to shock driven would begin. This is known as the Ke01 extreme starburst line. Referring to Figure 1 from Kewley et al. (2006), galaxies that lie below this line have their emission dominated by star formation, and is where the H II regions in this work would expect to be found.

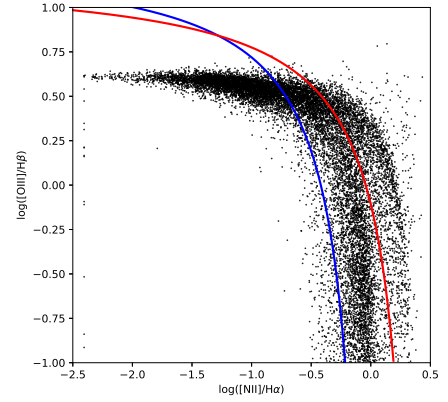
Positions above the line belong to shock dominated emission, and this can be further split in classification to whether the galaxy is LINER or Seyfert. Kauffmann et al. (2003) further developed a classification line that defined the lower limit for galaxies, as it was stated by themselves that the previous starburst/AGN line gave a *'conservative lower limit on the true nature of the number of AGN'* in the sample they used. Despite this, the newer lower limit does not exist for all ratio maps.

Specific ratios can also be indicative of certain properties of the radiation. For example, the ratio of $[OIII]/[OII]$ is sensitive to the level of ionisation in the gas and $[OI]/[H\alpha]$ has sensitivity towards the level of hardness in the radiation field. Furthermore, in the field of galaxy work, whether the galaxy is a LINER galaxy or a Seyfert galaxy can be determined by the position on $[OIII]/H\alpha - [SII/NII/OI]/H\alpha$.

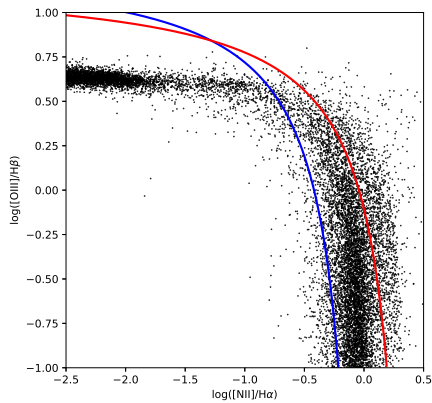
The maps are constructed through plotting collectively the value for the desired emission line ratio for every pixel in the image and plotting one ratio against another. All of the simulations we use in this work are unable to simulate or identify emission through shocks - leading to the definitive knowledge that all emission from MOCASSIN in all wavelengths is from star bursts and formation. As a result, it is expected that all points are to lie below the Ka03 classification line.



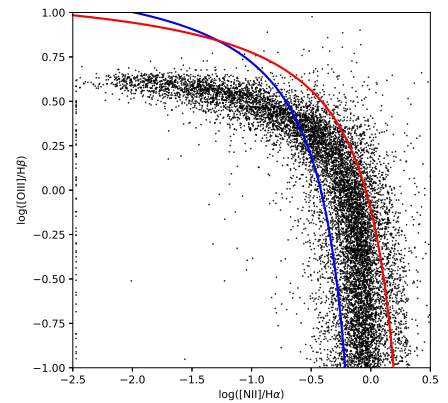
(a) Run I



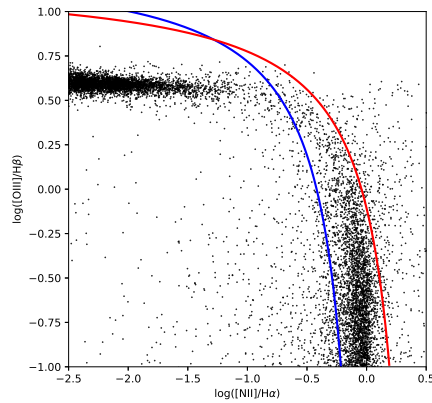
(b) Run J



(c) Run T



(d) Run M



(e) Run Q

Figure 29: BPT maps of $[OIII]/H\beta - [NII]/H\alpha$. Here the red line represents the Ke01 extreme starburst line and the blue line is the Ka03 classification line. A large portion of the data extracted from the maps lies outside and above the classification lines, which is counter-intuitive to what is expected as it is in these regions of the map where emission due to shocks is located- something that is excluded entirely from these simulations. This may, however, be due to the resolved nature of these regions, whereas these maps are typically used on unresolved galactic objects.

Figure 29 illustrates the BPT maps for the last simulation time step for every run. Contrary to what was expected in the behaviour of the emission ratios, the BPT maps from all runs exceed the Ka03 classification line boundary, which should not be possible given the physics of the simulations. This is not, however, a unique result. Ercolano et al. (2012) retrieved similar results in their BPT maps when studying observations of synthetic pillars intended to mimic the Pillars of Creation. They found that for higher distances from the ionising sources the ratio exceeded both the Ka03 and Ke01 line. In our maps, we see that the Ke01 line gives a better representation for where H II regions are ‘allowed’ to appear on the map. Even so, multiple cells still occur beyond the boundary of this line which defeats the objective of implementing this boundary. It is not known the spatial distances from the sources for each point, unlike the work from Ercolano et al. (2012), but this finding suggests a breakdown in the applicability of the lines in classifying galaxies that are unresolved.

Given that these results deviate so much from the Ke01 and Ka03 lines, I produced a new, empirically derived fit based upon all the BPT map results from every simulation and time step. The fit traces the upper boundary contour, and encompasses the majority of points within the map. Mathematically, the contour is described by Equation 22 and is consistent across all BPT maps produced in the $[O III]/H\beta$ - $[N II]/H\alpha$ ratios.

$$\log\left(\frac{[OIII]}{H\beta}\right) = \frac{0.15}{\log\left(\frac{[NII]}{H\alpha}\right) - 0.45} + 0.8 \quad (22)$$

Figure 31, as well as figures found in Appendix D illustrate the new fit on all plots. It is evident that the contour provides a close fit to the upper limit for every H II region, regardless of initial conditions, level of star formation and morphology. As a consequence, it may be that for H II regions their BPT plots can be better described separate from that of larger scale galactic classification. It is evident from our work and Ercolano et al. (2012) that when studying individual H II regions the classification lines break down. In spite of the lines being used for galaxies as opposed to smaller cloud regions, this should have no effect as it is a summation of many of these regions that lead to galaxies with star-formation dominated emission. If we are seeing, for all of our H II regions, that the regions far exceed the supposed boundaries of the Ke01 and Ka03 lines, then it becomes apparent that there is a breakdown in the efficiency of these lines towards star-formation dominated emission. For this reason, the new contour we are able to plot may give a better boundary when applying BPT maps to individual H II regions, since we are able to evidence its consistency within simulation across a multitude of region types. It is supported through repeated experiment that there is a measurable boundary that constrains the ratio data of H II regions, and we have been able to quantify it, however the reason why the simulated H II regions are ill-defined by the Ke01 and Ka03 lines is yet to be fully understood. Zhou et al. (2014) investigated the excitation properties of multiple H II regions within Arp 86 using BPT maps. They too found that the maximum starburst line of Kewley et al. (2001) was more accurate at defining the starburst cutoff than the newer classification line of Kauffmann et al. (2003). There is thus the potential that our new line defined here gives a better specification for H II regions specifically.

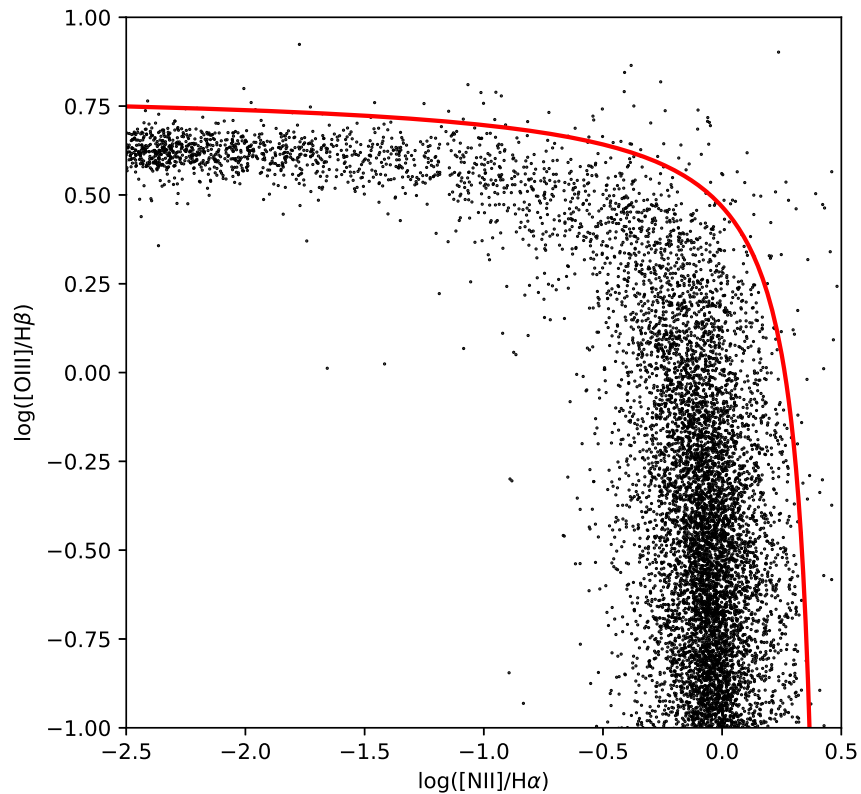
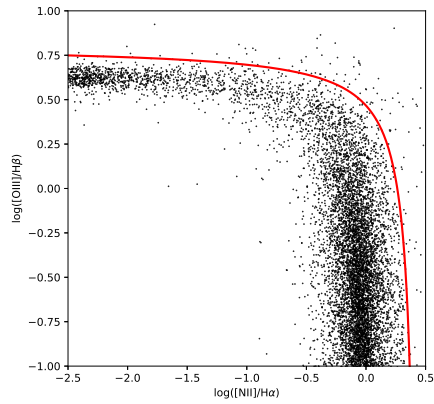
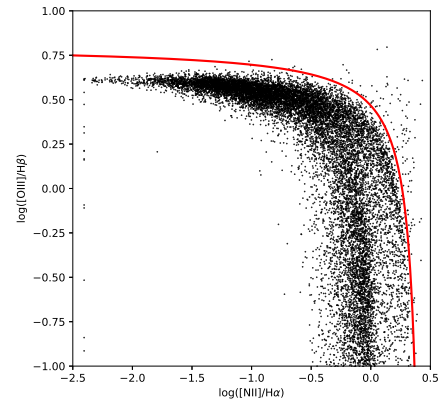


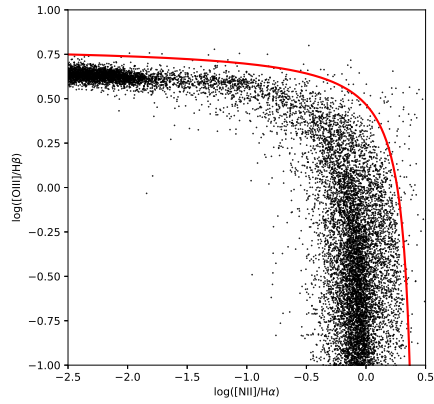
Figure 30: This illustrates a new classification line that I was able to fit that encompassed better the trend given by the data from Run I. Although there are still a few points that lie outside, these account for a very small percentage of the data. This line was empirically derived to explicitly fit this specific dataset, and was then tried against all other data we had gathered. Below the line would exist pure star forming emission, and above the line would be shock-driven emission.



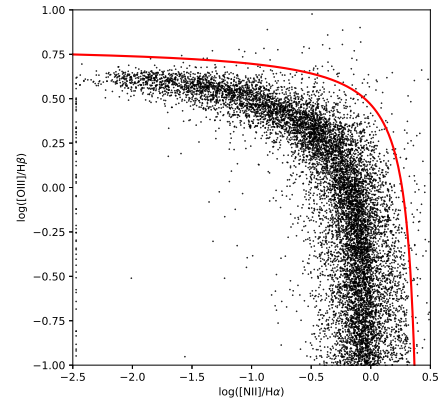
(a) Run I



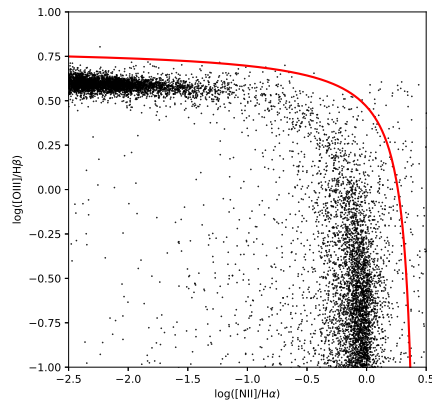
(b) Run J



(c) Run T



(d) Run M



(e) Run Q

Figure 31: BPT maps of $[OIII]/H\beta - [NII]/H\alpha$. The red contour is the new fit I have made to better describe the data within the BPT map for these ratios. The points now consistently lie within the classification line, and this line may be better adapted at dealing with resolved regions- specifically resolved star-forming regions.

8 Conclusions

At the beginning of this project I set out a number of objectives that we set to look into and attempt to address or contribute to the eventual understanding of. We began with building an understanding of what H II regions are, the different mechanisms that operate within them that can contribute to occurrences of turbulence, ionization front expansion (and in some uncommon cases collapse), termination of low mass stars and fragmentation. With this understanding of the true nature of H II regions, this then allowed for a more informed look at how the simulations used in this work would effectively or ineffectively model mechanisms within turbulent molecular clouds. I came to the understanding that the simulations would very well simulate the turbulent effects of photoionization within the hot and cold gas, as well as how both photoionization and stellar winds combined can affect the gas and dust surrounding the massive ionizing stars.

I ran multiple simulations with varying properties, including the addition of dust and winds, the changing of grid resolution, viewing orientation, photon frequency bins and the dust distribution model. The addition of dust in the simulation gave rise to the appearance of a second peak in the spectral energy distribution that correlated to the reprocessing of stellar photons from the UV to the infrared. This inclusion of dust assisted in making the SEDs in this simulatory work more resemble observation. Changing the grid resolution had a number of effects, largely around the quality of images and how accurately (with regards to spatial resolution) MOCASSIN could model the radiative transfer throughout the cloud. The inclusion of winds had profound effects on the molecular clouds in their evolution. It was seen that earlier forming bubbles had more dominance and impact, quenching the formation of later bubbles and hindering the lasting presence of features such as pillars.

A unique opportunity given by the use of simulations is the ability to observe these clouds from any angle. This was utilised in this work and illustrated how in spite of the viewing angle being different, leading to the H II region appearing very different, the SED remained unchanged. This was especially important in the morphological classification of these regions which has been attempted - this finding identified that physical look alone is not enough to classify such regions and that further observations about the star formation and the level of destruction within the cloud need to be made before concluding on its true nature. Allowing for the highest amount of frequency bins that MOCASSIN could use while still maintaining computational efficiency was vital to this step, as through experimentation I found that I was limited in memory usage and without a high amount of bins I could not model the IR emission sufficiently to achieve a usable SED. The final characteristic I had the ability to change was the dust distribution that MOCASSIN used. I discussed how the exact species and distribution of dust found within molecular clouds is a very difficult and ambiguous task, and that I could not qualitatively give a dust distribution that I know would be true to what is found in molecular clouds. Instead, I ran a sample test on 6 different dust distributions from both previous work carried out, and distributions that we do know can be found in certain parts of molecular cloud systems. The results showed that, with the exception of an oxygen deficient distribution which can be found around forming stars in their circumstellar discs, all the dust distributions gave very similar SEDs and results. This confirmed that the distribution we used would be representative of many dust distributions possible.

With the outputs from MOCASSIN for all the simulations, I was able to test methods

to study the evolution and ageing of the clouds. Presenting the SEDs indicated how with age and shape of the region, the SED did not systematically change in ways that were immediately obvious. Further investigation was required to test how it changed, and this was done through measuring the ratio of the IR emission to the UV and part of the visible emission. Selecting suitable frequency ranges and plotting the ratio for each time step in every simulation led to a decaying power law. The nature of the power law appearing to be largely influenced by the level of destruction and the rate at which this destruction occurred. The level of star formation within the clouds also suggested that it may have an influence on the power law, and although these plots are not yet fully deciphered, they suggest that they may give a new way to quantify H II regions and understand better the nature of them without the hindrance of observation angle.

Following the work on SEDs, we then investigated the turbulence within the simulations themselves, and attempted to see if it was possible to extract the turbulent field power law (described by a Kolmogorov-type power law) when emission is included. Building upon previous work done on this, we first quantified the power law in the velocity data of the particles, and then included emission in multiple lines to see which (if any) could return a power law similar to that of the velocity only data. Multiple iterations of the method led to many conclusions regarding both the turbulence within the cloud and what the method traces. Finding a basic structure function with the velocity data gave rise to a power law that was slightly higher than the predicted and initial Kolmogorov velocity field. Using a more computationally simplified square-bin method also yielded a very similar power law but much smaller in overall magnitude. The cause of this could not be determined, but our standard circular bin method gave results with magnitudes the same as other authors' work.

To investigate further the higher power law, mapping of both the velocity from the centre of mass of the cloud and producing structure functions considering only the hot gas indicated that the structure function is dominated by the presence of the hot gas and as such was tracking the hot gas leaving the bubbles and being expelled to larger distances. After this, emission from three different lines were added in ordered to closer mimic how the emission is intertwined with the velocity information, and followed previous methods used with emission in structure functions. Only $H\alpha$ produced functions that still had, on small spatial scales, a power law that could be noted across multiple scales. However, it differed greatly from the velocity only functions and was not consistent across different times. The electron density was then included into both the velocity and $H\alpha$ in an attempt to normalise the ionisation to help reduce the influence of the emission within the functions, but this was unsuccessful and led to noisy structure functions with no distinguishable trends.

I then plotted BPT maps to see if it was possible to fit the Ke01 or Ka03 classification lines to the data, which would then show that the emission is photoionisation driven as opposed to shock driven. This sat in line with knowing that all the emission in our emission lines do indeed come from photoionisation only, however the line fits failed to show this. Due to this, I fitted a new line that both categorized the emission from the H II region and was consistent across all time steps for multiple different initial cloud conditions. This line represented the cut off found in our work where photoionisation and shock emission could be divided.

The work presented here has opened new paths into how we can use current methods to better understand and extract information about H II regions that can further our ability

to understand these regions and what takes place within them. As well as this, we have also taken current methods and tested them against what we can see with the simulations in this work with the intention to highlight to what extent we can see details and processes within clouds of known structures and initial conditions. This work will hopefully assist in breaking through barriers that exist due to our observational limitations and allow for us to understand what we see in its entirety as opposed to what we can physically see with instruments.

Acknowledgements

I would like to thank my supervisor Dr James Dale for his continued support and help during this work with the lending of simulations and scripts, and for his insightful input. I would also like to thank my friends and family for their support during this work and their patience with me while I completed this thesis. I would finally like to thank the University of Hertfordshire and the Centre for Astrophysics Research for allowing me to use their computing facilities to fulfil the work of this project.

References

- Anathpinkida, S. (2008), ‘Smoothed Particle Hydrodynamics Simulations of Colliding Molecular Clouds’, *University of Wales*.
- Anderson, L. D., Zavagno, A., Deharveng, L., Abergel, A., Motte, F., André, P., Bernard, J. P., Bontemps, S., Hennemann, M., Hill, T., Rodón, J. A., Roussel, H. & Russeil, D. (2012), ‘The dust properties of bubble H II regions as seen by Herschel’, *A&A* **542**, A10.
URL: <https://doi.org/10.1051/0004-6361/201117283>
- Axford, W. I. (1961), ‘Ionization fronts in interstellar gas: The structure of ionization fronts’, *Philosophical Transactions of the Royal Society of London. Series A, Mathematical and Physical Sciences* **253**(1029), 301–333.
URL: <http://www.jstor.org/stable/73143>
- Bacon, R., Accardo, M., Adjali, L., Anwand, H., Bauer, S., Biswas, I., Blaizot, J., Boudon, D., Brau-Nogue, S., Brinchmann, J., Caillier, P., Capoani, L., Carollo, C. M., Contini, T., Couderc, P., Daguisé, E., Deiries, S., Delabre, B., Dreizler, S., Dubois, J., Dupieux, M., Dupuy, C., Emsellem, E., Fechner, T., Fleischmann, A., François, M., Gallou, G., Gharsa, T., Glindemann, A., Gojak, D., Guiderdoni, B., Hansali, G., Hahn, T., Jarno, A., Kelz, A., Koehler, C., Kosmowski, J., Laurent, F., Le Floch, M., Lilly, S. J., Lizon, J. L., Loupias, M., Manescau, A., Monstein, C., Nicklas, H., Olaya, J. C., Pares, L., Pasquini, L., Pécontal-Rousset, A., Pelló, R., Petit, C., Popow, E., Reiss, R., Remillieux, A., Renault, E., Roth, M., Rupprecht, G., Serre, D., Schaye, J., Soucail, G., Steinmetz, M., Streicher, O., Stuik, R., Valentin, H., Vernet, J., Weilbacher, P., Wisotzki, L. & Yerle, N. (2010), *The MUSE second-generation VLT instrument*, Vol. 7735 of *Society of Photo-Optical Instrumentation Engineers (SPIE) Conference Series*, p. 773508.
- Baker, J. G. & Menzel, D. H. (1938), ‘Physical Processes in Gaseous Nebulae. III. The Balmer Decrement.’, *The Astrophysical Journal* **88**, 52.
- Baldwin, J. A., Phillips, M. M. & Terlevich, R. (1981), ‘Classification parameters for the emission-line spectra of extragalactic objects.’, *Publications of the Astronomical Society of the Pacific* **93**, 5–19.
- Bate, M. R., Bonnell, I. A. & Price, N. M. (1995), ‘Modelling accretion in protobinary systems’, *Monthly Notices of the Royal Astronomical Society* **277**(2), 362–376.
- Bertoldi, F. & McKee, C. F. (1992), ‘Pressure-confined Clumps in Magnetized Molecular Clouds’, *The Astrophysical Journal* **395**, 140.
- Bianchi, L. & Garcia, M. (2014), ‘The effective temperatures of O-type stars from UV spectroscopy’, *Advances in Space Research* **53**(6), 973–981.
- Bisbas, T. G., Haworth, T. J., Williams, R. J. R., Mackey, J., Tremblin, P., Raga, A. C., Arthur, S. J., Baczynski, C., Dale, J. E., Frostholm, T., Geen, S., Haugblle, T., Hubber, D., Iliev, I. T., Kuiper, R., Rosdahl, J., Sullivan, D., Walch, S. & W^onsch, R. (2015),

- ‘starbench: the D-type expansion of an H&II region’, *Monthly Notices of the Royal Astronomical Society* **453**(2), 1324–1343.
URL: <https://doi.org/10.1093/mnras/stv1659>
- Boneberg, D. M., Dale, J. E., Girichidis, P. & Ercolano, B. (2015), ‘Turbulence in giant molecular clouds: the effect of photoionization feedback’, *Monthly Notices of the Royal Astronomical Society* **447**(2), 1341–1352.
- Bonnell, I. A., Clarke, C. J. & Bate, M. R. (2006), ‘The Jeans mass and the origin of the knee in the IMF’, *Monthly Notices of the Royal Astronomical Society* **368**(3), 1296–1300.
URL: <https://doi.org/10.1111/j.1365-2966.2006.10214.x>
- Brinchmann, J., Charlot, S., Kauffmann, G., Heckman, T., White, S. D. M. & Tremonti, C. (2013), ‘Estimating gas masses and dust-to-gas ratios from optical spectroscopy’, *Monthly Notices of the Royal Astronomical Society* **432**(3), 2112–2140.
URL: <http://dx.doi.org/10.1093/mnras/stt551>
- Brunt, C. M., Heyer, M. H. & Mac Low, M. M. (2009), ‘Turbulent driving scales in molecular clouds’, *Astronomy and Astrophysics* **504**(3), 883–890.
- Chira, R. A., Ibáñez-Mejía, J. C., Mac Low, M. M. & Henning, T. (2019), ‘How do velocity structure functions trace gas dynamics in simulated molecular clouds?’, *Astronomy and Astrophysics* **630**, A97.
- Churchwell, E. (2002), ‘Ultra-Compact HII Regions and Massive Star Formation’, *Annual Review of Astronomy and Astrophysics* **40**, 27–62.
- Churchwell, E., Sievers, A. & Thum, C. (2010), ‘A millimeter survey of ultra-compact HII-regions and associated molecular clouds’, *Astronomy and Astrophysics* **513**, A9.
- Clayton, G. C., Wolff, M. J., Sofia, U. J., Gordon, K. D. & Misselt, K. A. (2003), ‘Dust grain size distributions from m_{rn} to m_{em}’, *The Astrophysical Journal* **588**(2), 871–880.
URL: <http://dx.doi.org/10.1086/374316>
- Dale, J. E. (2017), ‘The effect of the virial state of molecular clouds on the influence of feedback from massive stars’, *Monthly Notices of the Royal Astronomical Society* **467**(1), 1067–1082.
URL: <https://doi.org/10.1093/mnras/stx028>
- Dale, J. E. & Bonnell, I. A. (2008), ‘The effect of stellar winds on the formation of a protocluster’, *Monthly Notices of the Royal Astronomical Society* **391**(1), 2–13.
- Dale, J. E., Bonnell, I. A., Clarke, C. J. & Bate, M. R. (2005), ‘Photoionizing feedback in star cluster formation’, *Monthly Notices of the Royal Astronomical Society* **358**(1), 291–304.
- Dale, J. E., Ercolano, B. & Bonnell, I. (2012), ‘Triggering, suppressing and redistributing star formation’, *arXiv e-prints* p. arXiv:1208.3364.

- Dale, J. E., Ngoumou, J., Ercolano, B. & Bonnell, I. A. (2013), ‘Massive stars in massive clusters - IV. Disruption of clouds by momentum-driven winds’, *Monthly Notices of the Royal Astronomical Society* **436**(4), 3430–3445.
- Dale, J. E., Ngoumou, J., Ercolano, B. & Bonnell, I. A. (2014), ‘Before the first supernova: combined effects of H II regions and winds on molecular clouds’, *Monthly Notices of the Royal Astronomical Society* **442**(1), 694–712.
- Dobbs, C. L. (2008), ‘GMC formation by agglomeration and self gravity’, *Monthly Notices of the Royal Astronomical Society* **391**(2), 844–858.
- Draine, B. T. (2011), *Physics of the Interstellar and Intergalactic Medium*.
- Ebert, R. (1955), ‘Über die Verdichtung von H I-Gebieten. Mit 5 Textabbildungen’, *Zeitschrift für Astrophysik* **37**, 217.
- Elmegreen, B. G. & Scalo, J. (2004), ‘Interstellar turbulence i: Observations and processes’, *Annual Review of Astronomy and Astrophysics* **42**(1), 211–273.
URL: <http://dx.doi.org/10.1146/annurev.astro.41.011802.094859>
- Ercolano, B., Barlow, M. J. & Storey, P. J. (2005), ‘The dusty MOCASSIN: fully self-consistent 3D photoionization and dust radiative transfer models’, *Monthly Notices of the Royal Astronomical Society* **362**(3), 1038–1046.
- Ercolano, B., Barlow, M. J., Storey, P. J. & Liu, X. W. (2003), ‘MOCASSIN: a fully three-dimensional Monte Carlo photoionization code’, *Monthly Notices of the Royal Astronomical Society* **340**(4), 1136–1152.
- Ercolano, B., Dale, J. E., Gritschneider, M. & Westmoquette, M. (2012), ‘Synthetic observations of simulated Pillars of Creation’, *Monthly Notices of the Royal Astronomical Society* **420**(1), 141–146.
- Falgarone, E. (1997), ‘Structure of molecular clouds and turbulence.’, *IAU Symposium* **170**, 119–127.
- Fukui, Y. & Kawamura, A. (2010), ‘Molecular clouds in nearby galaxies’, *Annual Review of Astronomy and Astrophysics* **48**(1), 547–580.
URL: <https://doi.org/10.1146/annurev-astro-081309-130854>
- Garay, G. & Lizano, S. (1999), ‘Massive Stars: Their Environment and Formation’, *Publications of the Astronomical Society of the Pacific* **111**(763), 1049–1087.
- Gingold, R. A. & Monaghan, J. J. (1977), ‘Smoothed particle hydrodynamics: theory and application to non-spherical stars’, *Monthly Notices of the Royal Astronomical Society* **181**(3), 375–389.
URL: <https://doi.org/10.1093/mnras/181.3.375>
- Goldsworthy, F. A. (1958), ‘On the Propagation and Structure of Ionization Fronts’, *Reviews of Modern Physics* **30**(3), 1062–1068.

- Gordon, K. D., Gies, D. R., Schaefer, G. H., Huber, D., Ireland, M. & Hillier, D. J. (2018), ‘Angular Sizes and Effective Temperatures of O-type Stars from Optical Interferometry with the CHARA Array’, *The Astrophysical Journal* **869**(1), 37.
- Greenberg, J. M. (1980), Interstellar dust - A sink and source of molecules, in ‘Les Spectres des Molécules Simples au Laboratoire et en Astrophysique’, pp. 555–560.
- Gritschneider, M., Naab, T., Walch, S., Burkert, A. & Heitsch, F. (2009), ‘Driving Turbulence and Triggering Star Formation by Ionizing Radiation’, *The Astrophysical Journal Letters* **694**(1), L26–L30.
- Heap, S. R., Lanz, T. & Hubeny, I. (2006), ‘Fundamental Properties of O-Type Stars’, *The Astrophysical Journal* **638**(1), 409–432.
- Hennebelle, P. & Falgarone, E. (2012), ‘Turbulent molecular clouds’, *The Astronomy and Astrophysics Review* **20**(1).
URL: <http://dx.doi.org/10.1007/s00159-012-0055-y>
- Hester, J. J. & Desch, S. J. (2005), *Understanding Our Origins: Star Formation in HII Region Environments*, Vol. 341 of *Astronomical Society of the Pacific Conference Series*, p. 107.
- Hubber, D. A., Ercolano, B. & Dale, J. (2016), ‘Observing gas and dust in simulations of star formation with Monte Carlo radiation transport on Voronoi meshes’, *Monthly Notices of the Royal Astronomical Society* **456**(1), 756–766.
- Jeans, J. H. (1928), *Astronomy and cosmogony*.
- Jones, K., Jones, K. & Messier, C. (1991), *Messier’s Nebulae and Star Clusters*, Practical Astronomy Handbooks, Cambridge University Press.
URL: <https://books.google.co.uk/books?id=SL EzPBn1i2gC>
- Kauffmann, G., Heckman, T. M., Tremonti, C., Brinchmann, J., Charlot, S., White, S. D. M., Ridgway, S. E., Brinkmann, J., Fukugita, M., Hall, P. B., Ivezić, Ž., Richards, G. T. & Schneider, D. P. (2003), ‘The host galaxies of active galactic nuclei’, *Monthly Notices of the Royal Astronomical Society* **346**(4), 1055–1077.
- Kessel-Deynet, O. (1999), Treatment of Ionizing Radiation in Smoothed Particle Hydrodynamics Calculations and Application to the Dynamics of Cloud Cores in the Radiation Field of Massive Stars, PhD thesis, Max-Planck-Institut für Astronomie, Königstuhl 17, D-69117 Heidelberg, Germany.
- Kewley, L. J., Dopita, M. A., Sutherland, R. S., Heisler, C. A. & Trevena, J. (2001), ‘Theoretical Modeling of Starburst Galaxies’, *The Astrophysical Journal* **556**(1), 121–140.
- Kewley, L. J., Groves, B., Kauffmann, G. & Heckman, T. (2006), ‘The host galaxies and classification of active galactic nuclei’, *Monthly Notices of the Royal Astronomical Society* **372**(3), 961–976.

- Kharchenko, N. V., Piskunov, A. E., Röser, S., Schilbach, E. & Scholz, R. D. (2005), ‘Astrophysical parameters of Galactic open clusters’, *Astronomy and Astrophysics* **438**(3), 1163–1173.
- Krumholz, M. R., Bate, M. R., Arce, H. G., Dale, J. E., Gutermuth, R., Klein, R. I., Li, Z. Y., Nakamura, F. & Zhang, Q. (2014), Star Cluster Formation and Feedback, *in* H. Beuther, R. S. Klessen, C. P. Dullemond & T. Henning, eds, ‘Protostars and Planets VI’, p. 243.
- Laor, A. & Draine, B. T. (1993), ‘Spectroscopic Constraints on the Properties of Dust in Active Galactic Nuclei’, *The Astrophysical Journal* **402**, 441.
- Larson, R. B. (1979), ‘Stellar kinematics and interstellar turbulence.’, *Monthly Notices of the Royal Astronomical Society* **186**, 479–490.
- Larson, R. B. (1981), ‘Turbulence and star formation in molecular clouds.’, *Monthly Notices of the Royal Astronomical Society* **194**, 809–826.
- Lefèvre, C., Pagani, L., Juvela, M., Paladini, R., Lallement, R., Marshall, D. J., Andersen, M., Bacmann, A., McGehee, P. M., Montier, L., Noriega-Crespo, A., Pelkonen, V. M., Ristorcelli, I. & Steinacker, J. (2014), ‘Dust properties inside molecular clouds from coreshine modeling and observations’, *Astronomy and Astrophysics* **572**, A20.
- Leto, P., Umana, G., Trigilio, C., Buemi, C. S., Dolei, S., Manzitto, P., Cerrigone, L. & Siringo, C. (2009), ‘7 mm continuum observations of ultra compact HII regions’, *Astronomy and Astrophysics* **507**(3), 1467–1473.
- Mac Low, M.-M., Klessen, R. S., Burkert, A. & Smith, M. D. (1998), ‘Kinetic Energy Decay Rates of Supersonic and Super-Alfvénic Turbulence in Star-Forming Clouds’, *Physical Review Letters* **80**(13), 2754–2757.
- McLeod, A. F., Dale, J. E., Evans, C. J., Ginsburg, A., Kruijssen, J. M. D., Pellegrini, E. W., Ramsay, S. K. & Testi, L. (2019), ‘Feedback from massive stars at low metallicities: MUSE observations of N44 and N180 in the Large Magellanic Cloud’, *Monthly Notices of the Royal Astronomical Society* **486**(4), 5263–5288.
- McLeod, A. F., Dale, J. E., Ginsburg, A., Ercolano, B., Gritschneider, M., Ramsay, S. & Testi, L. (2015), ‘The Pillars of Creation revisited with MUSE: gas kinematics and high-mass stellar feedback traced by optical spectroscopy’, *Monthly Notices of the Royal Astronomical Society* **450**(1), 1057–1076.
- McLeod, A. F., Weilbacher, P. M., Ginsburg, A., Dale, J. E., Ramsay, S. & Testi, L. (2016), ‘A nebular analysis of the central Orion nebula with MUSE’, *Monthly Notices of the Royal Astronomical Society* **455**(4), 4057–4086.
- Medina, S. N. X., Arthur, S. J., Henney, W. J., Mellema, G. & Gazol, A. (2014), ‘Turbulence in simulated H II regions’, *Monthly Notices of the Royal Astronomical Society* **445**(2), 1797–1819.

- Morales, E. F. E., Wyrowski, F., Schuller, F. & Menten, K. M. (2013), ‘Stellar clusters in the inner Galaxy and their correlation with cold dust emission’, *Astronomy and Astrophysics* **560**, A76.
- Murray, N. (2011), ‘Star Formation Efficiencies and Lifetimes of Giant Molecular Clouds in the Milky Way’, *The Astrophysical Journal* **729**(2), 133.
URL: <https://doi.org/10.1088/0004-637x/729/2/133>
- Noriega-Crespo, A. (1986), The Effects of Hydrogen II Regions and Supernovae in Proto-Dwarf Galaxies., PhD thesis, California Univ., Santa Cruz.
- O’dell, C. R. (2001), ‘The Orion Nebula and its Associated Population’, *Annual Review of Astronomy and Astrophysics* **39**, 99–136.
- Offner, S. S. R. & McKee, C. F. (2011), ‘The Protostellar Luminosity Function’, *The Astrophysical Journal* **736**(1), 53.
- Oishi, J. S. & Low, M.-M. M. (2006), ‘The inability of ambipolar diffusion to set a characteristic mass scale in molecular clouds’, *The Astrophysical Journal* **638**(1), 281–285.
URL: <https://doi.org/10.1086>
- Oort, J. H. (1954), ‘Outline of a theory on the origin and acceleration of interstellar clouds and O associations’, *Bulletin of the Astronomical Institutes of the Netherlands* **12**, 177.
- Paradis, D., Mény, C., Juvela, M., Noriega-Crespo, A. & Ristorcelli, I. (2019), ‘Revisiting the dust properties in the molecular clouds of the Large Magellanic Cloud’, *Astronomy and Astrophysics* **627**, A15.
- Peters, T., Klessen, R. S., Mac Low, M.-M. & Banerjee, R. (2010), ‘Limiting Accretion onto Massive Stars by Fragmentation-induced Starvation’, *The Astrophysical Journal* **725**(1), 134–145.
- Relaño, M., Verley, S., Pérez, I., Kramer, C., Calzetti, D., Xilouris, E. M., Boquien, M., Abreu-Vicente, J., Combes, F., Israel, F. & et al. (2013), ‘Spectral energy distributions of hii regions in m33 (herm33es)’, *Astronomy Astrophysics* **552**, A140.
URL: <http://dx.doi.org/10.1051/0004-6361/201220073>
- Siess, L., Dufour, E. & Forestini, M. (2000), ‘An internet server for pre-main sequence tracks of low- and intermediate-mass stars’, *Astronomy and Astrophysics* **358**, 593–599.
- Speck, A. K., Corman, A. B., Wakeman, K., Wheeler, C. H. & Thompson, G. (2009), ‘Silicon Carbide Absorption Features: Dust Formation in the Outflows of Extreme Carbon Stars’, *The Astrophysical Journal* **691**(2), 1202–1221.
- Spitzer, L. & Army, T. T. (1978), ‘Physical Processes in the Interstellar Medium’, *American Journal of Physics* **46**(11), 1201–1201.
- Stevance, H. F., Eldridge, J. J., McLeod, A., Stanway, E. R. & Chrimes, A. A. (2020), ‘A systematic aging method I: HII regions D118 and D119 in NGC 300’, *Monthly Notices of the Royal Astronomical Society* p. arXiv:2004.02883.

- Strömberg, B. (1939), ‘The Physical State of Interstellar Hydrogen.’, *The Astrophysical Journal* **89**, 526.
- Tan, J. C., Beltrán, M. T., Caselli, P., Fontani, F., Fuente, A., Krumholz, M. R., McKee, C. F. & Stolte, A. (2014), Massive Star Formation, *in* H. Beuther, R. S. Klessen, C. P. Dullemond & T. Henning, eds, ‘Protostars and Planets VI’, p. 149.
- Vandervoort, P. O. (1963), ‘The Formation of H II Regions.’, *The Astrophysical Journal* **137**, 381.
- Vázquez-Semadeni, E., Cantó, J. & Lizano, S. (1998), ‘Does Turbulent Pressure Behave as a Logatropé?’, *The Astrophysical Journal* **492**(2), 596–602.
- Wang, J., Feigelson, E. D., Townsley, L. K., Broos, P. S., Román-Zúñiga, C. G., Lada, E. & Garmire, G. (2010), ‘A Chandra Study of the Rosette Star-forming Complex. III. The NGC 2237 Cluster and the Region’s Star Formation History’, *The Astrophysical Journal* **716**(1), 474–489.
- Ye, T. (1992), ‘Diameter distribution of HII regions in galaxies.’, *Monthly Notices of the Royal Astronomical Society* **255**, 32–40.
- Zhou, Z.-M., Wu, H., Huang, L., Li, H.-B., Zhou, Z.-Z., Jia, J.-J., Lam, M. I. & Zhu, Y.-N. (2014), ‘Metallicity and star formation activities of the interacting system arp 86 from observation with mos on xinglong 2.16m telescope’, *Research in Astronomy and Astrophysics* **14**.
- Zhuravlev, V. V. (2020), ‘Dynamic role of dust in formation of molecular clouds’, *Monthly Notices of the Royal Astronomical Society* **500**(2), 2209–2226.
URL: <http://dx.doi.org/10.1093/mnras/staa3424>

9 Appendices

9.1 Appendix A

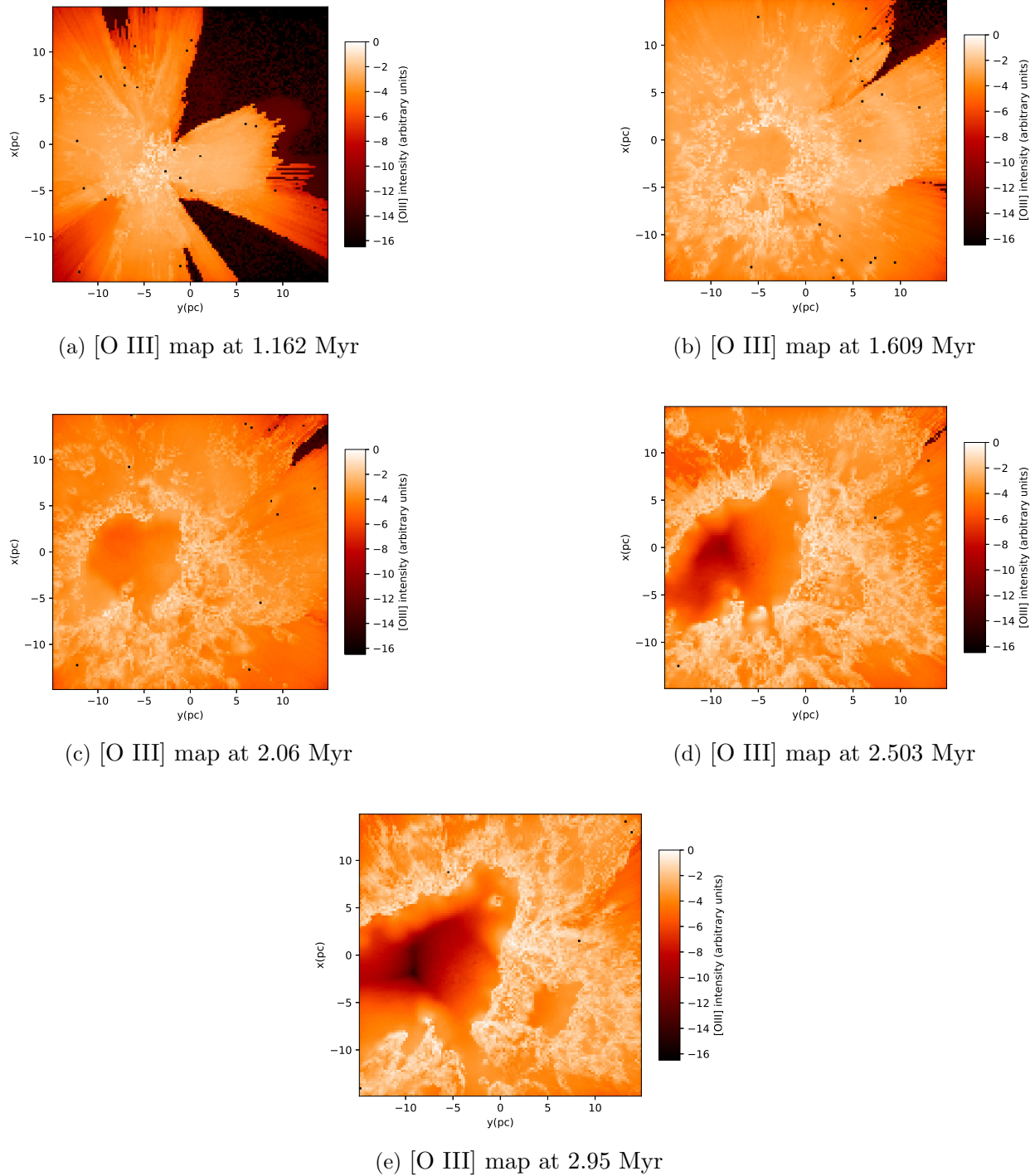
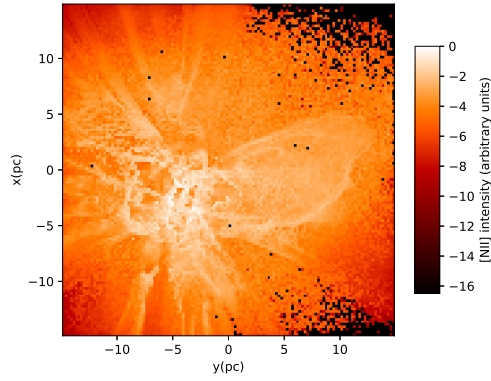
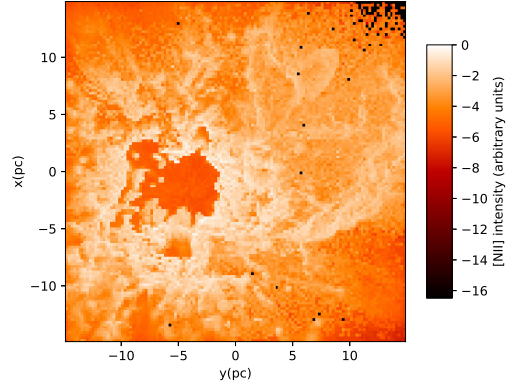


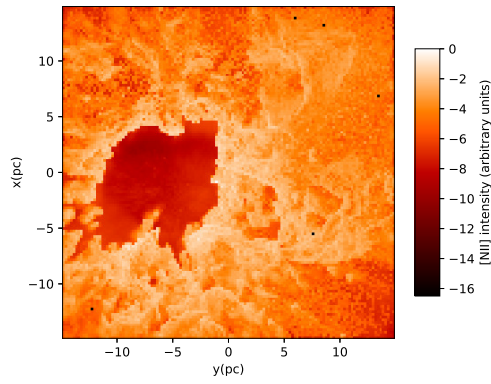
Figure 32: Evolution of [O III] within the GMC of Run I with time. Clear bubble-like regions are observed as a result of the photoionization of hydrogen and stellar-driven winds.



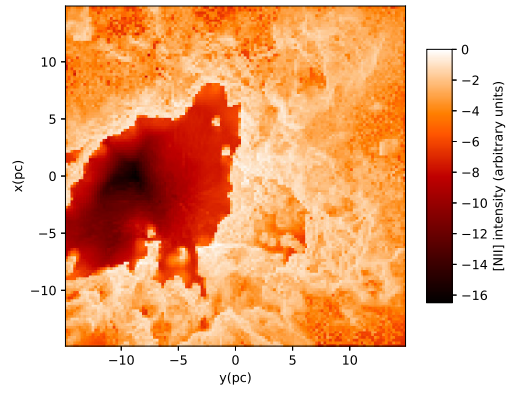
(a) [N II] map at 1.162 Myr



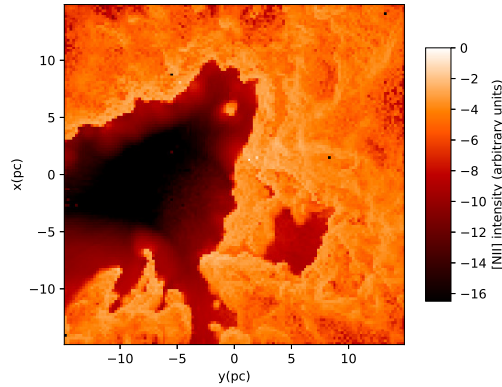
(b) [N II] map at 1.609 Myr



(c) [N II] map at 2.06 Myr

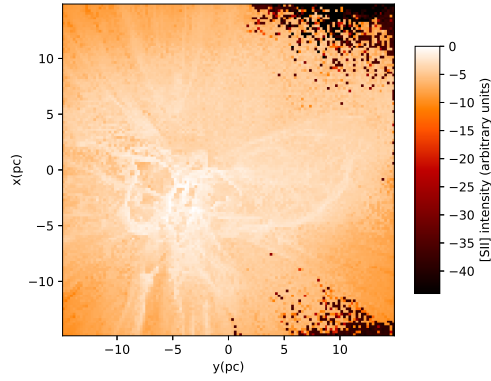


(d) [N II] map at 2.503 Myr

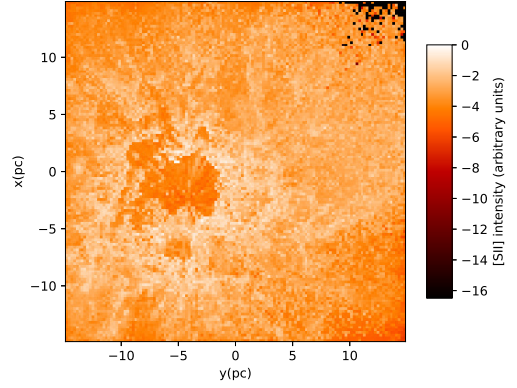


(e) [N II] map at 2.95 Myr

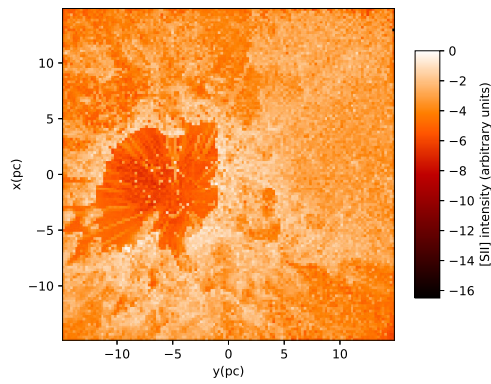
Figure 33: Evolution of $[NII]$ within the GMC of Run I with time. Clear bubble-like regions are observed as a result of the photoionization of hydrogen and stellar-driven winds.



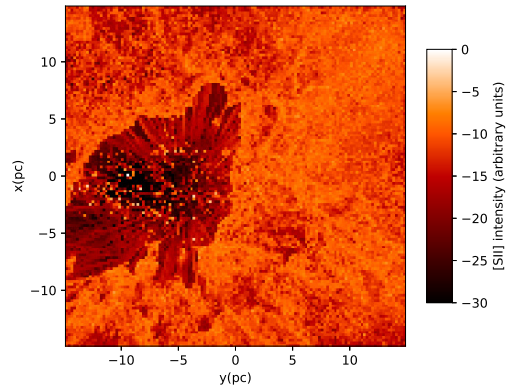
(a) [S II] map at 1.162 Myr



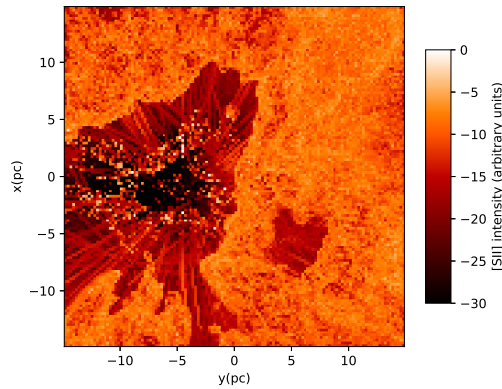
(b) [S II] map at 1.609 Myr



(c) [S II] map at 2.06 Myr



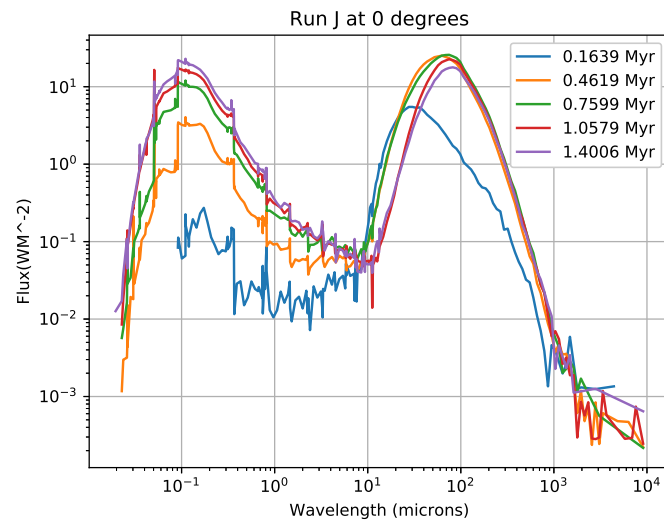
(d) [S II] map at 2.503 Myr



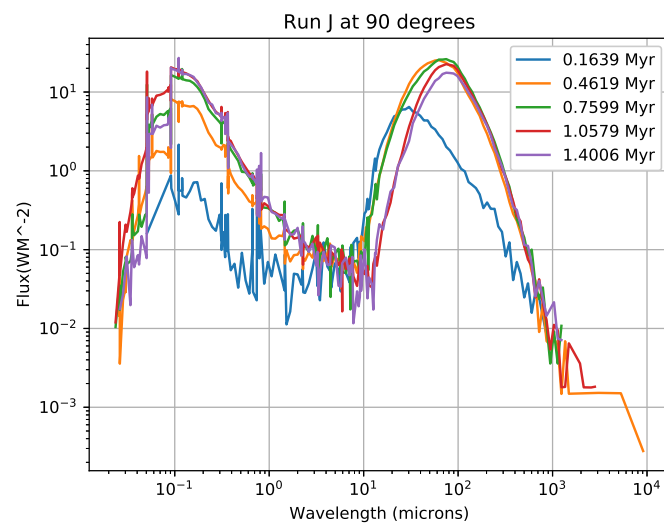
(e) [S II] map at 2.95 Myr

Figure 34: Evolution of $[SII]$ within the GMC of Run I with time. Clear bubble-like regions are observed as a result of the photoionization of hydrogen and stellar-driven winds. This is also an example of when MOCASSIN failed to be able to fully converged the temperature in all of the cells in the grid, and as such has left this unconverged result.

9.2 Appendix B

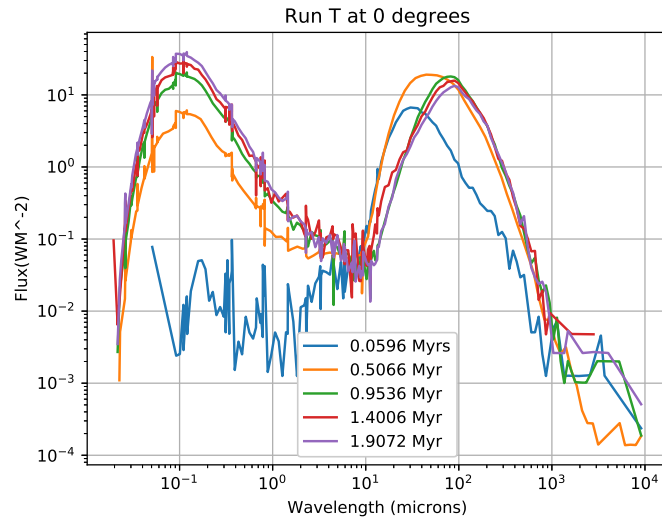


(a) SED over time along the z-axis

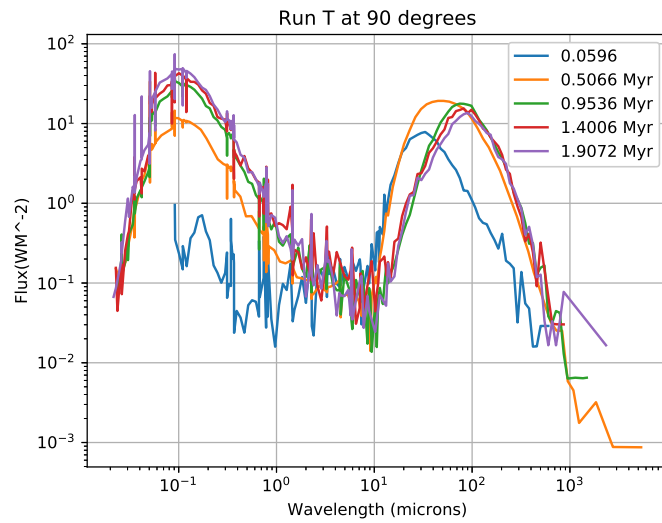


(b) SED over time at 90 to z axis

Figure 35: SED comparison from two different observation angles for Run J to illustrate the similarity found in features such as the IR and UV peaks with two separate viewing axes.

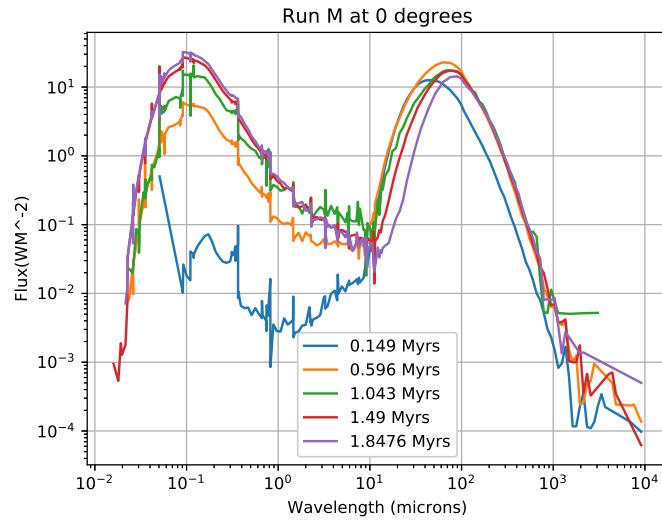


(a) SED over time along the z-axis

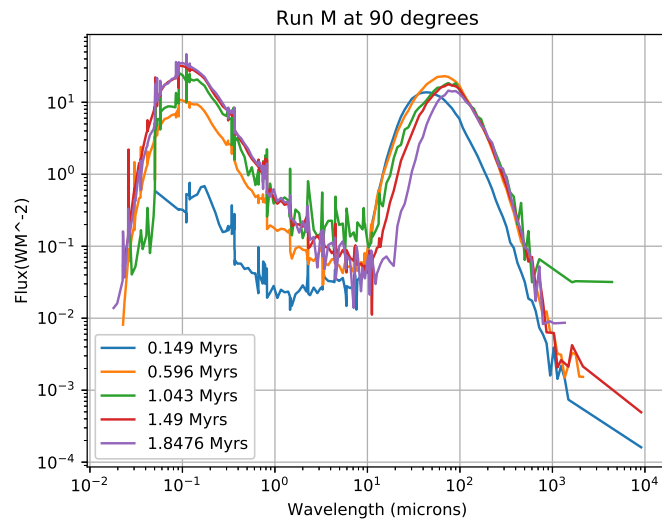


(b) SED over time at 90 to z axis

Figure 36: SED comparison from two different observation angles for Run T to illustrate the similarity found in features such as the IR and UV peaks with two separate viewing axes.

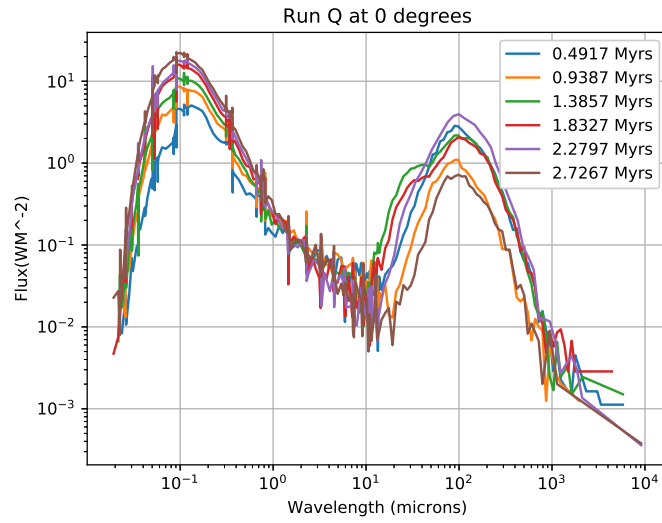


(a) SED over time along the z-axis

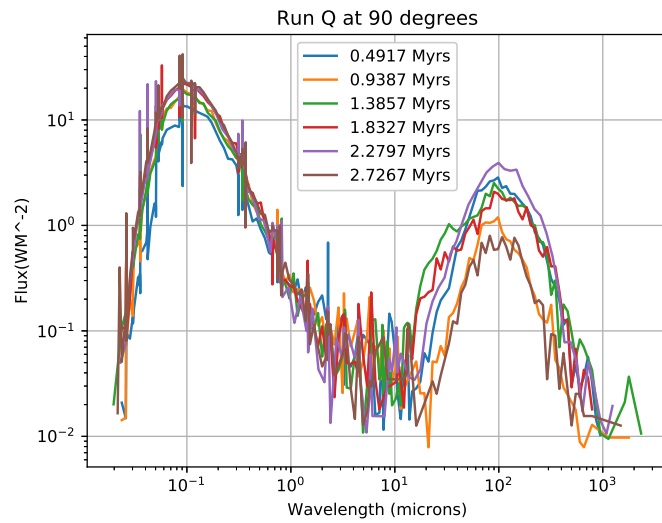


(b) SED over time at 90 to z axis

Figure 37: SED comparison from two different observation angles for Run M to illustrate the similarity found in features such as the IR and UV peaks with two separate viewing axes.



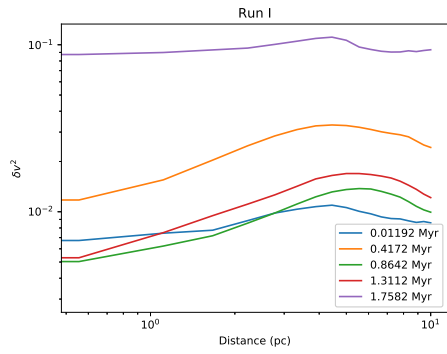
(a) SED over time along the z-axis



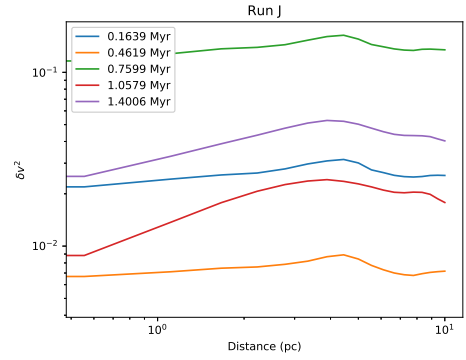
(b) SED over time at 90 to z axis

Figure 38: SED comparison from two different observation angles for Run Q to illustrate the similarity found in features such as the IR and UV peaks with two separate viewing axes.

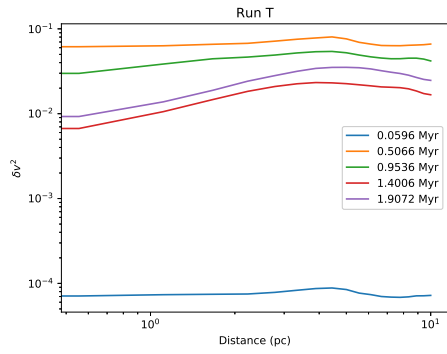
9.3 Appendix C



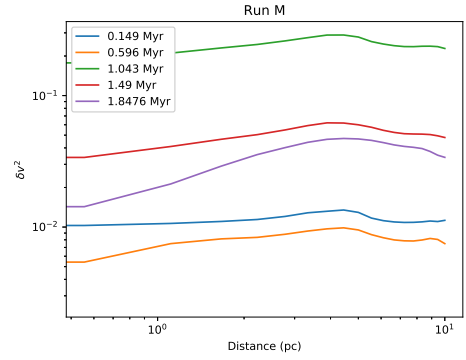
(a) Run I



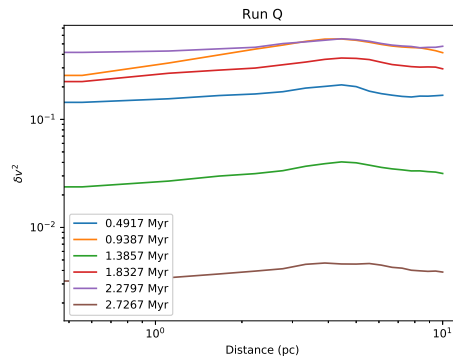
(b) Run J



(c) Run T

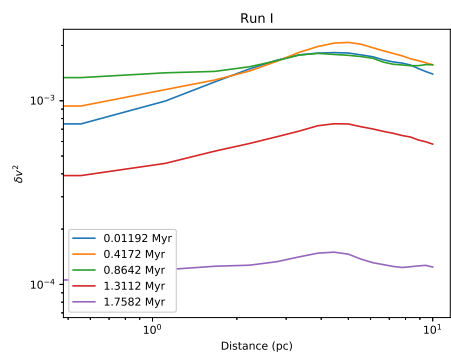


(d) Run M

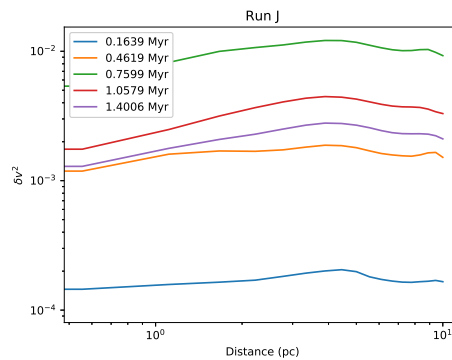


(e) Run Q

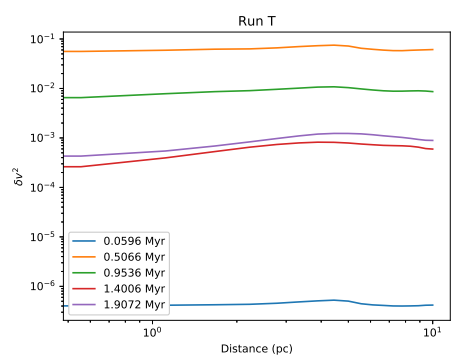
Figure 39: Structure functions with $[\text{N II}]$ emission included. Any power-law patterns within the results are very weak and likely not the definitive result of energetic differences in the turbulent nature of the cloud with distance.



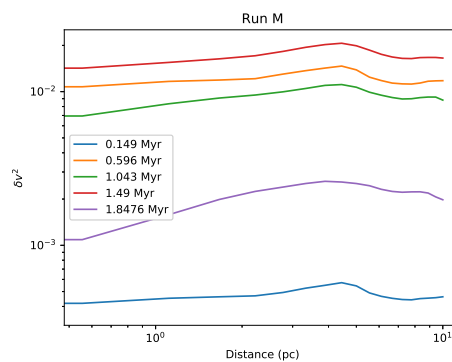
(a) Run I



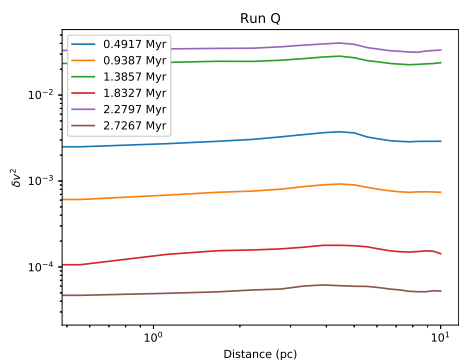
(b) Run J



(c) Run T



(d) Run M



(e) Run Q

Figure 40: Structure functions in $[\text{O III}]$ emission. Any power-law patterns within the results are very weak and likely not the definitive result of energetic differences in the turbulent nature of the cloud with distance.

9.4 Appendix D

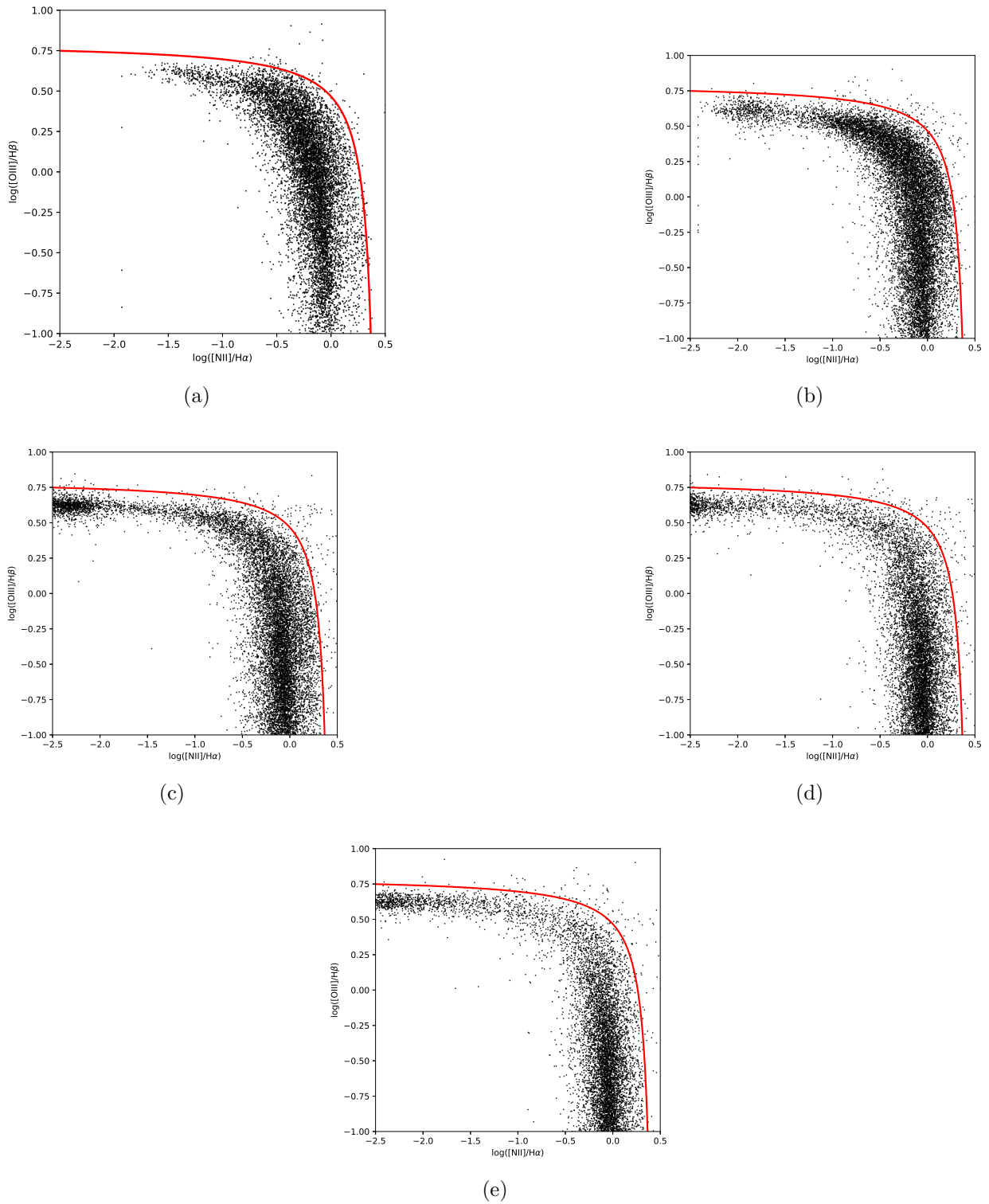
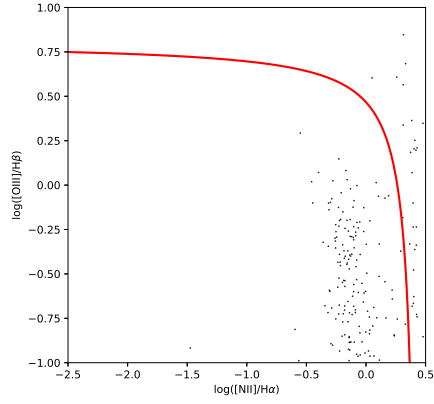
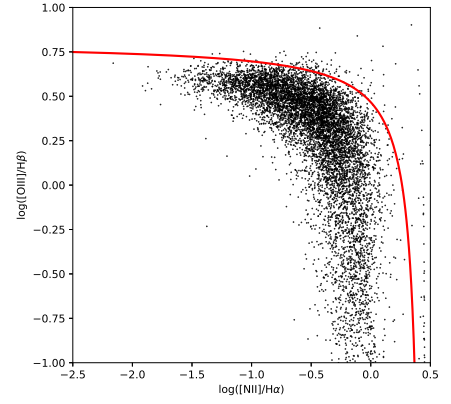


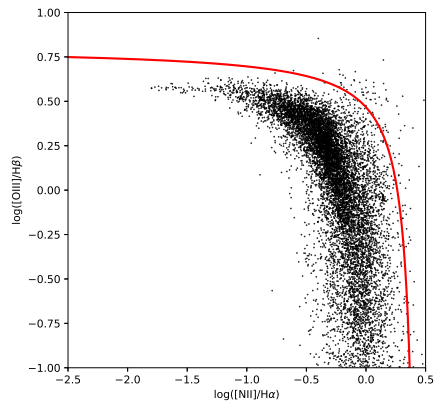
Figure 41: BPT maps of $[OIII]/H\beta - [NII]/H\alpha$ for Run I. The red contour is the new fit I have made to better describe the data within the BPT map for these ratios.



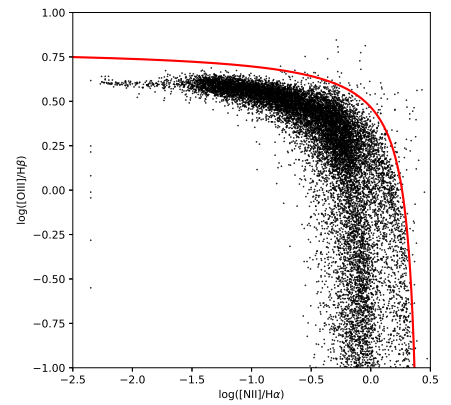
(a)



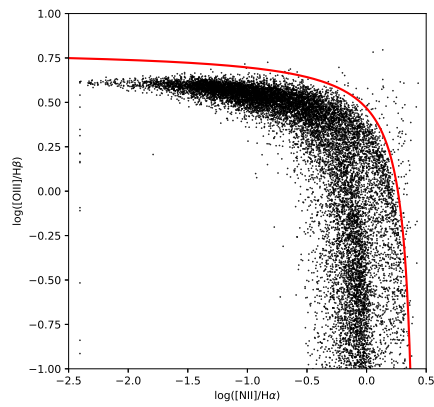
(b)



(c)

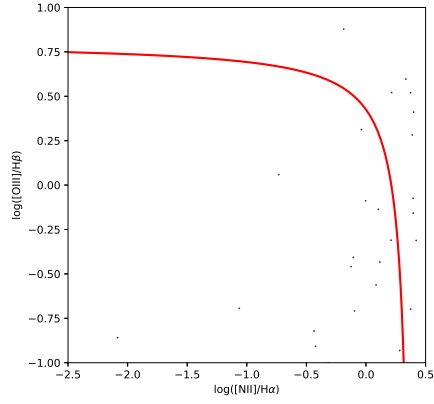


(d)

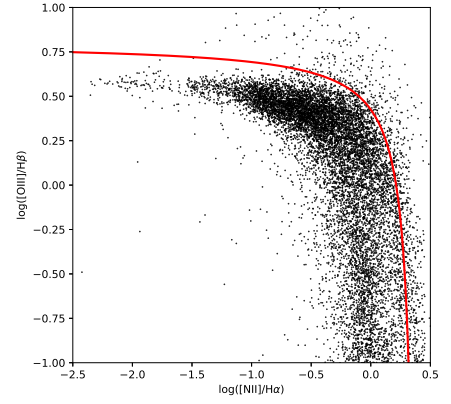


(e)

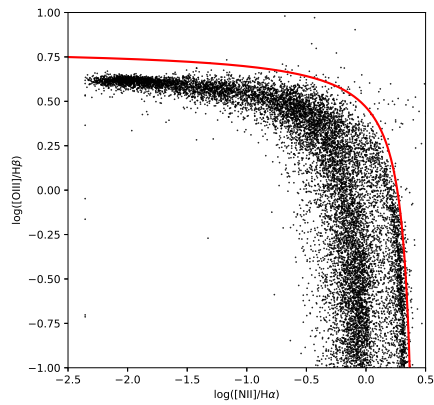
Figure 42: BPT maps of $[OIII]/H\beta - [NII]/H\alpha$ for Run J. The red contour is the new fit I have made to better describe the data within the BPT map for these ratios.



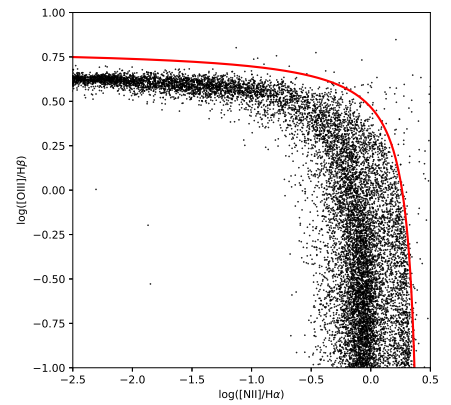
(a)



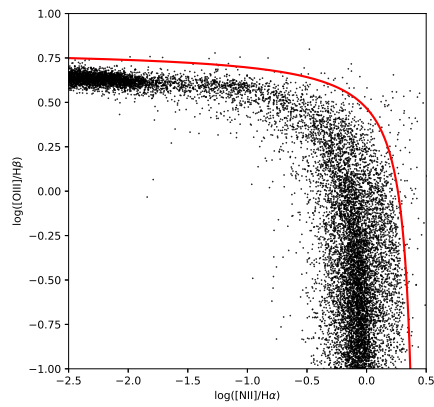
(b)



(c)

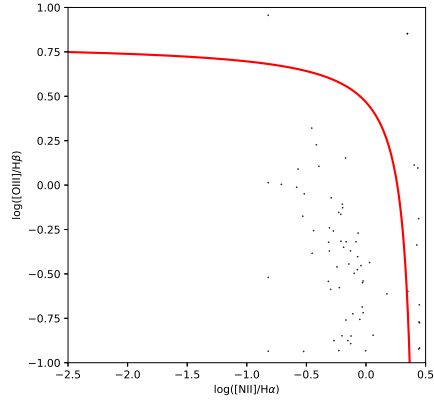


(d)

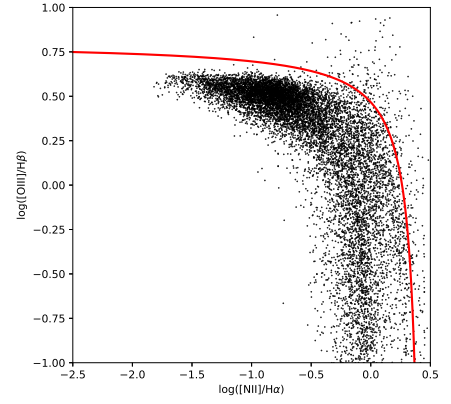


(e)

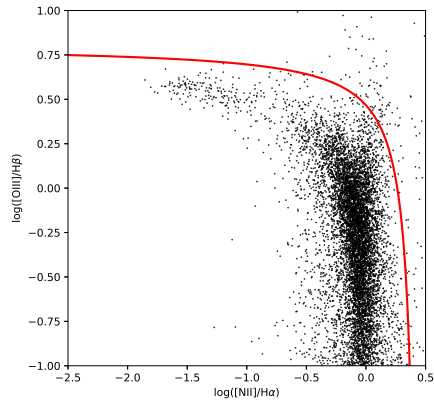
Figure 43: BPT maps of $[\text{OIII}]/\text{H}\beta - [\text{NII}]/\text{H}\alpha$ for Run T. The red contour is the new fit I have made to better describe the data within the BPT map for these ratios.



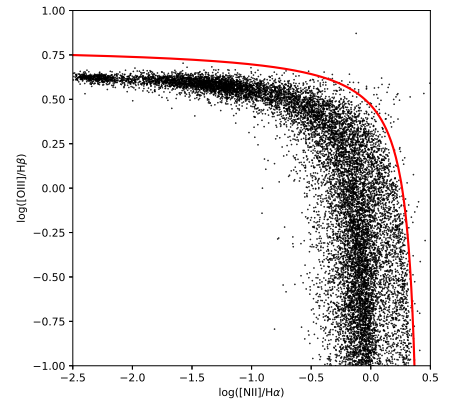
(a)



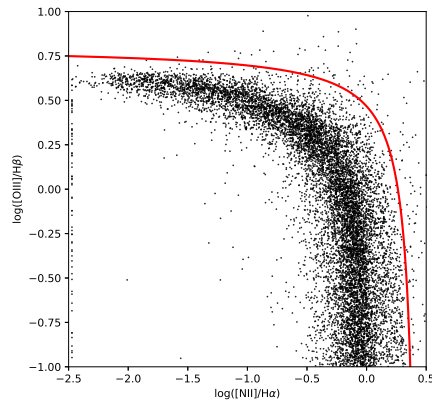
(b)



(c)

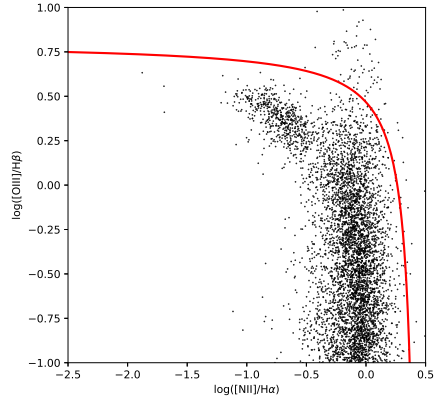


(d)

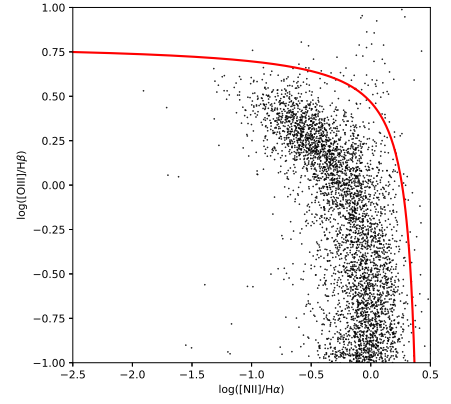


(e)

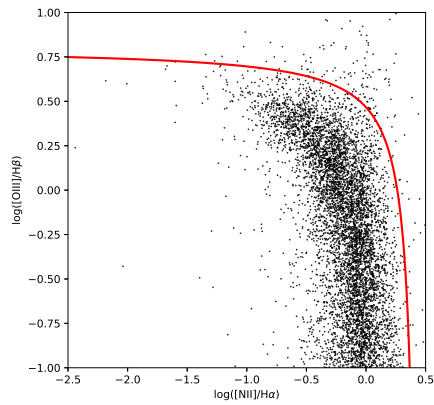
Figure 44: BPT maps of $[OIII]/H\beta - [NII]/H\alpha$ for Run M. The red contour is the new fit I have made to better describe the data within the BPT map for these ratios.



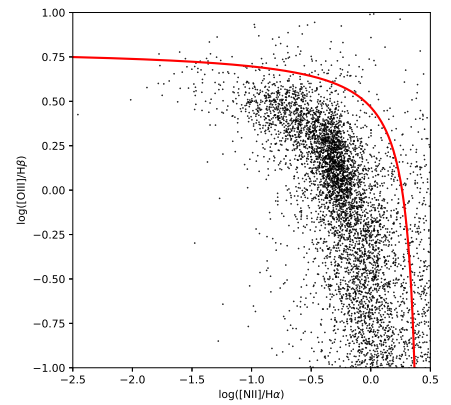
(a)



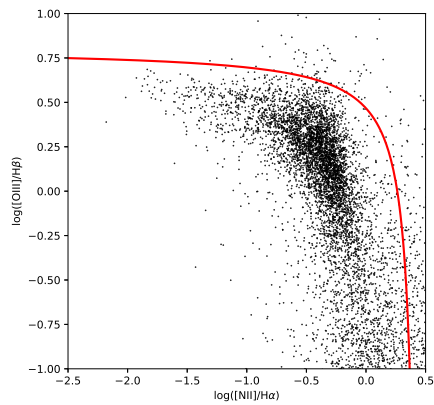
(b)



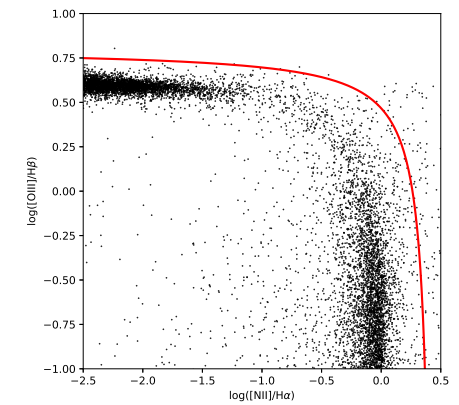
(c)



(d)



(e)



(f)

Figure 45: BPT maps of $[\text{OIII}]/\text{H}\beta - [\text{NII}]/\text{H}\alpha$ for Run Q. The red contour is the new fit I have made to better describe the data within the BPT map for these ratios.